

STRAIN AGING IN NICKEL 200

By

WALTER RAYMOND CRIBB

A DISSERTATION PRESENTED TO THE GRADUATE COUNCIL OF
THE UNIVERSITY OF FLORIDA IN PARTIAL FULFILLMENT OF THE
REQUIREMENTS FOR THE DEGREE OF DOCTOR OF PHILOSOPHY

UNIVERSITY OF FLORIDA

1975



UNIVERSITY OF FLORIDA



3 1262 08552 4618

To Mom and Dad

ACKNOWLEDGMENTS

Sincere appreciation is due many people in this department for their help during my entire stay at the University of Florida. Most sincere thanks are due Professor Robert E. Reed-Hill whose continued guidance and encouragement made this dissertation possible.

Many thanks to Professor F.N. Rhines who first encouraged me and gave me confidence to strive for a higher degree in metallurgy and whose continued interest in my program is appreciated.

I would also like to thank the members of my committee, Drs. Martin A. Eisenberg, Craig S. Hartley and John J. Hren for fruitful discussions of my work.

Many thanks to my colleagues Messrs. Juan R. Donoso, R.M. Chhatre, Francisco Boratto and to the laboratory assistants C. Barnes and M. Brimanson who spent many hours of discussion and who cooperated in the collection and interpretation of experimental data. The preparation of the final manuscript by Elizabeth Beville is also greatly appreciated.

The financial support of the Army Research Office (Durham), the International Nickel Company, and the Energy Research and Development Administration is greatly appreciated.

Finally, I thank my wife, Kathie, whose patience, encouragement and understanding during my course of study helped make it all possible.

TABLE OF CONTENTS

	<u>PAGE</u>
ACKNOWLEDGMENTS	iii
LIST OF TABLES	vii
LIST OF FIGURES	viii
ABSTRACT	xi
INTRODUCTION	1
CHAPTER	
I PREVIOUS INVESTIGATIONS	4
1.1 Static Strain Aging	4
1.1.1 Historical Aspects	4
1.1.2 Mechanisms of Static Strain Aging in Metals Alloys	5
1.1.3 Summary of Important Mechanisms of Dislocation Locking During Aging	10
1.1.4 Aspects of the Static Strain Aging Experiment..	11
1.1.5 Static Strain Aging Stages in BCC Metals	13
1.1.6 Static Strain Aging in Nickel and FCC Alloys...	17
1.2 Dynamic Strain Aging	19
1.3 Work Hardening in Metals and Alloys	23
1.4 Anelastic Phenomena in Nickel and FCC Ferrous Alloys..	27
II EXPERIMENTAL PROCEDURES	35
2.1 Materials	35
2.2 Experimental Techniques	37

	<u>PAGE</u>
2.2.1	Swaging 37
2.2.2	Annealing 37
2.2.3	Specimen Profile Measurements 37
2.2.4	Tensile Testing 38
2.2.5	Static Aging Experiments 38
III	EXPERIMENTAL RESULTS 43
3.1	The Behavior of the Lower Yield Stress Increase, $\Delta\sigma$... 43
3.2	The Lüders Extension, ϵ_L 50
3.3	The Hardening Component, $\Delta\sigma_H$ 50
3.4	Activation Energies 50
3.5	The Dependence of $\Delta\sigma$ and ϵ_L on Prestrain 53
3.6	Comparison of Nickel 270 and Nickel 200 Static Strain Aging 55
3.7	The Stress-Strain Behaviors 57
3.8	The Work Hardening Behaviors of Nickel 270 and of Nickel 200 69
IV	DISCUSSION 80
4.1	Rationale for Static Strain Aging in Nickel 200 80
4.2	The Mechanism for Static Strain Aging Exhibited in Nickel 200 82
4.2.1	The Distribution of Vacancies, Carbon Atoms and Dislocations After Plastic Deformation 82
4.2.2	Vacancy Trapping by Carbon Atoms 82
4.2.3	The Concentration of Carbon-Vacancy Pairs 83
4.2.4	Theory of Initial Schoeck Locking by Carbon- Vacancy Pairs 85
4.2.5	The Mechanism Controlling the Increase in $\Delta\sigma$ with Time 96
4.2.6	Regarding the Behavior of Nickel 200 After the Peak in $\Delta\sigma$ 107

	<u>PAGE</u>
4.3 Summary	114
4.4 Comments on the Relationship Between Static Strain Aging and Dynamic Strain Aging in Nickel 200	115
CONCLUSIONS AND OBSERVATIONS	121
APPENDICES	
A COMPUTATION OF THE INTERACTION ENERGY BETWEEN A CARBON-VACANCY PAIR DEFECT AND SCREW DISLOCATIONS IN FCC METALS	125
B DETERMINATION OF $U(x)$, THE ENERGY OF A SCREW DISLOCATION DISPLACED A DISTANCE x FROM THE CENTER OF ITS SNOEK ATMOSPHERE	132
BIBLIOGRAPHY	135
BIOGRAPHICAL SKETCH	144

LIST OF TABLES

<u>Table</u>		<u>Page</u>
1	Recognized Aspects of Strain Aging	2
2	The Diffusivity of Carbon in Nickel	21
3	Estimates of the Rate of Vacancy Production During Plastic Deformation	32
4	Alloy Compositions	36
5	Least Squares Parameters for Static Strain Aging Data Assuming $\Delta\sigma$ Is a Function of $\ln t$	45
6	Least Squares Parameters for Static Strain Aging Data Assuming a Log $\Delta\sigma$ -Log t Linear Relationship	49
7	The Slopes and Intercepts (at $t = 1s$) of $\Delta\sigma$ Versus $\ln t$ Curves Calculated from Eq. 56	108
8	Interaction Energies for Tetragonal Defects in the FCC Structure	128

LIST OF FIGURES

<u>Figure</u>		<u>Page</u>
1	General aspects of the classical static strain aging test	12
2	An example of the stages of the yield return in Nb-0 alloys [8]; (a) the increase in $\Delta\sigma$ with time; (b) the components of $\Delta\sigma$ and their dependence on aging time.....	16
3	Schematic example of stage behavior in polycrystalline fcc metals	25
4	Schematic description of the work hardening behavior in a metal using a log Θ -log σ plot	25
5	Illustrating the method used to determine the aging parameters ϵ_L , $\Delta\sigma = \sigma_{LY} - \sigma_0$ and $\Delta\sigma_H = \sigma_{Ext} - \sigma_0$. Dashed loading line indicates the approximate loading line which would have been observed in the absence of misalignment of the test specimen	41
6	Selected load-time curves obtained after prestraining a series of specimens 5% at 273°K, aging at 408°K for the times indicated, and restraining at 273°K	42
7	The time and temperature dependence of the return of the lower yield stress in Nickel 200. Specimens were prestrained to a stress level of 265 MPa. The dashed curves are approximate corrected curves which account for specimen heat-up in the aging baths	44
8	Normalized aging curves for Nickel 200. The 373°K curve was normalized to an assumed maximum of 28.5 MPa. The dashed curves reflect approximate corrections for the heat-up time of the specimens	47
9	Illustrating the approximate $t^{1/7}$ power law relation governing the aging of Nickel 200 at temperatures below 448°K. Data for the 448°K (shown) and 473°K cases do not fit this relation well	48
10	The dependence of the Lüders strain on time and temperature in Nickel 200	51

11	The approximate behavior of the secondary hardening component of the lower yield stress increase ($\Delta\sigma_H = \sigma_{Ext} - \sigma_0$)	52
12	The dependence of $\Delta\sigma$ and ϵ_L on prestrain. Nickel 200 specimens were prestrained at 273°K, aged for 6000 seconds at 448°K, and restrained at 273°K	54
13	(a) The yield return of a Nickel 270 specimen aged for a time to achieve a maximum in $\Delta\sigma$ for Nickel 200. (b) Yield return for a Nickel 200 specimen aged only one-half as long	56
14	True stress-true plastic strain curves for Nickel 270 ($\dot{\epsilon} = 4.2 \times 10^{-4} \text{ s}^{-1}$)	58
15	Variation of the 0.2% yield stress and the ultimate tensile strength with temperature of Nickel 270 ($\dot{\epsilon} = 4.2 \times 10^{-4} \text{ s}^{-1}$)	59
16	Variation of the uniform and total elongation with temperature in Nickel 270 ($\dot{\epsilon} = 4.2 \times 10^{-4} \text{ s}^{-1}$)	60
17	True stress-true plastic strain curves for Nickel 200 ($\dot{\epsilon} = 4.2 \times 10^{-4} \text{ s}^{-1}$)	62
18	The temperature dependence of the 0.2% yield stress and ultimate tensile strength of Nickel 200	63
19	The temperature and strain rate dependence of the 0.2% yield stress in Nickel 200 on an expanded stress axis	64
20	Variation of the stresses at 5, 11, 19 and 30% plastic strain with temperature in Nickel 200	66
21	Variation of the uniform and total elongations with temperature in Nickel 200. Also shown are the approximate temperature ranges over which serrations were observed at the respective strain rates.....	67
22	Variation of reduction in area with temperature for Nickel 200 and Nickel 270	68
23	The log Θ -log σ curves of Nickel 270 ($\dot{\epsilon} = 4.2 \times 10^{-4} \text{ s}^{-1}$) .	70
24	The log Θ -log σ curves of Nickel 200 ($\dot{\epsilon} = 4.2 \times 10^{-4} \text{ s}^{-1}$) .	71
25	The variation of m_{II} and m_{III} with temperature in Nickel 270 ($\dot{\epsilon} = 4.2 \times 10^{-4} \text{ s}^{-1}$)	73

26	The variation of m_{II} and m_{III} with temperature in Nickel 200 ($\dot{\epsilon} = 4.2 \times 10^{-4} \text{ s}^{-1}$)	74
27	The variation of the work hardening parameter ($\sigma_{5\%} - \sigma_{0.5\%}$) with temperature ($\dot{\epsilon} = 4.2 \times 10^{-4} \text{ s}^{-1}$)	76
28	The variation of ϵ_2 and ϵ_3 (the approximate strains at which Stages II and III, respectively, begin) with temperature for Nickel 270 and Nickel 200 deformed at a strain rate of $4.2 \times 10^{-4} \text{ s}^{-1}$	78
29	The dependence of ϵ_3 on temperature and strain rate in Nickel 200	79
30	A schematic illustration of the assumed configuration of the carbon-vacancy pair and the three possible independent orientations that it may assume	87
31	The concentrations of dipoles in each of the three possible orientations ($B' = 0.3 \text{ eV}$ (6900 kcal/mole), $A = 0.2 \text{ eV}$ (4600 kcal/mole))	91
32	Schematic illustration of the growth of a saturated carbon-vacancy atmosphere. R_s is time dependent and the concentration within R_s is assumed to be a fraction, f , of the carbon concentration	99
33	The aging curves obtained from the model for strain aging in Nickel 200 (Eq. 56); the dashed lines are the experimental data (Figure 7)	109
34	This diagram illustrates the aging stages of Nickel 200. The solid line represents the experimental scope of the present investigation	116
35	The interaction potential u_i of a carbon-vacancy dipole with a screw dislocation for $r = b$ and $A/b = 0.2 \text{ eV}$	131

Abstract of Dissertation Presented to the
Graduate Council of the University of Florida in
Partial Fulfillment of the Requirements for
the Degree of Doctor of Philosophy

STRAIN AGING IN NICKEL 200

By

Walter Raymond Cribb

August, 1975

Chairman: Robert E. Reed-Hill
Major Department: Materials Science and Engineering

Dynamic and static strain aging were observed in commercially available Nickel 200 which contains principally 1000 ppm carbon as an alloying impurity. Static strain aging tests were conducted on annealed tensile specimens which were prestrained at 273°K to a stress level of 265 MPa (approximately 0.05 strain) at a nominal strain rate of $4.2 \times 10^{-3} \text{ s}^{-1}$. Under these conditions, homogeneous plastic flow was guaranteed to occur. Specimens were aged immediately after prestraining for different times at 373, 408, 428, 448 or 473°K and the time dependence of the return of the lower yield stress was observed. The return of the yield experiments indicated that $\Delta\sigma$ increased as $\ln t$ or approximately as $t^{1/7}$ kinetically and behaved in accordance with an activation energy of 25 kcal/mole before the observed peak in $\Delta\sigma$. It is demonstrated that the defect responsible for this anomalous increase in $\Delta\sigma$ may be the rotation of carbon-vacancy pairs in the strain fields of dislocations. A quantitative model is derived for the increase in $\Delta\sigma$ before the aging peak and it is concluded that several important stages in the aging of Nickel 200 may occur: (a) the formation of

carbon-vacancy pairs and their initial ordering, (b) the migration of vacancies in the strain energy gradients of dislocations and the consequent formation of more carbon-vacancy pairs near dislocations, (c) the growth of an ordered carbon-vacancy dipole atmosphere, (d) depletion of free vacancies in the remainder of the lattice which decreases the flux to the ordered atmosphere and results in a $\Delta\sigma$ maximum, (e) the migration of bound vacancies to dislocation sinks and the resulting decrease in $\Delta\sigma$, (f) the migration of carbon atoms in the strain fields of dislocations and the growth of a Cottrell atmosphere, and (g) precipitation of graphite during overaging. Items (f) and (g) are only speculated to occur. This model is different from the Cottrell-Bilby model and can account for the kinetics and activation energy for strain aging observed in Nickel 200.

Tensile tests were conducted between 77 and 800°K at nominal strain rates of 4.2×10^{-5} , 10^{-4} , 10^{-3} , and 10^{-2} s^{-1} . The results of these experiments confirm that dynamic strain aging (DSA) in Nickel 200 is exhibited over a temperature interval between 273 and 575°K at $4.2 \times 10^{-4} \text{ s}^{-1}$. Over the DSA interval, the following phenomena were exhibited and depended upon the strain rate: the Portevin-Le Chatelier Effect, yield stress plateaus, ultimate stress peaks, reduction in area minima and mild ductility minima. An analysis of work hardening indicates that anomalous work hardening over the DSA interval is very weakly exhibited. The mechanism for discontinuous yielding is rationalized to be dynamic Snoek ordering of carbon-vacancy pairs during plastic deformation and can account for the anomalously low temperature interval (with respect to the expected mobility of carbon) over which DSA is observed to occur.

INTRODUCTION

Currently, eight aspects of strain aging are recognized [1] as playing a major role in the deformation of polycrystalline metals (Table 1). The first two are static strain aging phenomena which are obtained by restraining a set of prestrained specimens that have been aged at an elevated temperature. The last six aspects listed in Table 1 are characteristic of dynamic strain aging, i.e., aging which occurs during plastic deformation. Dynamic strain aging can occur in both substitutional and interstitial alloys. The most interesting cases of dynamic strain aging have normally involved interstitial solutes in transition metals.

Most research on the role of interstitial impurities in the mechanical behavior of transition metals has been conducted using the body-centered cubic class of metals such as Fe, Nb, Mo, Ta, W and V [2]. The principal interstitial impurities in these metals which are responsible for strain aging are N, O, C and H.

Nickel is the only metal of the commercially important Period IV transition series of the Periodic Table that is face-centered cubic. It is also the only fcc transition metal widely used for constructional purposes. The other fcc transition metals Rh, Pd, Ir, and Pt are less abundant and have not been used as major construction materials. As such, in-depth investigations of their mechanical properties have not been undertaken.

TABLE 1
Recognized Aspects of Strain Aging

1. Yield Points
2. Strengthening
3. Discontinuous Yielding
4. Strain Rate Sensitivity Minimum
5. Ductility Minimum
6. Abnormal and Rate Dependent Work Hardening
7. Yield Stress Plateaus
8. Flow Stress Transients on Changes in Strain Rate

The principal purpose of the present investigation was to characterize the strain aging phenomena of commercially available Nickel 200. This alloy contains as its principal strengthening agent solid solution interstitial carbon (0.15 w/o maximum). To the best knowledge of the author, a complete classical static strain aging investigation has never been conducted using an interstitial solid solution fcc alloy.

A prime goal in the present investigation was to develop a quantitative model that could explain the kinetics and energetics of the return of the lower yield stress. Furthermore, the tensile behavior of Nickel 200 during constant strain rate tests conducted over a wide range of temperatures and strain rates was investigated in order to better define the dynamic strain aging phenomena in Nickel 200.

CHAPTER I
PREVIOUS INVESTIGATIONS

1.1 Static Strain Aging

1.1.1 Historical Aspects

It has been recognized for a long time that the yield phenomenon in iron and other bcc metals is closely related to the presence of interstitial impurity atoms such as carbon or nitrogen. Most strain aging investigations have centered about the iron and steel industry since the 1930s when the phenomenon in low carbon steel first became a major commercial nuisance.

The first metallurgical investigation of aging in mild steel was conducted by Davenport and Bain [3] in 1935, who noted that heterogeneous flow occurred in both annealed and deformed materials after having been "aged" by storing before working. Subsequent work by Gensamer and Low [4] in 1944 related the strain aging and yield point to the presence of trace amounts of nitrogen and carbon. Since the time of these early investigations, much interest has continued to center on iron and other commercially significant body-centered cubic metals such as vanadium [5], niobium [6], tantalum [7], and molybdenum [8]. At the present time, very little research effort has been directed to the study of static strain aging phenomena in face-centered cubic and hexagonal metals containing interstitial impurities.

1.1.2 Mechanisms of Static Strain Aging in Metals and Alloys

Three main dislocation pinning mechanisms have been postulated on the basis of experimental evidence in metals and alloys. These are Cottrell pinning, Suzuki locking and Schoeck locking.

In all of the previously mentioned investigations of bcc metals, the most plausible explanation for static strain aging is due to Cottrell and Bilby [9] who attributed the effect to the diffusion of interstitial atoms in solution (e.g., carbon, nitrogen, oxygen or hydrogen) to dislocations. Their concept relates the increase in flow stress and yield point return after aging to the migration of solute atoms to the tensile region about an edge dislocation. The effect of this segregation is to locally lower the strain energy of the system and to consequently stabilize the dislocation to the point where an increased flow stress is required to remobilize the dislocation or to generate mobile dislocations.

The Cottrell mechanism is of major importance in causing the return of the sharp yield point in steel while an increase in the steel's ability to work harden and a reduction in ductility (in the later stages of aging) are probably associated with precipitation of carbides and nitrides [10]. The major contribution of the Cottrell-Bilby work was to solve the problem related to the diffusion of an interstitial atom in the stress field of a dislocation. The solution predicts the time-temperature dependence of the rate of impurity migration as inferred from internal friction measurements [11]. Cottrell and Bilby derived the following relationship for $n(t)$, the number of atoms arriving at the dislocation in the time t per unit length,

$$n(t) = 3 \left(\frac{\pi}{2}\right)^{1/3} n_0 \left(\frac{ADt}{kT}\right)^{2/3} \quad (1)$$

where n_0 is the average number of solute atoms per unit volume and the parameter A is the interaction constant which describes the tendency for a solute atom or center of dilatation to be attracted by an edge dislocation's hydrostatic stress field, D is the diffusivity of the solute and k and T have their usual meanings. The principal characteristics of Cottrell pinning as manifested in the static strain aging experiment are (a) a $t^{2/3}$ time dependence of the lower yield stress return, and (b) an activation energy for the yield return approximately equal to that for the migration of interstitial solute atoms. The model assumes long range migration of solute and probably involves about 10^3 atoms jumps [12] (or a net rms displacement of 30 to 50b). An empirical result is that the increase in stress necessary to free a dislocation from its atmosphere as measured by $\Delta\sigma$ is directly proportional to the number of atoms, $n(t)$, which have arrived at the dislocation. Thus, the strain energy decrease associated with long range impurity migration is directly proportional to $n(t)$. This model with modifications [13,14] has survived for twenty-five years without its concepts being significantly altered. Excellent reviews of the Cottrell-Bilby theory are available in many places [15-19].

Suzuki [20] has pointed out that in face-centered cubic metals containing extended dislocations, a completely different form of interaction between dislocations and impurity atoms can exist. Since the stacking fault has a locally different crystal structure from the matrix, the solid solubility of impurities contained in the matrix can differ appreciably within the stacking fault and outside. Consequently a chemical potential exists across the fault, resulting in the binding of impurity atoms to the stacking fault. Pinning is a result

of the accumulation of solute at the fault. Thus, this type of interaction should be characterized by an activation energy due to solute migration. Unfortunately, while the magnitude of the locking stresses has been calculated and applied with some success to solid solution alloys, the kinetics of migration to the faults have not been studied [21]. Nickel has a stacking fault energy [22,23] of approximately 400 dynes/cm. The equilibrium separation [24] between two partial dislocations is estimated to be only $3b$. The magnitude of the yield point produced by segregation to stacking faults is related to the fault area. Hence, in other metals such as Ag-6 w/o Al [25] where faults are estimated to be $30b$ wide the effect is more important. Thus, one would not expect Suzuki locking to be a very important pinning mechanism in nickel [26].

The third type of pinning is sometimes called short range order locking and was proposed by Schoeck [27] and later expanded upon by Schoeck and Seeger [28]. Schoeck and Seeger considered a bcc lattice in which the concentration of interstitials is low enough to keep the interaction between interstitials small. Snoek originally proposed [29] that small atom impurities in solid solution occupy the octahedral interstices at the center of an edge or the center of a face of the unit cell in a bcc metal. Such sites have tetragonal symmetry since two of the six solvent atoms surrounding the interstitial site are closer than the other four. As a result, the octahedral sites may be classified into three groups depending upon which one of three mutually perpendicular $\langle 100 \rangle$ directions the two nearest neighbor solvent atoms are aligned along. Thus, the three types of interstitial sites correspond to the three directions of tetragonality and if no applied stress is acting, the three kinds of interstitial sites will be occupied by the same fraction

of interstitials; namely, one-third will be in each of the three types of sites. One may visualize each type of site occupied by an interstitial as a dipole. The principal axis of the tetragonal distortion gives the orientation of the dipole. If an applied (non-hydrostatic) stress is acting, the energy of interaction between the stress and the dipoles will in general depend on the orientation of the dipoles (i.e., the types of sites occupied by an interstitial atom). As a consequence, an applied stress will cause a redistribution of dipole orientations and the population of the sites with lower energy will increase, whereas the population of the sites with higher energy will decrease. This process is known as the Snoek effect [29] and it gives rise to a well established internal friction peak [30,31,32]. The activation energy associated with stress induced ordering of interstitial solute in bcc metals is normally that associated with diffusion of the impurity [33]. Schoeck [27] in 1956 pointed out that a similar redistribution of dipole orientations could be effected by the strain field of a dislocation. By such a process, the energy of the system is lowered in a period of time approximately that required for one interstitial atom jump and, therefore, the dislocation becomes locked. Whereas the locking due to atmosphere formation (Cottrell) requires diffusion of interstitials over long distances, the locking due to stress induced ordering of interstitial dipoles is accomplished merely by atomic rearrangement between neighboring lattice sites and, therefore, takes place in times which are orders of magnitude faster.

Schoeck and Seeger [28] examined the process in considerable detail in 1959. Starting with the interaction energy between the interstitial solute atoms and the dislocation and assuming the concentration of solute

was small, they showed that the line energy of a dislocation surrounded by a Snoek ordered atmosphere is decreased by an amount U_0 given by

$$U_0 = \frac{\pi c_0 A^2}{kT} \ln \frac{3LkT}{A} \quad (2)$$

where

c_0 = total concentration of interstitials

A = an interaction constant

L = cut-off radius

kT = thermal energy

They next derived that the extra applied stress, $\Delta\tau$, necessary to pull the dislocation from the ordered atmosphere is given by

$$\Delta\tau = \frac{U_0 kT}{2bA} \quad (3)$$

A more complete derivation of these results is carried out in the discussion relative to the carbon-vacancy pair (Section 4.2.4) and is related directly to pinning in Nickel 200.

The possible contribution to the rise in yield stress made by ordering of solute atoms in the stress fields of dislocations has generally been ignored probably because it occurs very quickly at the temperatures that have usually been investigated. Snoek ordering, however, can explain the rapid static strain aging phenomena observed by Wilson and Russell [34] in tensile tests on a low carbon steel and similar observations on a range of materials (for example, Carpenter on tantalum-oxygen [12] and niobium-oxygen [35]; Owen and Roberts [36] on martensite; Rose and Glover [37] in stainless steel). Support for this view comes from an investigation by Nakada and Keh [38] of rapid strain aging in iron-nitrogen alloy single crystals.

Wilson and Russell [34] verified that the rise in yield stress at 261°K in iron specimens (containing 0.039 w/o carbon) prestrained 4% was 63% complete in 100 seconds and noted that this time is in reasonable agreement with relaxation times observed in the case of the elastic after-effect due to the ordering of carbon in iron. Thus, the process is complete in roughly the jump time of a carbon atom. It must be noted that parts of their data were taken with a reduced applied load which was generally between 80 and 90% of the load at the end of prestrain. Aging while applying a load has been shown to influence the size of the yield point and depends strongly upon the fraction of the prestrain load that is used in aging [39,40,41,42,43]. A similar case occurs in the data of Nakada and Keh [38] who used single crystal Fe-0.1 at/o C and N in their investigation.

Although Quist and Carpenter [35] did not conduct the usual static strain aging experiments, their investigation of dislocation pinning in Nb-O alloys during internal friction measurements is noteworthy. They conducted their experiments between 273 and 313°K and attributed damping phenomena to the pinning of dislocations by Snoek ordering of oxygen interstitial atoms in the strain fields of dislocation line segments. They observed that pinning was effectively completed in a period of one oxygen atom jump time.

1.1.3 Summary of Important Mechanisms of Dislocation Locking During Aging

The two most important mechanisms of dislocation locking that may occur in metals containing dissolved interstitial impurities are related to (a) the Cottrell-Bilby model and, (b) the Schoeck-Seeger model.

The principal features of the Cottrell-Bilby model are

- (1) Solute atoms migrate toward the dislocation over long distances under the influence of the gradient in elastic interaction energy between the dislocation and the solute.
- (2) $t^{2/3}$ aging kinetics are predicted by the model and observed experimentally.
- (3) The activation energy for the yield return predicted by the model and observed experimentally is that for the diffusion of interstitial solute.

The principal features of the Schoeck-Seeger model are

- (1) Interstitial atoms with tetragonal strain fields reorient in the strain field of a dislocation.
- (2) The aging process by Snoek ordering is completed in approximately the time required for one atom jump.
- (3) The activation energy predicted by this model is that for diffusion of the interstitial solute.

1.1.4 Aspects of the Static Strain Aging Experiment

Figure 1 illustrates the mechanics of the classical static strain aging test for a specimen deformed in tension (or compression) at a constant strain rate. The initial prestrain and unloading cycle gives the specimen a known deformation history and internal state, i.e., a higher "fresh" dislocation density than that in the annealed specimen. If the material is immediately restrained after unloading, the stress-strain curve returns to the curve which would have been attained had the specimen not been unloaded. However, by aging under the proper conditions (e.g., higher temperature and/or longer times) a yield point occurs and is followed by a period of Lüders flow at constant load

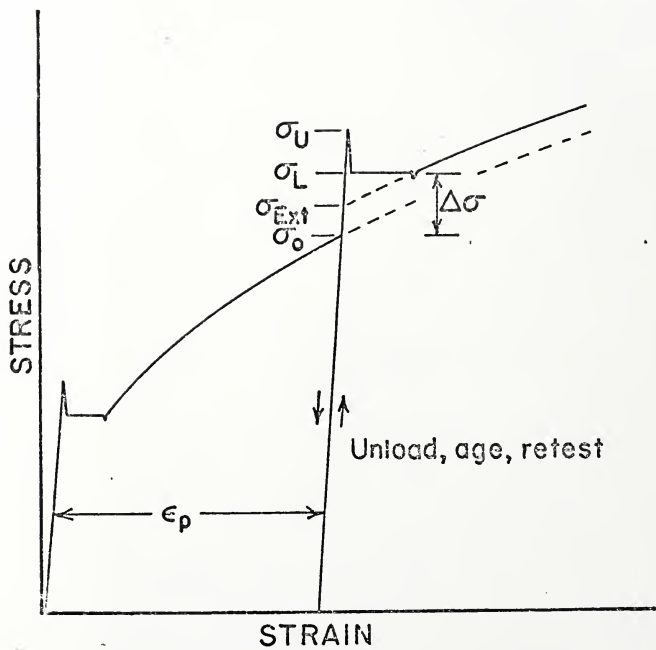


Figure 1. General aspects of the classical static strain aging test.

before work hardening resumes. In fact, the process of aging results in a gradual transition from a smooth reloading curve for very short aging times to a curve similar to that shown in Figure 1.

The important parameters of the reloading curve are σ_U , σ_L and σ_{Ext} , the upper yield stress, the lower yield stress and the stress increment obtained by extrapolating the post-yielding curve, respectively. For short aging times, σ_{Ext} is equal to σ_0 , the value of the stress before unloading. The extrapolated stress, σ_{Ext} , is determined by the intercept of the flow curve, i.e., that portion of the stress-strain curve where uniform strain hardening is present, with the pre-yield or "elastic" portion of the reloading curve. The experimental parameter, $\Delta\sigma = \sigma_L - \sigma_0$, is the parameter that is normally associated with strain aging as it is experimentally the easiest to determine.

Accompanying the return of the yield point is the reappearance of heterogeneous deformation, i.e., the passage of a Lüders band down the specimen gage length, at the lower yield stress, which is also characteristic of annealed metal. During the initial stages of aging, the lower yield stress increases with aging time as does the size of the Lüders strain. The rate of change of these properties generally increases with aging time and temperature. After aging for somewhat longer times, depending on the metal and its history, the variation of $\Delta\sigma$ and the Lüders strain with time in bcc metals becomes much slower, in many cases exhibiting a slight decrease with aging time.

1.1.5 Static Strain Aging Stages in BCC Metals

Five stages of aging during static strain aging have been identified for bcc metals containing interstitials. The first stage has been

explained on the basis of observations of very rapid returns of yield points in interstitial iron alloys [34,38,44] and internal friction experiments in other bcc metals [12,35]. The explanation is that very rapid pinning may be attributed to stress induced ordering of interstitials in the strain fields of dislocations as previously modeled by Schoeck and Seeger [28] (Section 1.1.2).

The last four stages have been explained [10,45,46] on the basis of a Petch equation of the form

$$\sigma = \sigma_i + 2k_y d^{-1/2} \quad (4)$$

where σ is the lower yield stress, σ_i the lattice friction stress, k_y a dislocation locking parameter and $2d$ is the grain size. This equation was developed originally by Petch [47,48,49] in order to provide a method of separating the factors contributing to the lower yield strength of polycrystalline iron. During the Lüders band propagation, it was believed that unpinned sources release many dislocations which pile up at the grain boundaries. Thus, a feature of the model is the grain size and the boundaries are pile-up sites which act as stress concentrations. The pile-ups are controlled by the grain size and act in conjunction with the applied stress to unpin nearby dislocations in a neighboring grain. The friction stress is represented by σ_i and is the stress to move an unbound or free dislocation through the lattice.

Rosenfield and Owen [50] formulated the aging phenomena in terms of an equation of the form

$$\Delta\sigma = \Delta\sigma_H + 2k_y d^{-1/2} \quad (5)$$

where $\Delta\sigma$ is the gain in the lower yield stress after aging, $\Delta\sigma_H$ the gain in the hardening component of the lower yield stress increase, as determined by extrapolating the load-time curve after the Lüders strain back to the reloading curve, and k_y and d have the usual meanings.

Szkopiak [6] performed static strain aging experiments on niobium-oxygen alloys and separated the two components of the yield stress increase of Eq. 5 as shown in Figure 2. In Figure 2a, the typical return of the yield stress experiment on a bcc metal shows that at small aging times the increase in lower yield stress is very rapid (depending upon temperature of aging) and approaches a maximum. At longer aging times, the lower yield stress increment shows a slight decrease. In Figure 2b, the two components of $\Delta\sigma$ in Eq. 5 are shown separately.

The five stages of aging that have been observed in alloy systems such as Nb-O [6,35], Fe-C [34,45,46], and Fe-N [38,51,52] alloys and probably occur in Ta [12,18], V [5], and Mo [8] as well are:

Stage I: This stage is observed clearly only at low temperatures since locking occurs by stress induced ordering of interstitials in the strain fields of dislocations and occurs within the time span of approximately one solute atom jump. The strength of pinning agrees reasonably well with the Schoeck-Seeger model.

Stage II: In this stage, k_y reaches a maximum and remains constant. The lower yield stress reaches a maximum and the Lüders strain increases very rapidly. The rationale for this stage is that the formation of Cottrell atmospheres takes place during aging and upon reloading dislocations become unpinned from their atmospheres.

Stage III: Further increases in the lower yield stress are due to an increase of the $\Delta\sigma_H$ parameter. In this stage, the Lüders strain remains

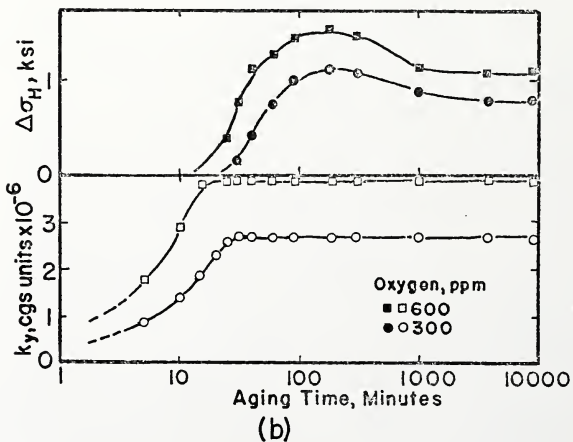
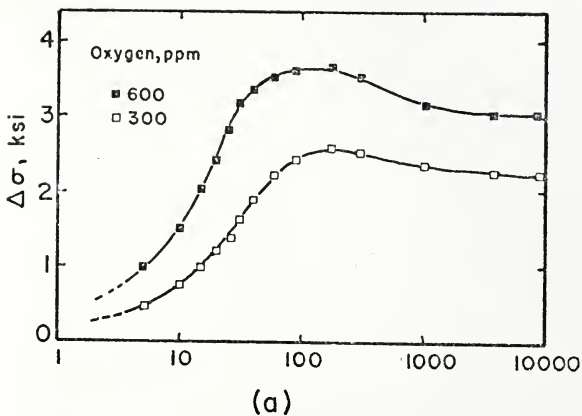


Figure 2. An example of the stages of the yield return in Nb-O alloys [8]; (a) the increase in $\Delta\sigma$ with time, (b) the components of $\Delta\sigma$ and their dependence on time.

nearly constant as the yield stress increases and enhanced strengthening occurs. The principal rationale for this hardening is that dislocations have been aged to the extent that they tend to remain immobile or pinned upon subsequent reloading. Thus, new or additional dislocations are created and the yield stress continues to increase.

Stage IV: During this stage, solute continues to be accommodated in the strain field of dislocations but no longer effects an increase in $\Delta\sigma$. Hence, $\Delta\sigma$ remains approximately constant.

Stage V: As more and more interstitial solute segregates to dislocations, a condition of "overaging" is satisfied and precipitates may form; hence, the loss of a coherent strain field or the robbing of solute near dislocations and a mild decrease in the hardening component.

The above stages of static strain aging appear to hold true for most of the body-centered cubic metals containing interstitial oxygen, carbon or nitrogen. However, in the case of face-centered cubic metals containing interstitial impurities no complete investigations of the behavior of the return of the lower yield stress have been carried out.

1.1.6 Static Strain Aging in Nickel and FCC Alloys

Among the fcc commercial alloys, nickel containing carbon is probably the most significant where an interstitial (carbon) is deliberately added to improve mechanical properties. Other than pure nickel, only fcc multicomponent alloys such as the austenitic stainless steels [37,53,54] contain carbon for similar reasons and exhibit mechanical properties similar to nickel-carbon alloys.

There exists some experimental evidence related to the static strain aging of nickel-carbon alloys. In particular, two short notes were

published by Macherauch et al. [55] and by Macherauch and Vöhringer [56] regarding static strain aging in Ni-0.05 w/o C after prestraining slightly beyond the initial yield plateau. Their data were plotted by this author and an approximate $t^{1/3}$ or $t^{1/4}$ time dependence of the lower yield stress return was exhibited. They did not speculate on the kinetics; however, they determined an activation energy of 10.2 ± 2 kcal/mole in agreement with the activation energy for diffusion of hydrogen in nickel (see, for example, Boniszewski and Smith [57]).

The only other investigation relating to nickel-carbon alloy is due to Sukhovarov [58] and Sukhovarov et al. [59]. Using compression specimens deformed at room temperature and aged between 433 and 493°K for various times, they deduced with apparent difficulty (because serrated flow occurred) that the average activation energy was 30.7 kcal/mole, somewhat lower than the carbon migration energy in nickel. This author plotted their lower yield stress data and noted that $\Delta\sigma/\Delta\sigma_{\max}$ varied approximately as $t^{0.3}$. They conclude (incorrectly, it is believed) that the Cottrell-Bilby model explains the rise in $\Delta\sigma$ and that probably the formation of precipitates eventually occurs; they never observed this aspect.

In addition, since serrated flow occurred in the investigation of Sukhovarov [58], it is probable that the data were scattered because the lower yield stress was not as clearly defined as in the present investigation where yield point measurements were made under conditions precluding serrated flow. On this basis, their data should be used judiciously.

Hydrogenated nickel exhibits strain aging behavior [57,60-65] when deformed below room temperature. Much effort has been directed toward

understanding fracture, ductility, and other embrittlement related phenomena attributable to hydrogen. Also, serrated flow [57, 60-65] is exhibited in hydrogenated nickel between approximately 130 and 225°K [65] at a nominal strain rate of 10^{-4} s^{-1} . The kinetics of static strain aging in hydrogenated nickel were very briefly investigated by Boniszewski and Smith [57] and they concluded that the Cottrell-Bilby model can account for static strain aging of charged specimens. However, they did not speculate on the exact kinetics that the experimental data may have followed.

Marek and Hochman [66] have demonstrated the existence of static strain aging effects in AISI 316 alloy and related it to the approximate activation energy for diffusion of interstitial carbon in austenite. However, the effect was most marked in the micro-yield region (0.01% proof stress) with no effect on flow stress after yielding, UTS, or elongation, which is indicative of a low interstitial/dislocation interaction energy.

1.2 Dynamic Strain Aging

Dynamic strain aging (DSA) is a feature exhibited in most commercial metals and alloys [1]. In general, aspects of DSA have created very little interest in the past, probably since in steel it exhibits its most significant effects over a temperature range around 450°K where steel is not normally worked. Other bcc metals such as titanium, tantalum, niobium and vanadium exhibit DSA over a temperature range where these metals are most needed [1].

As with steel, nickel containing carbon exhibits its effects at relatively low temperatures (300 to 500°K, roughly). Early investigations by Sukhvarov and Kharlova [67] confirmed that dynamic strain aging

occurs in nickel when alloyed with small amounts of carbon. In a subsequent investigation Popov and Sukhovorov [68] indicated that the apparent activation energies associated with the appearance and disappearance of serrated flow are 20 and 33 kcal/mole, respectively. No conclusion regarding the very low activation energy for the onset of serrated flow was ventured. On the other hand, Nakada and Key [51] have indicated that the onset activation energy in Ni-C alloys is 15 ± 2 kcal/mole and that for the disappearance of serrations is 26 ± 4 kcal/mole. It is a well established experimental fact that the activation energy associated with the diffusion of carbon in nickel is approximately 35 kcal/mole (see Table 2). Generally, in interstitial alloys the activation energy for the onset of serrated flow is associated with the diffusion of impurity atoms and is made on the basis that when the velocity of dislocations is approximately equal to that of the velocity of the diffusing impurity atoms, a drag or pinning of dislocations occurs. Thus, the pinning as observed through the serrated flow phenomenon is assumed to be controlled by the diffusion of impurity atoms just as in the static strain aging experiment. By plotting $\log \dot{\epsilon}$ versus $1/T$, where $\dot{\epsilon}$ is the strain rate at temperature T where serrated flow is first observed, an activation energy may be deduced. The values of 15 ± 2 and 20 kcal/mole for the onset of serrated flow determined by the preceding authors are much too small to be related to the diffusion of carbon in nickel. Popov and Sukhovorov [68] made no conclusions regarding this apparent anomaly. Nakada and Keh, however, ventured that pipe diffusion of carbon along dislocation cores controls serrated flow in nickel.

TABLE 2

The Diffusivity of Carbon in Nickel

$\frac{D_0}{\text{cm}^2/\text{sec}}$	Q kcal/mole	<u>Technique</u>
0.048	34.8	Elastic and magnetic aftereffect [69]
0.13	34.5	Radioactive tracer [70]
0.1	33.0	Radioactive tracer [71]
--	38.5	Thermogravimetric [72]
--	39.7	Thermogravimetric [72]
--	32.3	Magnetic aftereffect [73]

Regarding the activation energy associated with the disappearance of serrations, Kinoshita et al. [74] proposed that this value may represent the sum of the activation energies for the diffusion of solute plus the binding energy of solute atoms to dislocations. On this basis, Nakada and Keh [51] have deduced a binding energy of 11.0 kcal/mole (0.5 eV) for a carbon atom to a dislocation in nickel assuming that serrated flow in Ni-C alloys is caused by carbon directly. Popov and Sukhovarov [68] attributed their value of 33 ± 3 kcal/mole (1.4 eV) for the disappearance of serrations to a combination of creep processes coupled with Cottrell atmosphere formation.

Other than the above nickel-carbon studies and the experimental work on hydrogenated nickel [57,60-65] which shows strain aging, no other investigations of the effect of interstitials on the stress-strain and work hardening behaviors in pure face-centered cubic metals have been conducted. However, some face-centered cubic ferrous alloys appear to possess mechanical properties similar to those of nickel-carbon alloys. In an investigation by Jenkins and Smith [54] complications due to substitutional alloying elements such as Cr occurred. Nevertheless, AISI 330 stainless steel (Fe-15Cr-33Ni-0.4C), exhibits similar dynamic strain aging trends. A calculation of the energies for the onset and disappearance of serrations revealed that 26.6 and 62.0 kcal/mole are the onset and termination activation energies. They indicated that the onset activation energy is very close to that for vacancy migration in Fe-30 Ni. As the Portevin-Le Chatelier effect is absent for low carbon content, they conclude that vacancies alone are not responsible and that carbon-vacancy pairs account for the observed activation energy. Mention was not made of the exact mechanism for the pinning during serrated flow. A similar argument appears to apply in the case of Nickel 200.

Other strain aging effects occur in face-centered cubic alloys but these arise mainly from the diffusion of substitutional solutes and are outside the scope of this dissertation.

1.3 Work Hardening in Metals and Alloys

In studying the work hardening of metals and alloys it is desirable to determine the mechanisms that control the rise in flow stress. In general, this involves relating the macroscopic behavior to changes in the microscopic structural features of the metal. For example, observations of slip line lengths or dislocation structures can supplement an explanation of work hardening.

From the macroscopic point of view, polycrystalline stress-strain curves have been shown to be generally piece-wise continuous [75-81]. For example, Figure 3 shows schematically that a polycrystalline face-centered cubic metal may deform so as to show discontinuities in its stress-strain behavior. Zankl [75] and others [76-81] have shown that these stages can be correlated very well with deformation processes. According to his experimental work [75] the identifiable stages are related to the following processes:

1. The Transition Stage. This extends from zero plastic strain to approximately 0.1%. In this stage, multiple slip starts first in the largest grains and then spreads into neighboring grains.
2. Stage I. This begins when all grains have begun to deform with slip still involving multiple slip systems. Stage I in polycrystals is thus basically different from the easy glide Stage I of face-centered cubic crystals. It ends at approximately $\epsilon_p \approx 1.0\%$.

3. Stage II. Here slip tends to occur predominantly on a single (primary) system but with interaction from secondary systems. The deformation is accordingly analogous to that in Stage II of a fcc single crystal. Large grains may break down into several regions [80] with different primary systems. This stage extends to about $\epsilon_p \cong 5.0\%$ in pure fcc metals such as copper and nickel.

4. Stage III. As in fcc single crystal deformation, this stage is controlled largely by dynamic recovery and has been associated with cross slip [82].

In general, polycrystalline stress-strain curves appear to be continuous in shape and the stages difficult to identify on such curves. This is in marked contrast to single crystal stress-strain curves which often exhibit well-defined stages. A sensitive empirical method [83] for detecting polycrystalline stage behavior has been developed as a logical projection of previous empirical analyses [84-92]. This is based upon the assumption that each stage of stress-strain behavior can be reasonably described by a modified Swift [92] equation:

$$\epsilon = \epsilon_0 + c\sigma^m \quad (6)$$

where σ is the true stress, ϵ the true plastic strain, m the work hardening exponent and ϵ_0 and c are constants.

One may solve very simply for the parameters in Eq. 6 by plotting $\log \theta$ versus $\log \sigma$ where $\theta = \frac{d\sigma}{d\epsilon}$. A schematic example of such a plot is shown in Figure 4 for a typical face-centered cubic metal such as copper or nickel. Any straight line on this type of plot has an equation of the type:

$$\log \theta = (1-m) \log \sigma - \log cm \quad (7)$$

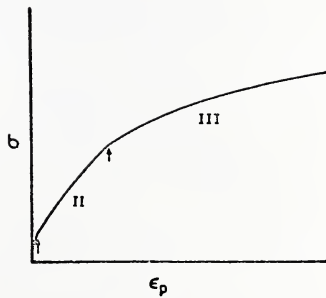


Figure 3. Schematic example of stage behavior in polycrystalline fcc metals.

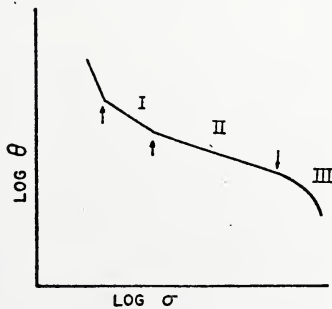


Figure 4. Schematic description of the work hardening behavior in a metal using a $\log \Theta$ - $\log \sigma$ plot.

Thus, the value of m typically characterizes the power law relationship of Eq. 6. An m equal to one is a linear stress-strain curve and a $\log \Theta$ versus $\log \sigma$ plot would show a line with a zero slope; a parabolic stress-strain curve would show a $(1-m)$ -value of -1.0 (i.e., $m=2$) and so on. High m values correspond to curves with a great deal of curvature, i.e., very rapidly decreasing work hardening rate with increasing stress as in Stage III when dynamic recovery processes reduce the work hardening rate very rapidly with continued deformation. All other parameters held constant, a high value of m for a single stress-strain curve would, in general, imply that the material has low ductility, even though the material might possess a reasonably high ultimate strength. However, it should be noted that a three or four stage stress-strain behavior could well lead to a combination of both high strength and high ductility depending upon the m values of the various stages and the extent of a particular stage during deformation.

It should be noted that the stage behavior observed by using Eqs. 6 or 7 is within limits independent of the empirical power law equation used. For example, an analysis based upon the Crussard and Jaoul method [87-89] using a $\log \sigma - \log \epsilon$ diagram shows that discontinuities occur at the same places on the stress-strain curve as determined by using a $\log \Theta - \log \sigma$ diagram.

In the current investigation, interstitial solute concentration was the principal alloy variable known to affect stress-strain behavior. Interstitial elements tend to significantly increase the strength of a metal while generally decreasing its ductility. This in turn affects the stage behavior of the parent metal.

Another factor influencing the stage behavior of metals and alloys is the stacking fault energy. This intrinsic property of a metal or alloy determines the separation distance of the two partial dislocations of an extended dislocation [93].

For high SFE metals like nickel [22,23,94] or aluminum [93] the separation distance is small and mobile dislocations may be assumed to approach total dislocations. In low SFE metals and alloys such as Ni-40Co and Ni-60Co [94] this distance becomes appreciable and the partials may be separated by a wide band of stacking fault. By effectively varying the geometry of the dislocation by lowering its stacking fault energy, the deformation behavior might be expected to change as well. Thus, it would appear that in a low stacking fault energy metal a dislocation effectively loses a degree of freedom of movement by virtue of its assuming a planar character. This should reduce the ability of the material to undergo dynamic recovery involving either cross-slip or climb.

One may also view a stacking fault as a building block for a deformation twin. In general, twin boundary energies are lower in lower stacking fault energy metals. This observation is in agreement with the fact that twinning plays a greater role in the deformation behavior of metals and alloys [95,96] with low stacking fault energies. Twinning was not observed in the present investigation.

1.4 Anelastic Phenomena in Nickel and FCC Ferrous Alloys

Considerable research has been performed for many years on the effects of interstitial solutes on the strain aging of body-centered cubic metals and alloys [2]. In addition, much emphasis has shifted

toward examining a variety of internal friction effects (such as the Snoek effect, the cold-work peak and dislocation damping behavior) that can be correlated closely to strain aging phenomena [97].

In contrast, however, there exists but a dearth of strain aging and internal friction studies of interstitial solid solutions of face-centered cubic metals. The reason for this lack of interest probably stems from the fact that in terms of the mechanical behavior of these alloys, the interstitials apparently cause a less dramatic effect on the mechanical properties. In addition, fcc metals are not expected to exhibit a Snoek peak because of site symmetry [30,32,98,99].

Very different specific mechanisms for the observed relaxation peaks in fcc metals and alloys have been suggested by various authors. Adler and Radeloff [99] reviewed the types of defects which could account for internal friction in fcc metals and alloys:

- (1) interstitial-solute clusters which have noncubic strain fields [30,98];
- (2) interstitial-substitutional solute clusters in which the interstitial reorients preferentially under stress if it is a near neighbor to an immobile substitutional solute [98,99];
- (3) interstitial-vacancy complexes of different types, i.e., Wu and Wang [100] suggested a defect consisting of one interstitial occupying a vacancy with a nearest neighbor interstitial in its normal site.

Within each category listed above are many possible specific combinations which could in principle cause a relaxation effect.

There is evidence for relaxation due to carbon pairs in both Ni and the fcc allotrope of Co, and for oxygen pairs in Ag [101]. The

existence of an internal friction peak associated with dissolved C in Ni was first reported by Kê and Tsien [102] and further investigated by Kê, Tsien and Misek [103]. The peak is quite small and occurs at 523°K for a frequency of 1 Hz. By application of a saturating magnetic field, the existence of the peak was shown to be unrelated to the ferromagnetic nature of the sample. Further, the peak was found to decline in strength as the carbon precipitated from solution. Kê and Tsien pointed out that unassociated C atoms, located at the body-centered position of the fcc structure and in the equivalent positions midway along the cube edges, could not be responsible for the relaxation, since the symmetry of such defects is cubic. After Tsien [104] found in later work that the relaxation strength varied essentially as the square of the carbon content in solution, it became evident from mass-action considerations that carbon pairs were the responsible defect.

Diamond and Wert [69] also investigated the diffusion of carbon in nickel utilizing elastic aftereffect measurements above and below the Curie temperature and noted no discontinuity in carbon diffusivity. Hence, magnetic transformation effects do not affect carbon diffusivity. In addition, they concluded that the elastic aftereffect is due principally to interstitial diffusion of C-C pairs in agreement with the results of the previously mentioned group of Chinese investigators [102-105]. The simplest interstitial pair configuration in their view consists of two atoms occupying nearest neighbor octahedral sites which are the largest for fcc metals, e.g., the two sites $\frac{1}{2}00$ and $0\frac{1}{2}0$. The stress induced reorientation of such pairs (designated 110 pairs) which gives rise to anelastic effects, is the result of one of the atoms jumping into an unoccupied nearest neighbor interstitial site. A summary

of Ni-C diffusion data is presented in Table 2. It should be noted that all methods agree reasonably well with an activation energy of 35 kcal/mole for the migration energy of carbon in nickel. No distinction is made in the last four references cited in the table concerning the nature of the mobile species, e.g., dicarbon complexes.

C.T. Tsien [104] considered the effect of impurities on an internal friction peak in a carburized 18.5 w/o manganese steel. The principal experimental observation was that the internal friction peak height varies linearly with carbon content. It was proposed that the addition of Mn to Fe-C alloys may reduce the opportunity of forming carbon-carbon atom pairs and there may be greater probability of forming Mn-C pairs instead. Thus, in high manganese steels the internal friction peak is not attributed to rotation of the carbon atom pairs but due to that of carbon-manganese pairs. As a result, the height of the internal friction peak was observed to be directly proportional to the carbon content.

This brings us to the point of the possible mechanism involved in Nickel 200 which has 0.18 w/o Mn and smaller amounts of iron and copper. Presuming a pair mechanism (in order to obtain a tetragonal defect which would account for an internal friction peak) one might presume a possibility of C-C atom pairs or C-Mn atom pairs causing the static strain aging effects. However, in the investigations previously cited, not one was conducted using a deformed metal and this factor may be an important consideration. Hence, a third and possibly fourth species may be involved, namely, the vacancy and the self-interstitial. It has been demonstrated by Seitz [106] that in fcc metals the predominant defect produced during plastic deformation is the vacancy. Table 3 shows the data of

a number of authors [107] who have described the vacancy concentration during plastic deformation for a variety of fcc metals and alloys as

$$c_v = K\epsilon^n \quad (8)$$

where c_v = vacancy concentration (atom fraction)

ϵ = true strain

K = proportionality constant

$n \approx 1$

The principal experimental technique used to determine c_v involves monitoring resistivity changes during deformation and subsequent annealing of the specimens [106,108]. The identification of the defects annealing out during each recovery stage has been the subject of extensive previous work in nickel. Studies have been made of the resistivity recovery spectrum following neutron irradiation, electron irradiation and quenching from high temperatures [109,110]. In addition, changes in magnetic properties have also been studied in conjunction with the resistivity recovery process [73,111,112].

On this basis [108] cold rolled nickel behaves as

$$c_v = 2.1 \times 10^{-4} \epsilon \quad (9)$$

In addition, it has been estimated that approximately eight times as many vacancies as self-interstitials are generated.

Point defects are generally believed to be generated during plastic deformation by two basic mechanisms [31,113]: (a) nonconservative motion of jogs on screw (or mixed character) dislocations and (b) recombination of dislocations containing edge type components. The second mechanism is due to annihilation of edge dislocations and may

TABLE 3*

Estimates of the Rate of Vacancy Production
During Plastic Deformation

Material	K	Type of Deformation
Cu	1.9×10^{-4}	tensile elongation
Ni	2.1×10^{-4}	cold rolling
Ni	12×10^{-4}	shock forming
NaCl	1×10^{-4}	compression
70-30 Brass	5.9×10^{-4}	tensile elongation
Au	2.9×10^{-4}	tensile elongation
Al	0.2×10^{-4}	tensile elongation

* From Ulitchny and Gibala [107]

not be important relative to the first mechanism in the production of vacancies until Stage III deformation occurs. The relation between vacancy concentration and strain is also probably only valid to strains of the order of 10%. It has been noted that the vacancy concentration tends to approach a saturation value at large strains [108]. Thus, vacancies may play an important role in deformed and aged nickel.

As concerns the manganese impurity in Nickel 200, a qualitative argument may be made against the existence of Mn-C complexes as opposed to C-V complexes. The gram atomic volume of Mn [114] is 7.39 cm^3 while that for Ni [115] is 6.59 cm^3 . Thus, a Mn atom is only approximately 4% oversized on a nickel lattice site. In an interstitial octahedral lattice site, a carbon atom is about 14% oversized. Relative to binding to a vacancy, the carbon atom should provide a stronger compressional center of dilatation than the manganese atom even though in the former case an octahedral interstitial site is occupied and in the latter a normal lattice site is occupied. Hence, the binding energy of a vacancy to a carbon atom should be higher than that of a manganese atom to a carbon atom or a vacancy. In addition, Nickel 200 contains approximately three times less manganese than carbon on an atom fraction basis.

The value for the diffusion energy of a vacancy through a lattice is very sensitive to the presence of impurities which tend to slow down a freely migrating vacancy because of binding to impurity atoms [116,117]. In pure nickel, the vacancy migration energy is between 0.8 and 0.9 eV and for impure nickel [117,118] (99.9% pure plus an unspecified amount of carbon) is approximately 1.1 eV. Thus, one may deduce that the approximate binding energy of carbon to vacancies is between 0.2 and 0.3 eV. In short, the carbon-vacancy interaction could cause the formation of a

defect complex which might cause strain aging in Nickel 200. It is not clear whether or not dicarbon-vacancy defects may be completely ruled out as a possible complex causing strain aging.

An excellent discussion concerning internal friction and strain aging to carburized ferrous austenite by Ulitchny and Gibala [107] suggests that the relaxation phenomena in these alloys are attributable to the rotation of carbon-vacancy pairs. Their conclusion is based upon experiments in which vacancies were produced in stainless steels by (1) quenching, (2) deformation and (3) irradiation. These processes have in common that they (a) increase the vacancy concentration in the metals, (b) increase the observed peak heights of the bound pair peak and (c) increase the peak heights in proportion to the relative numbers of vacancies they are anticipated to produce. These alloys possess mechanical properties quite similar to nickel-carbon alloys. In addition, the diffusivities of both carbon atoms and vacancies in the austenitic stainless steels are similar to those in nickel-carbon alloys [107] suggesting that a similar mechanism in the present investigation of Nickel 200 should not be ruled out.

CHAPTER II
EXPERIMENTAL PROCEDURES

2.1 Materials

Nickel 200 bars of 0.75 inch diameter were obtained through a local supplier and from the International Nickel Company. These two heats had slightly different compositions (Table 4); the mechanical properties as a result were somewhat altered, albeit small. All static strain aging experiments were conducted utilizing Nickel 200^b. The standard tensile tests were conducted using Nickel 200^a. This procedure was followed in order to minimize possible scatter of the data, particularly in the static strain aging experiments. In addition, Nickel 270 was also purchased; its composition also appears in Table 4.

Nickel 200 contains approximately 0.18 w/o Mn and 0.10 w/o C. The highest equilibrium solubility limit [119] for the nickel-carbon system is 0.27 w/o carbon. The room temperature solubility limit of carbon in nickel is only 0.02 w/o [120]. Also, nickel carbides are unstable in Ni-C alloys [119,121]. The development of visible graphite in nickel during cooling is generally agreed to occur very slowly. The present specimens, which were furnace cooled from the annealing temperature (1073°K) at a rate of approximately 2.0°/s, are believed to have retained all of the carbon in excess of the equilibrium solubility in solution since graphite was not observed either by optical or transmission electron microscopy of the annealed specimens.

TABLE 4
Alloy Compositions

	<u>Ni 270</u>	<u>Ni 200^a</u>	<u>Ni 200^b</u>
C	0.01	0.08	0.10
Mn	<0.001	0.27	0.18
Fe	0.002	0.05	0.01
S	<0.001	0.005	0.005
Si	<0.001	0.06	0.04
Cu	<0.001	0.01	0.01

All other impurities less than 100 ppm each.

2.2 Experimental Techniques

2.2.1 Swaging

The 0.75 inch (19.1 mm) bar stock of all the materials were cold swaged in a Model 3F Fenn rotary swaging machine to a diameter of 0.25 inch (6.4 mm). Intermittent annealing was not necessary. The resulting swaged bars were machined into threaded-end specimens with a nominal reduced section of 0.8 inch (20mm) and a gage diameter of 0.15 inch (3.8 mm).

2.2.2 Annealing

Annealing was accomplished in a Vacuum Industries Minivac furnace assembly. This unit utilizes a resistance heated tantalum element. Pressures as low as 10^{-3} millitorr can be maintained. No cold trap was used. All Nickel 200 specimens were annealed for 30 minutes at 800°C (1073°K); Nickel 270 specimens were annealed for 32 minutes at 595°C (868°K). These treatments resulted in specimens with a mean grain intercept of approximately 22 μ M. Annealing twin boundary intercepts were not counted in obtaining this result.

2.2.3 Specimen Profile Measurements

A Jones and Lamson Optical Comparator capable of measuring to 0.0001 inch (2.5 μ M) in the vertical and 0.001 inch (25 μ M) in the horizontal directions was used to measure the profile of as-annealed specimens. For all tests a specimen gage length was assumed to be identical to its reduced section and was determined to within \pm 0.005 inch (0.13mm) with experience.

2.2.4 Tensile Testing

All tensile testing was performed on two Instron machines (Model TT-C and Model FDL of 10,000 and 20,000 pound capacities, respectively). The standard crosshead speed was 0.02 inch/minute resulting in a nominal specimen strain rate of $4.2 \times 10^{-4} \text{ s}^{-1}$. Three additional strain rates were also employed with the Nickel 200 specimens. All tests were conducted between 77 and 900°K. Above 297°K tests were carried out in a capsule using commercial purity argon gas. At no time was oxidation visible on the specimen surfaces. Below ambient temperature, liquid nitrogen (77°K), dry ice-acetone (196°K), or ice-water baths were employed.

Load-time curves were processed to yield true stress versus true plastic strain curves as well as the slope of these curves as a function of stress or strain. The stage behavior of the specimens was analyzed [83]. In brief, the procedure involves the plotting of $\log \dot{\epsilon}$ versus $\log \sigma$ and identifying portions of the curves through which straight lines may be passed. Each linear interval is assumed to represent a stage. This assumption was tested against results of Zankl [75], Schwink and Vorbrugg [77] and others [76,78-81] and a good correlation was obtained between stages determined in this manner and the method of Zankl and others using different plotting and metallographic procedures. To each linear region a different set of parameters (m, c, ϵ_0) may be deduced corresponding to the Swift [92] equation

$$\epsilon = \epsilon_0 + c\sigma^m \quad (10)$$

2.2.5 Static Aging Experiments

Annealed tensile specimens were prestrained approximately 5% to a stress level of 38.5 ksi (265 MPa) at 273°K and immediately unloaded,

removed from the testing jig and immersed in a silicon oil bath at 473, 448, 428 and 408°K or in a boiling water (distilled) bath for times as long as 2×10^6 seconds (approximately two weeks). Control of the constant temperature baths was held to within approximately one-half degree. Upon completion of the aging treatment, the specimen was removed and quickly quenched into cold water and tested immediately. The reloading temperature for the static strain aging tests was 273°K as in the prestrain. It was recognized early in the investigation that at room temperature and a strain rate of $4.2 \times 10^{-4} \text{ s}^{-1}$ (the rate corresponding to a crosshead speed of 0.02 inch/minute, standard at this laboratory), discontinuous flow occurred in Nickel 200. To alleviate this feature it was decided to conduct the prestrains in ice-water baths at a rate of $4.2 \times 10^{-3} \text{ s}^{-1}$. This had the additional benefit of producing a stable and reproducible lower yield stress plateau and, in addition, the ice-water bath assured that specimens were at the test temperature after removal from the high temperature aging baths.

Quite apparent from the start was the fact that specimen alignment offered a problem. Upon removal and replacement of a specimen in the tensile jig, it was evident that exact repositioning was difficult and uncertain. Therefore, on restraining a specimen after aging it, a small bending moment normally develops which may cause yielding to occur nonuniformly across the gage section of the specimen. The result is that the upper yield point as observed on the machine chart was usually absent. As a consequence all data reported are lower yield stresses. Compilation of the data included interpreting the Lüders extension as the chart displacement which occurred at constant load

(Figure 5). This method proved to provide the most consistent set of data and tended to alleviate apparent alignment or reloading displacements. Occasionally (perhaps 10% of the time), a yield point was observed and the data fell consistently in line with other Lüders extension data recorded by the former method.

The latent hardening achieved during long term and high temperature aging treatments was computed by linearly extrapolating the post-yielding curve back to the reloading line as demonstrated in Figure 5. This method also proved consistent. However, in most cases of short aging times or low temperature aging, the extrapolated stress fell below the prestrain value. This is physically unreasonable and is attributed to alignment effects which generally eliminate the yield point as mentioned previously and may cause the extrapolations to come back to the reloading curve somewhat low. However, the resulting data, again, proved to be consistent.

As an example of typical experimental results, Figure 6 shows a series of load-time curves which were obtained after prestraining a series of specimens at 273°K to 5%, aging at various times at 408°K, and restraining at 273°K. Figures 6b and 6d show examples of partial yield points that were obtained in a few cases during the present investigation.

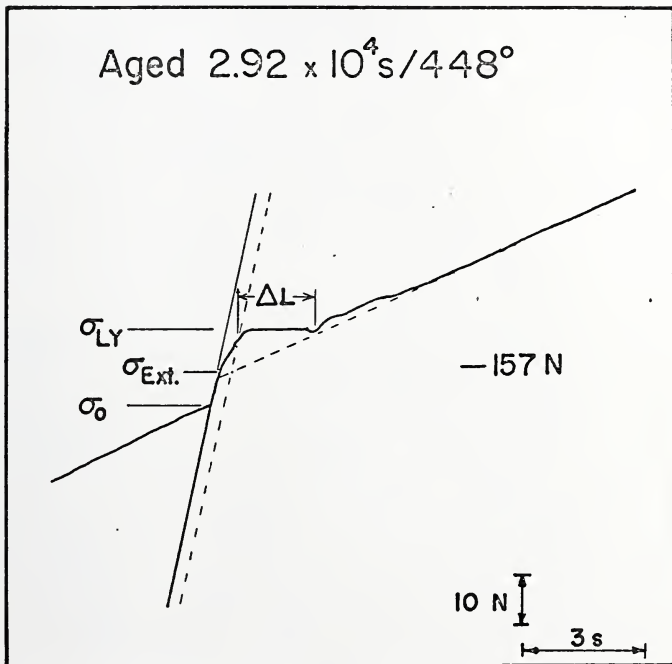


Figure 5. Illustrating the method used to determine the aging parameters ϵ_L , $\Delta\sigma = \sigma_{LY} - \sigma_0$ and $\Delta\sigma_H = \sigma_{Ext.} - \sigma_0$. The dashed loading line indicates the approximate loading line which would have been observed in the absence of misalignment of the test specimen.

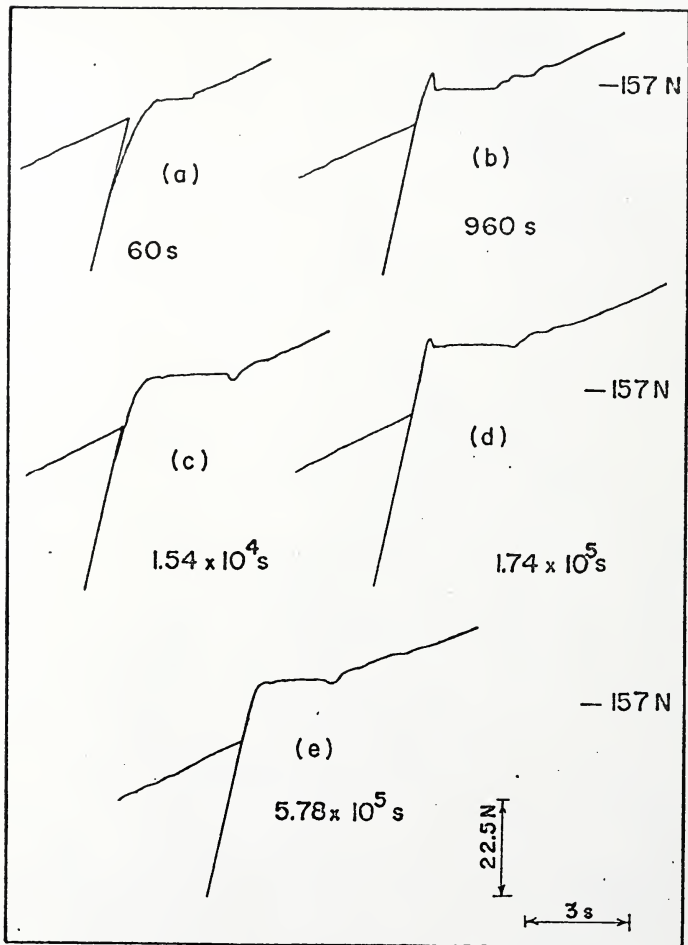


Figure 6. Selected load-time curves obtained after prestraining a series of specimens 5% at 273°K, aging at 408°K for the times indicated, and restraining at 273°K.

CHAPTER III
EXPERIMENTAL RESULTS

3.1 The Behavior of the Lower Yield Stress Increase, $\Delta\sigma$

Figure 7 illustrates the dependence of the lower yield stress increment, $\Delta\sigma$, on time and temperature over five decades of time and at five temperatures. The principal features of Figure 7 are

(1) The curves appear to approach a common value at small times. It would seem that the data obtained at the higher aging temperatures and for very short aging times are influenced by the time required to heat the specimen to temperature. This was confirmed by assuming a fixed heat-up time and displacing the curve (at each temperature) to shorter aging times. Thus, a heating time of approximately 40 to 60 seconds straightens out the start of the higher temperature curves to approximately the same linear dependence as exhibited by the 373°K curve. In addition, a simple heat transfer calculation indicated that a time constant of approximately 40 to 60 seconds should describe the specimen heat-up time. The dashed lines in Figure 7 show the approximate corrections necessary to account for heating the specimens in the baths.

(2) Each $\Delta\sigma$ curve shows a roughly linear increase with $\log t$ for times before reaching the maximum in $\Delta\sigma$.

(3) All curves show a well-defined peak whose height increases slightly, the lower the aging temperature.

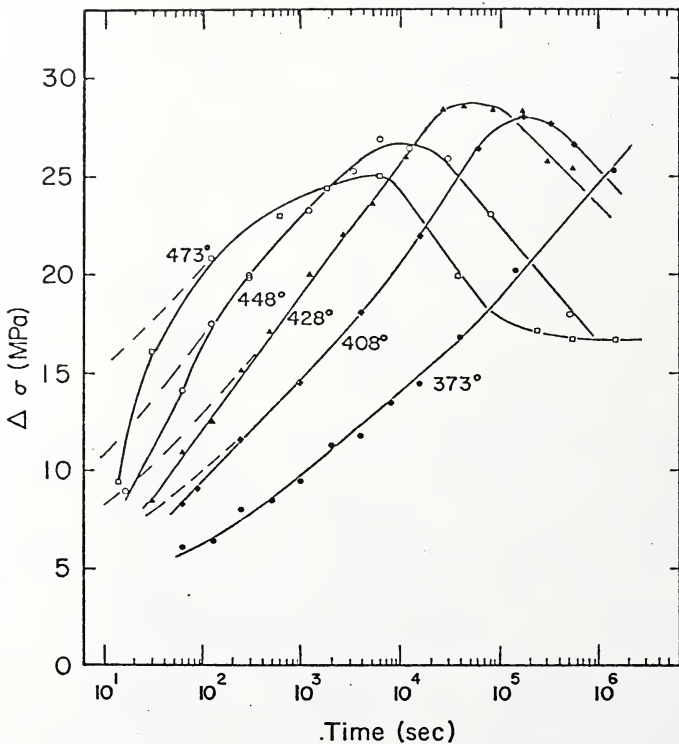


Figure 7. The time and temperature dependence of the return of the lower yield stress in Nickel 200. Specimens were prestrained to a stress level of 265 MPa. The dashed curves are approximate corrected curves which account for specimen heat-up in the aging baths.

TABLE 5

Least Squares Parameters for Static Strain Aging Data
Assuming $\Delta\sigma$ Is a Function of $\ln t$

<u>Temperature</u>	<u>t (sec)</u>	<u>Slope</u> <u>(MPA/\ln sec)</u>	<u>Intercept</u>	<u>r</u>
373	$480 \leq t \leq 1.43 \times 10^6$	2.088	-4.922	0.996
408	$240 \leq t \leq 6.62 \times 10^4$	2.647	-3.356	0.998
428	$60 \leq t \leq 2.16 \times 10^4$	2.602	1.618	0.995
448	$30 \leq t \leq 3.4 \times 10^3$	2.318	6.689	0.998
473	not fitted			

(4) $\Delta\sigma$ decreases significantly after $\Delta\sigma_{\max}$ is passed. Just after the peak, the decrease in $\Delta\sigma$ is almost linear with $\log t$. However, at 473°K, the highest temperature investigated, the data at very long aging times show that the lower yield stress decreases to a constant value of approximately 17 MPa.

Table 5 lists values obtained by the method of least squares for the slopes and intercepts (at $t=1s$) of the aging curves in Figure 7. A $\Delta\sigma$ versus $\ln t$ relationship is assumed to hold for times before $\Delta\sigma$ reaches a maximum.

In addition, Figure 8 shows a set of $\Delta\sigma$ curves which were normalized to their respective maximum peak heights, $\Delta\sigma_{\max}$. An approximate value of 28.5 MPa for $\Delta\sigma_{\max}$ was assumed for the 373°K curve since, for the aging times investigated, a peak was not attained. This diagram has the effect of making the aging curves more nearly parallel.

Figure 9 is a plot of the increase in lower yield stress versus $t^{1/7}$ using data from the 373, 408, 428 and 448°K aging curves of Figure 7. Least squares analysis of $\log \Delta\sigma$ versus $\log t$ curves indicated that $\Delta\sigma$ varies approximately as the 0.14 and 0.15 power of time. See Table 6 for the complete results. This represents an approximate time dependence of $t^{1/7}$.

It is important to note that this author prepared a specimen which had been aged for approximately 6 hours at 525°K (specimen taken from the undeformed threaded end of a deformed tensile specimen) and observed it carefully in a transmission electron microscope. No evidence of precipitates or free graphite in the grains, at dislocations or at grain boundaries was observed. Thus, it is highly unlikely that precipitation of carbon occurs during aging between 373 and 473°K in Nickel 200.

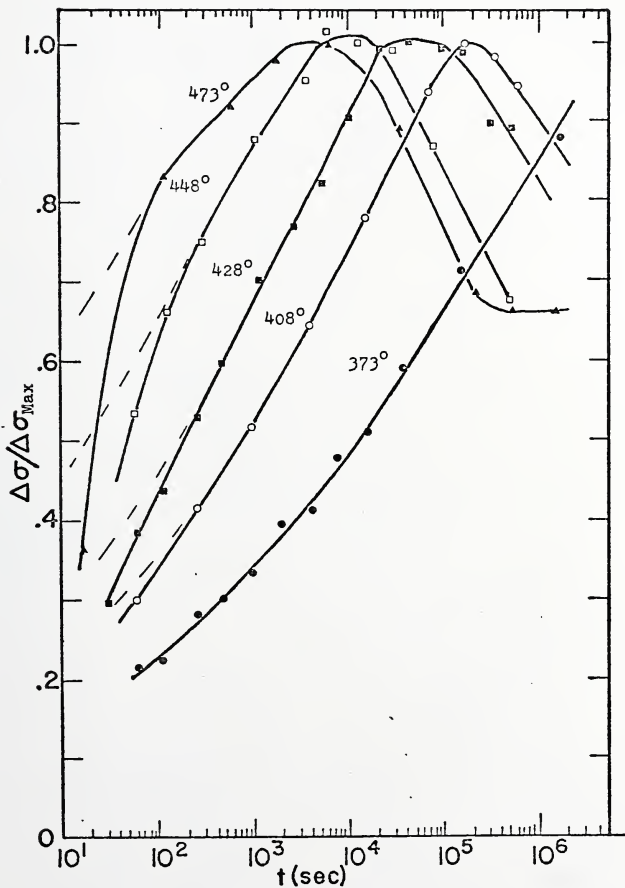


Figure 8. Normalized aging curves for Nickel 200. The 373°K curve was normalized to an assumed maximum of 28.5 MPa. The dashed curves reflect approximate corrections for the heat-up time of the specimens.

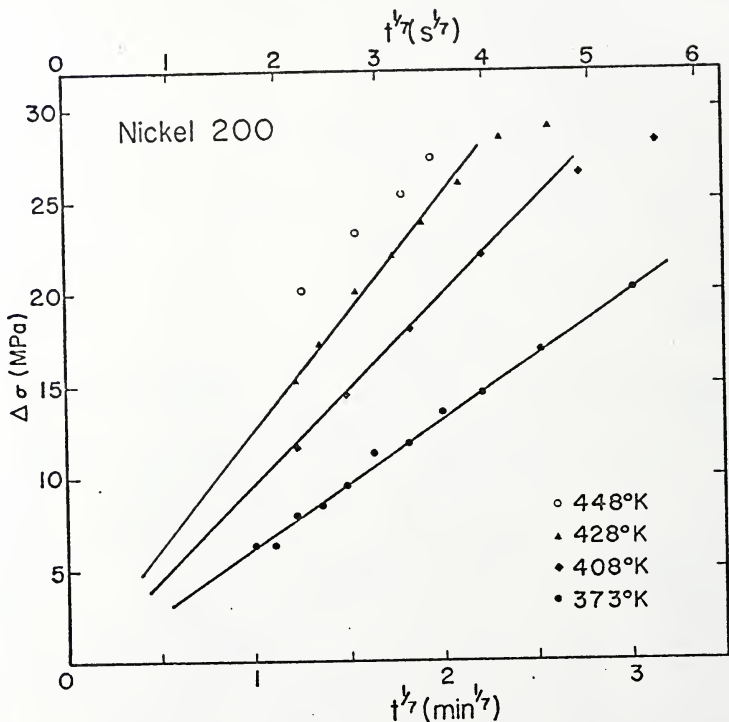


Figure 9. Illustrating the approximate $t^{1/7}$ power law relation governing the aging of Nickel 200 at temperatures below 448°K. Data for the 448°K (shown) and 473°K cases do not fit this relation well.

TABLE 6

Least Squares Parameters for Static Strain Aging Data
Assuming a Log $\Delta\sigma$ -Log t Linear Relationship

<u>Temperature</u>	<u>t (min)</u>	<u>Slope</u>	<u>Intercept</u>	<u>r</u>
373	$1.0 \leq t \leq 23,752$	0.145	0.804	0.993
408	$1 < t < 2892$	0.146	0.984	0.999
428	$2 \leq t \leq 710$	0.137	1.109	0.997
448 ^a	$2 \leq t \leq 100$	0.099	1.232	0.998
473 ^b	$10 \leq t \leq 30$	0.055	1.307	1.000

^a Three points

^b Two points

3.2 The Lüders Extension, ϵ_L

Figure 10 illustrates the dependence of the Lüders extension on $\log t$. The behavior is similar to that exhibited in Figure 7 for curves of $\Delta\sigma$ versus $\log t$. However, note that the peak in the Lüders extension occurs (at a given temperature) at an earlier time than the corresponding peak in $\Delta\sigma$. This may be indicative of the onset of hardening and is consistent with results obtained in bcc metals. Note also that at long times the extensions tend to return to their short time values; that is, they do not remain constant after reaching their maximum values. An interesting point is that the highest temperature curve (473°K) reaches an apparent minimum at approximately 1500 minutes.

3.3 The Hardening Component, $\Delta\sigma_H$

Figure 11 is a plot of $\Delta\sigma_H$, the hardening component of the increase in lower yield stress. This parameter was deduced as noted in Figure 5 by using the equation $\Delta\sigma_H = \sigma_{Ext} - \sigma_0$. Figure 11 shows that this hardening component appears only at discrete times. Note also that $\Delta\sigma_H$ peaks at approximately the same time as $\Delta\sigma$ and decreases to a value higher than that observed at very short aging times. It should be noted that the values of $\Delta\sigma_H$ cannot be taken as exact due to alignment problems which affected the choice of σ_{Ext} (see Figure 5).

3.4 Activation Energies

In order to establish a mechanism for static strain aging, the apparent activation energies associated with particular time dependent aging events were deduced. The activation energy for the return of the lower yield stress where in the interval an approximate logarithm of

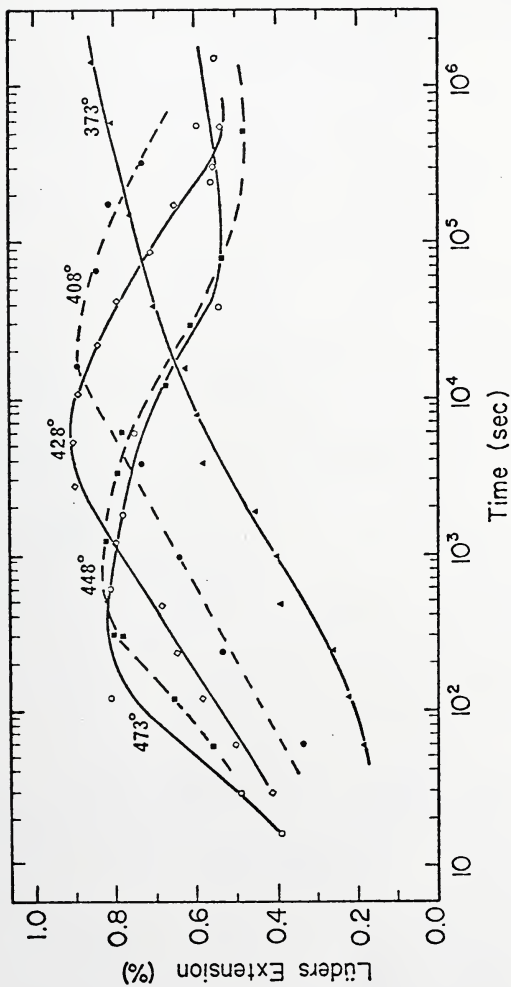


Figure 10. The dependence of the Lüders strain on time and temperature in Nickel 200.

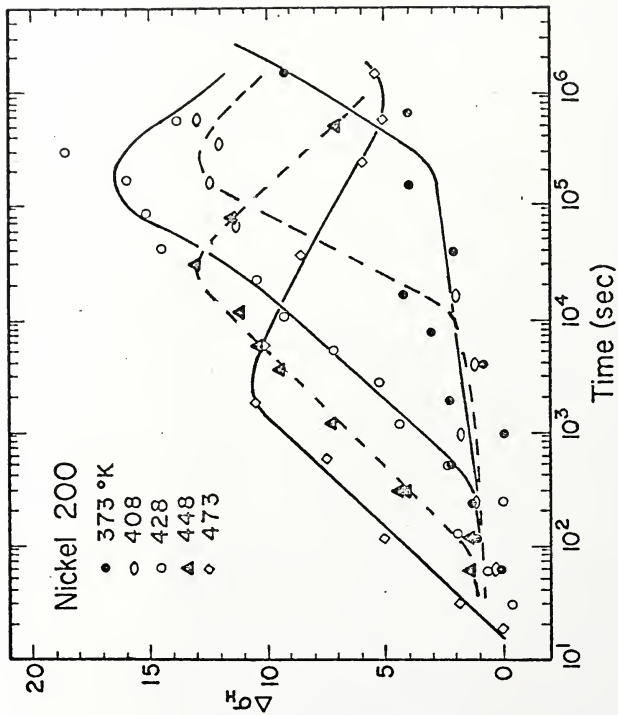


Figure 11. The approximate behavior of the secondary hardening component of the lower yield stress increase ($\Delta\sigma_H = \sigma_{Ext} - \sigma_0$).

time behavior is exhibited was calculated on the basis of the respective times to achieve a stress increase of 15.0 and 20.0 MPa. On this basis the activation energy for the return of the lower yield stress in Nickel 200 is 25.2 ± 3.2 and 26.4 ± 2.7 kcal/mole.

The activation energy for the development of a 0.6% Lüders extension is similar, 24.3 kcal/mole. In addition, the shift of the peaks of $\Delta\sigma$ versus $\log t$ is consistent with an activation energy of approximately 22 kcal/mole. The downward trend of the aging curves behaves in a manner corresponding to an activation energy of 29.0 kcal/mole on the basis of the method of cuts at $\Delta\sigma = 23$ MPa.

3.5 The Dependence of $\Delta\sigma$ and ϵ_L on Prestrain

To more fully characterize static strain aging, a series of specimens were prestrained various amounts and then aged at 448°K for a fixed time of 6000 seconds, the approximate time required to achieve the maximum $\Delta\sigma$ at this temperature when the prestrain was 5% (see Figure 7).

Figure 12 illustrates the dependences of $\Delta\sigma$ and ϵ_L on the amount of deformation at a constant aging time and temperature. The $\Delta\sigma$ curve shows that this parameter increases with prestrain, exhibits a broad maximum and then decreases slowly. It is interesting that Stage III of the work hardening behavior (see Section 3.8), as determined from $\log \theta$ versus $\log \sigma$ plots, begins at approximately 18% true strain at 273°K. Stage III is normally associated with dynamic recovery and in view of the broad peak and subsequent decrease in $\Delta\sigma$, it is possible that $\Delta\sigma$ is reflecting the dynamic recovery.

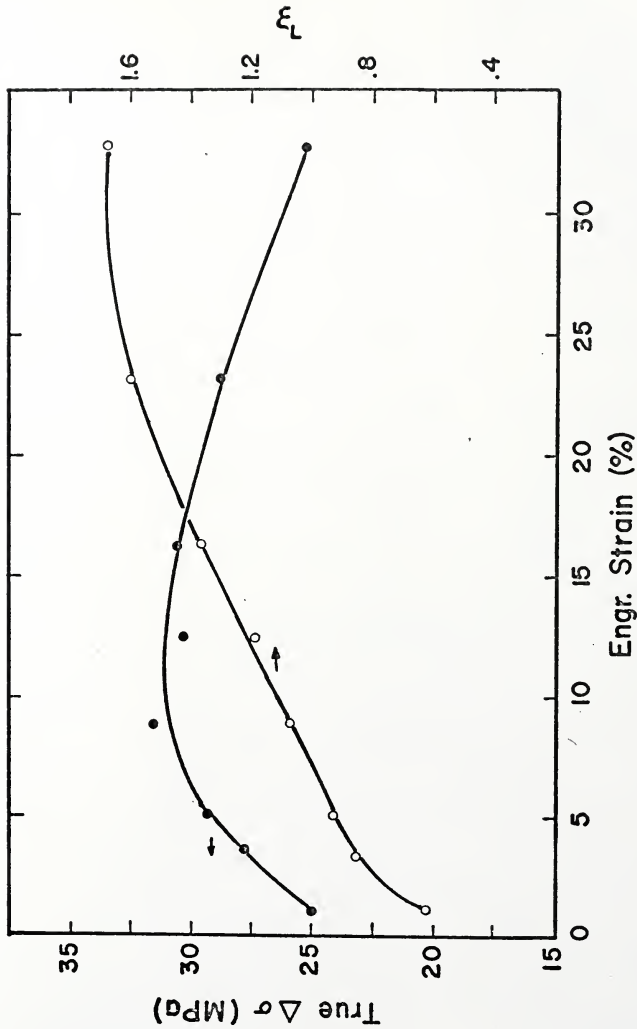


Figure 12. The dependence of $\Delta\sigma$ and ϵ_L on prestrain. Nickel 200 specimens were prestrained at 273°K, aged for 6000 seconds at 448°K, and restrained at 273°K.

The Lüders extension increases continuously with prestrain as indicated in Figure 12. The Lüders strain is determined not only by the size of the lower yield stress but also by the magnitude of the work hardening rate. The latter decreases continuously with strain and tends to make ϵ_L increase with strain. The fact that ϵ_L continues to increase with ϵ in Figure 12 is probably due to this cause. This is similar to the case of Type A Lüders bands which exhibit an increase in Lüders strain during plastic deformation [122].

3.6 Comparison of Nickel 270 and Nickel 200 Static Strain Aging

Several experimental observations indicate that the higher purity Nickel 270 does not contain sufficient carbon to give rise to measurable dynamic strain aging phenomena. Specifically, the Portevin-Le Chatelier effect was not observed in this metal. Also, even at the highest temperatures investigated, yield points or yield plateaus were not observed in annealed material. Thus, Nickel 270 may be nearly representative of pure nickel in terms of its mechanical properties.

To test if static strain aging is weakly exhibited in Nickel 270 a specimen was prestrained 5% at 273°K and aged for 1200 seconds at 473°K. The resulting curve shown in Figure 13a appears to indicate some aging since a short yield plateau is exhibited. However, the lower yield stress increase for this specimen was only 4.76 MPa which is small compared to the 23.00 MPa value for the commercial purity Nickel 200 specimen (Figure 13b) which was achieved in only one-half this aging time. It is also possible that a significant portion of the 4.76 MPa yield effect that has been observed in face-centered cubic metals [17,123]. Thus, one may be reasonably assured that strain aging phenomena in Nickel 270 are generally weak.

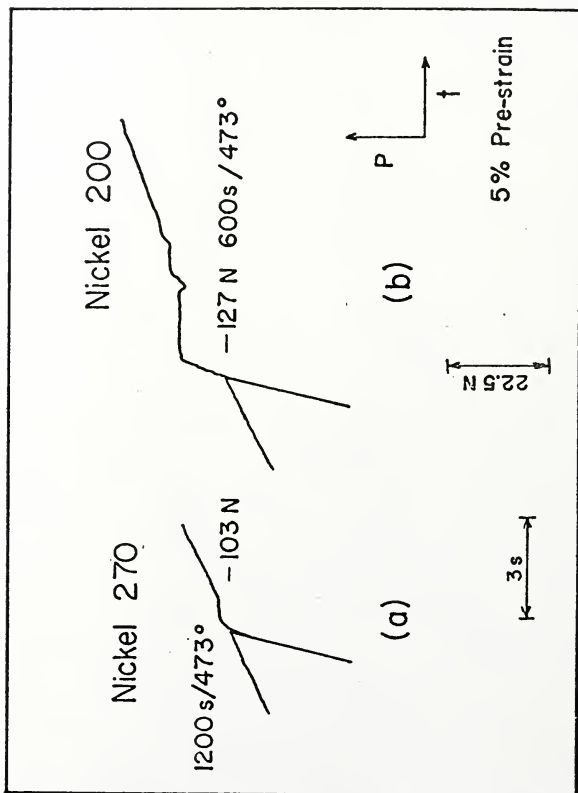


Figure 13. (a) The yield return of a Nickel 270 specimen aged for a time to achieve a maximum in $\Delta\sigma$ for Nickel 200. (b) Yield return for a Nickel 200 specimen aged only one-half as long.

3.7 The Stress-Strain Behaviors

The details of the basic mechanical behavior of the high purity nickel, Nickel 270, are shown in Figures 14-16. Those for commercial purity Nickel 200 are shown in Figures 17-22. Nickel 200 unlike Nickel 270 exhibits serrations and yield points.

As indicated in Figure 21, the Portevin-Le Chatelier effect was observed over four orders of magnitude of strain rate in Nickel 200. The figure also shows the approximate temperature intervals over which Types A, B and C serrated flow were observed. Type C serrations were sudden load drops appearing at regular intervals on the load-time curve. The serrated flow intervals correspond closely to those observed by Nakada and Keh [51] in nickel-carbon alloys indicating that the presence of the manganese in Nickel 200 does not appreciably affect the dynamic aging effects. The data of the present investigation are not extensive enough to calculate the apparent activation energy for the onset of serrations in Nickel 200 with accuracy. However, the data appear to be consistent with the apparent activation energy 15 ± 2 kcal/mole calculated by Nakada and Keh for the somewhat purer alloys [51]. In addition, the apparent activation energy for the disappearance of serrations calculated by Nakada and Keh [51], 26 ± 4 kcal/mole, also appears to be reasonable for Nickel 200.

Figure 14 shows representative stress-strain curves for Nickel 270 obtained at several temperatures. The 0.2% offset flow stress and the ultimate tensile strengths of Nickel 270 are plotted in Figure 15 as functions of the temperature. Note that the ultimate stress decreases monotonically with temperature without any undue irregularity. This type of stress-temperature variation is characteristic of a metal which

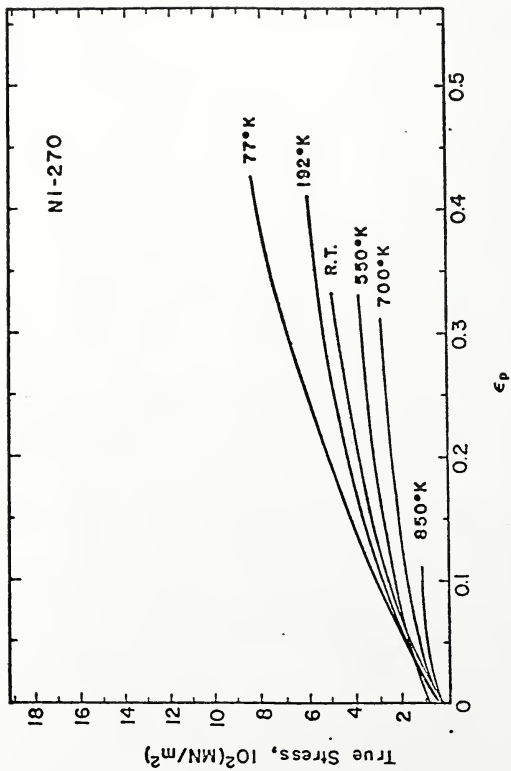


Figure 14. True stress-true plastic strain curves for Nickel 270 ($\dot{\epsilon} = 4.2 \times 10^{-4} \text{ s}^{-1}$).

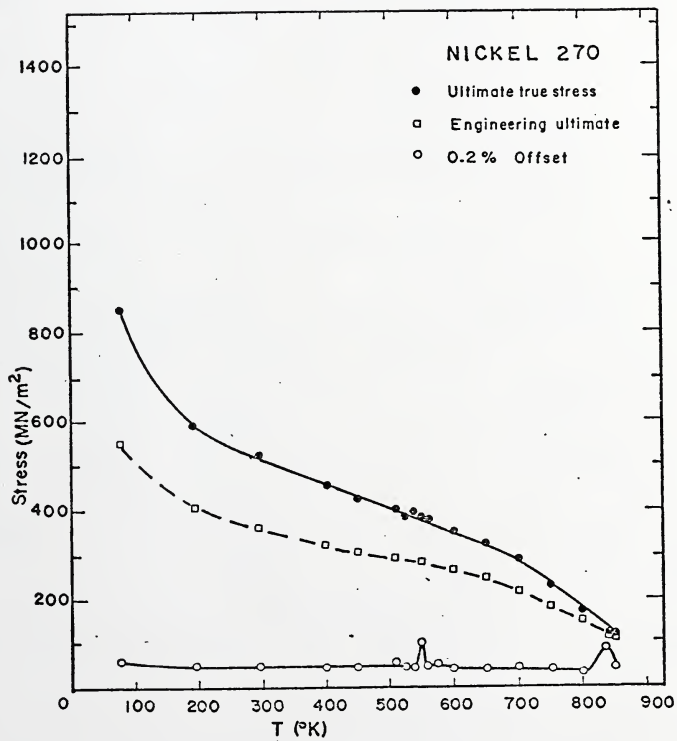


Figure 15. Variation of the 0.2% yield stress and the ultimate tensile strength with temperature in Nickel 270 ($\dot{\epsilon} = 4.2 \times 10^{-4} \text{ s}^{-1}$).

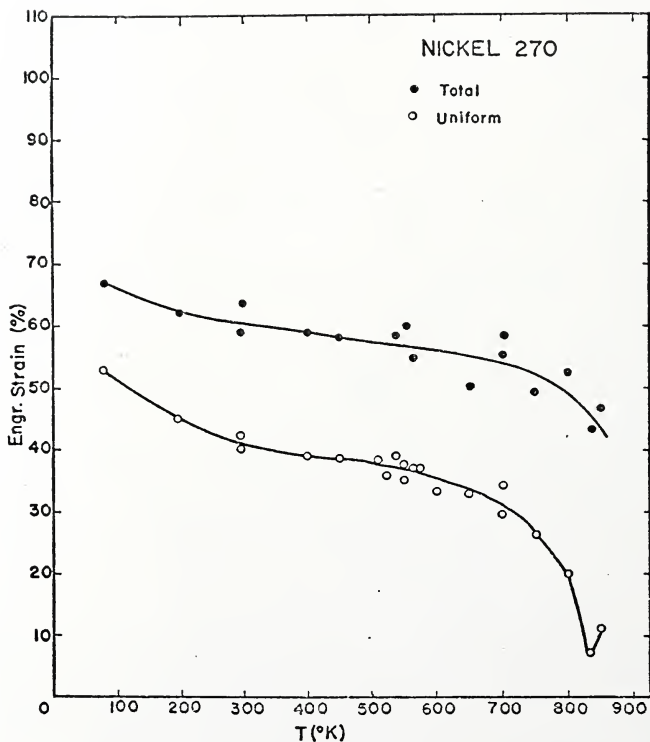


Figure 16. Variation of the uniform and total elongation with temperature in Nickel 270 ($\dot{\epsilon} = 4.2 \times 10^{-4} \text{ s}^{-1}$).

does not exhibit pronounced dynamic strain aging. The total and uniform elongations are illustrated in Figure 16 and show no anomalies. A minimum in ductility was observed at 835°K and surface cracking was noted on the specimens. Cracking also appeared on the specimen tested at 850°K. The Nickel 270 specimens were annealed at 868°K and this temperature was the upper testing limit. The elongations are reasonably constant over a wide range of temperature (approximately 200 to 650°K).

A representative sample of Nickel 200 stress-strain curves are shown in Figure 17. It should be noted that the curves at 300 and 525°K were serrated. Only average stress-strain behavior can be shown in these cases. Note that at 525°K the curve shows an anomalously high ultimate strength. The enhanced strengthening during work hardening is best illustrated in Figure 18 which shows dependence of the 0.2% flow stress and the ultimate stress on the temperature.

Because of the scale of the drawing in Figure 18 the 0.2% offset stress appears to decrease monotonically with temperature. However, a plot of the 0.2% offset stress for Nickel 200 at two strain rates with the stress axis expanded as in Figure 19 shows that there is a small yield stress plateau between approximately 300 and 475°K. This is generally characteristic of dynamic strain aging in bcc and hcp metals. The stresses were not normalized with respect to the elastic modulus, as is customary, because nickel exhibits a large magnetostriction [124,125] and the choice of modulus is uncertain below 626°K, the Curie point [126]. This plateau is weakly exhibited compared to that of titanium [127-129], for example. In comparison to the 0.2% stresses observed in Nickel 270, Nickel 200 exhibits a larger temperature dependence (compare Figures 15 and 18).

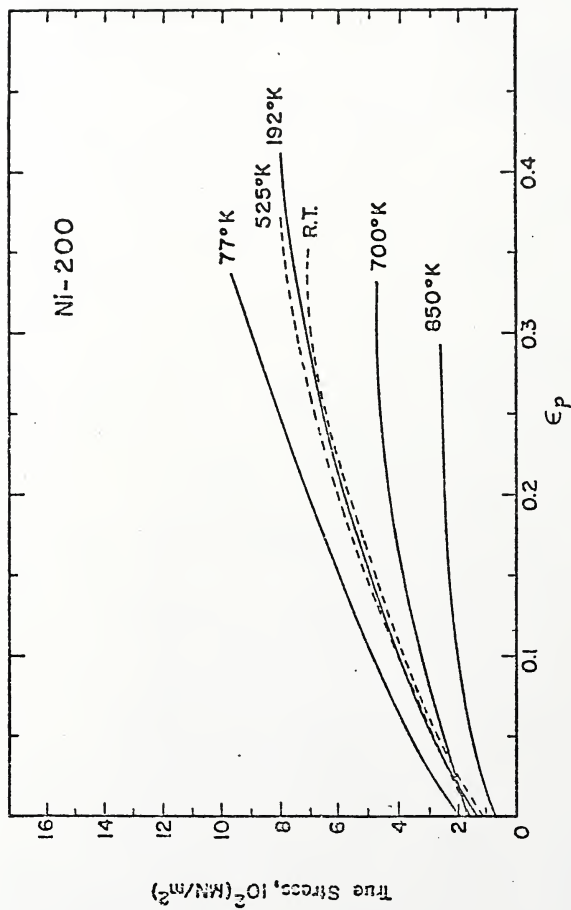


Figure 17. True stress-true plastic strain curves for Nickel 200 ($\dot{\epsilon} = 4.2 \times 10^{-4} \text{ s}^{-1}$).

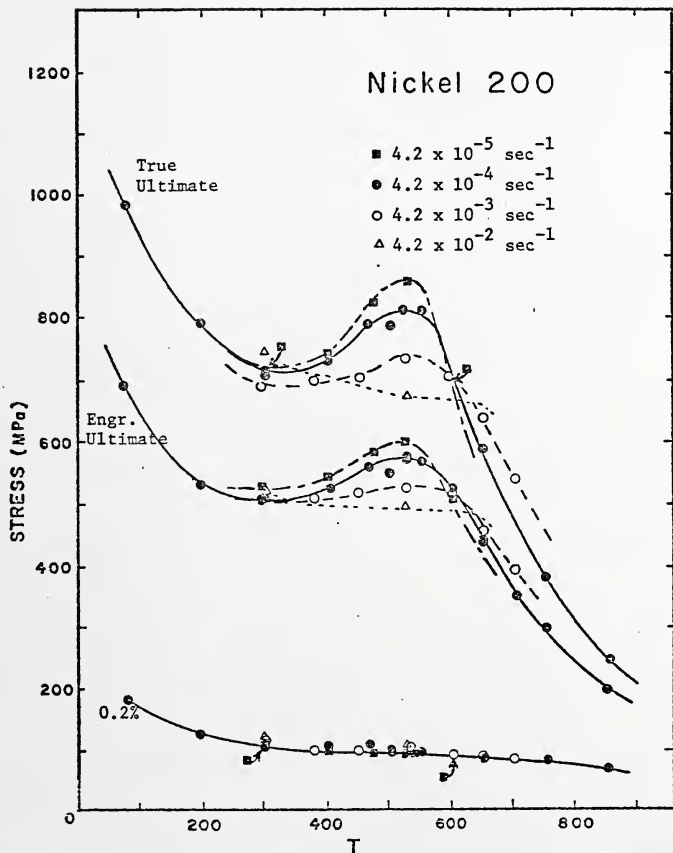


Figure 18. The temperature dependence of the 0.2% yield stress and ultimate tensile strength of Nickel 200.

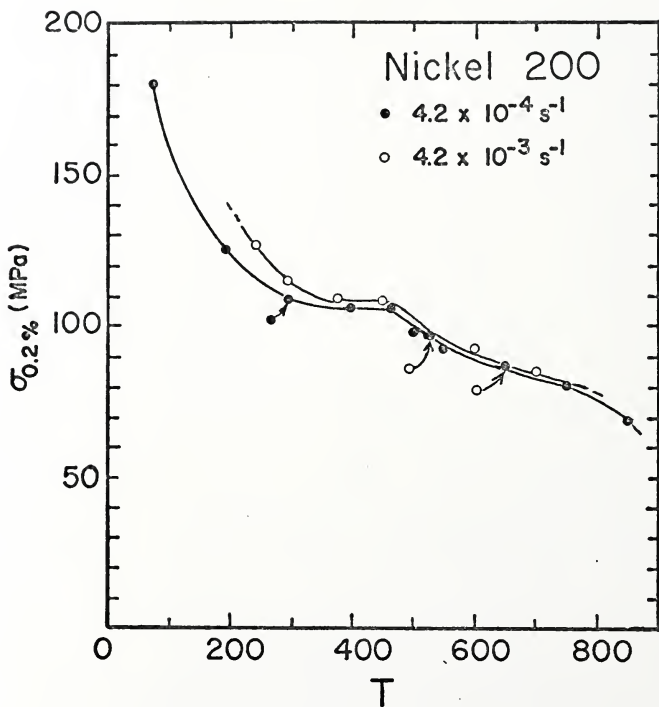


Figure 19. The temperature and strain rate dependence of the 0.2% yield stress in Nickel 200 on an expanded stress axis.

An important feature to note in Figure 18 is that anomalous strengthening is exhibited between 300 and 600°K. In Figure 20 the strain dependence of the flow stress is shown for 5, 11, 19, and 31% plastic strain. This figure demonstrates that only above approximately 11 to 19% plastic strain does the anomalous strengthening become significant. That is, the strengthening effect is not due to anomalous work hardening as Sukhovarov and Kharlova [67] previously suggested. Note that unlike the behavior of the ultimate tensile strengths plotted in Figure 18, the stress levels attained at 31% strain exhibit a rate dependent shift in the peaks. These peaks have a rate dependence corresponding to an activation energy of approximately 38 kcal/mole.

Figure 21 illustrates the temperature dependence of the uniform and total elongations in Nickel 200 at several strain rates. The total elongation at a strain rate of $4.2 \times 10^{-4} \text{ s}^{-1}$ shows a mild ductility minimum (blue-brittle effect) between approximately 300 and 450°K. This minimum is not well-defined. However, a well-defined but small reduction in area minimum does occur in Nickel 200 that is strain rate dependent as shown in Figure 22. This minimum was noted to have shifted in accordance with an apparent activation energy of approximately 25 kcal/mole. A reduction in area minimum is not always manifested in dynamic strain aging [130]. It is interesting to note, however, that 25 kcal/mole is approximately the activation energy for vacancy migration in nickel [109,118]. Not only is the loss in reduction in area not marked, but the lowest value recorded is still above 75%. Adjunct observations of the fracture surfaces under a low-power microscope did not reveal any striking difference in fracture mode at the reduction in area minimum.

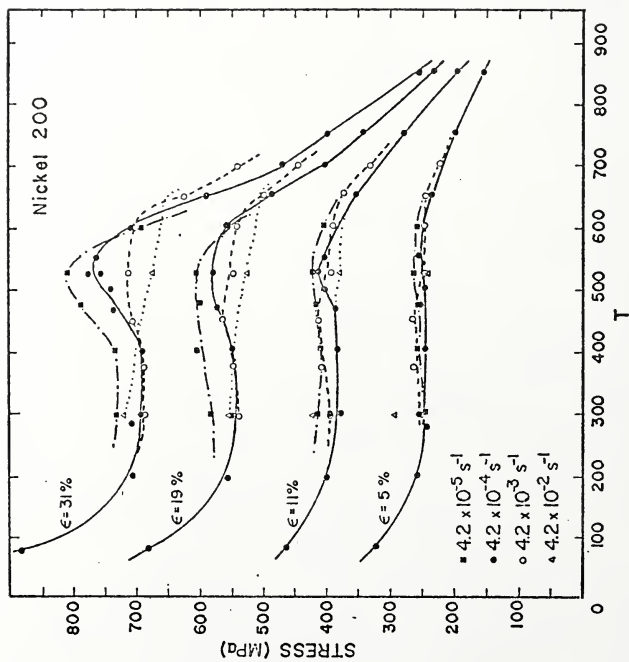


Figure 20. Variation of the stresses at 5, 11, 19, and 30% plastic strain with temperature in Nickel 200.

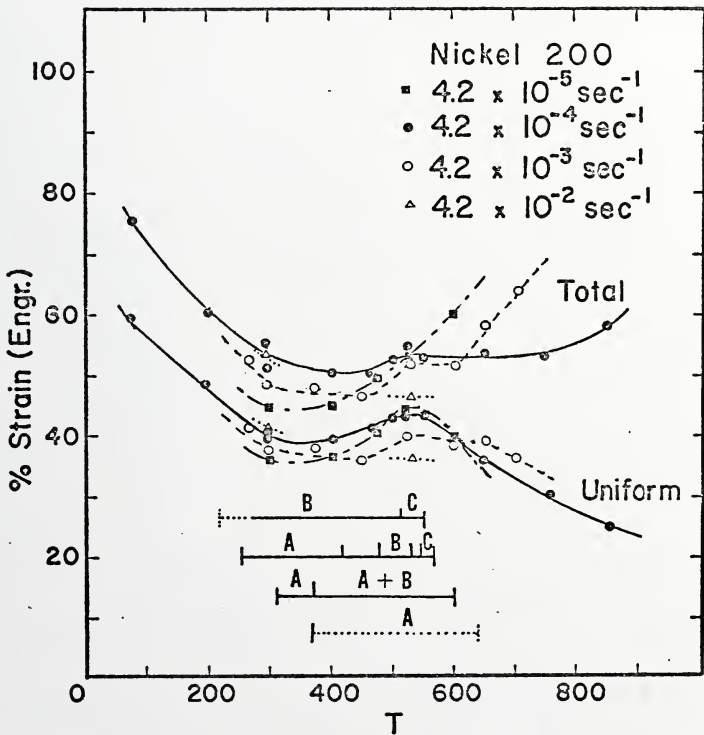


Figure 21. Variation of the uniform and total elongations with temperature in Nickel 200. Also shown are the approximate temperature ranges over which serrations were observed at the respective strain rates.

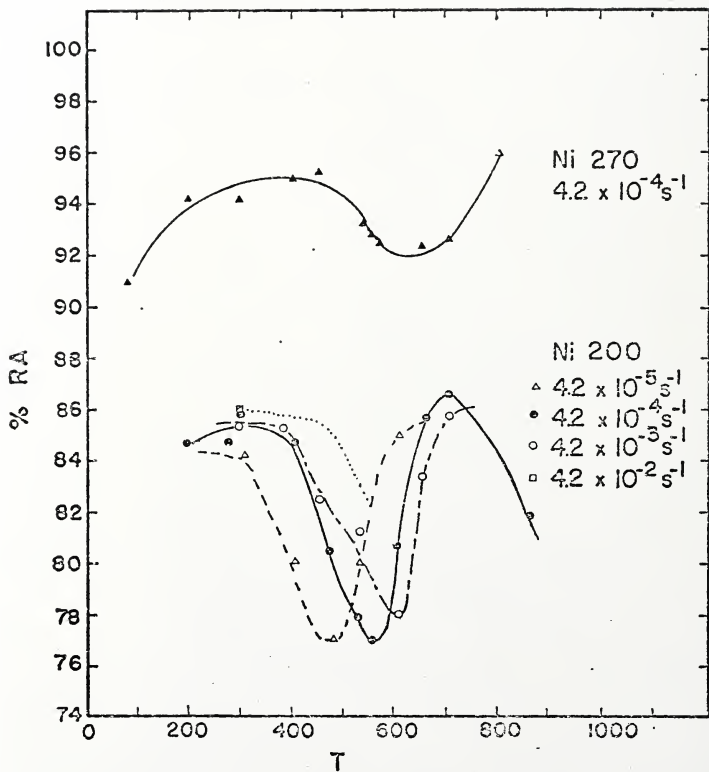


Figure 22. Variation of the reduction in area with temperature for Nickel 200 and Nickel 270.

Note that the higher purity Nickel 270 shows more ductility at all temperatures than does Nickel 200. Although a mild reduction in area minimum does occur in Nickel 270, it is spread over a wide interval between approximately 425 and 750°K and is not as pronounced as that in Nickel 200. Even the lowest reduction in area observed in this investigation is considerably higher than that in most commercially available bcc metals and alloys.

The strain rate sensitivity in Nickel 200 and Nickel 270 was not investigated because the temperature interval of serrated flow in Nickel 200 was some 300°K wide and it was believed that strain rate changes conducted during discontinuous plastic flow would prove inconclusive. It was noted, however, that at room temperature during moderately heterogeneous plastic flow, changes in rate resulted in the appearance of flow stress transients in Nickel 200 and a steady state strain rate sensitivity very close to zero was observed.

In summary, whereas the higher purity Nickel 270 shows no anomalies in ultimate strength and elongation with increasing temperature, Nickel 200 between 300 and 600°K shows anomalous strengthening, serrated flow, a small yield stress plateau and a mild elongation minimum.

3.8 The Work Hardening Behavior of Nickel 270 and of Nickel 200

Figures 23 and 24 show a cross-section of the $\log \theta$ versus $\log \sigma$ curves for Nickel 270 and Nickel 200, respectively, deformed at a nominal strain rate of $4.2 \times 10^{-4} \text{ s}^{-1}$. These curves satisfactorily represent the general trend of work hardening at all strain rates investigated. No attempt has been made to draw in the straight lines representing the stage behavior in order to reduce the complexity of the figures.

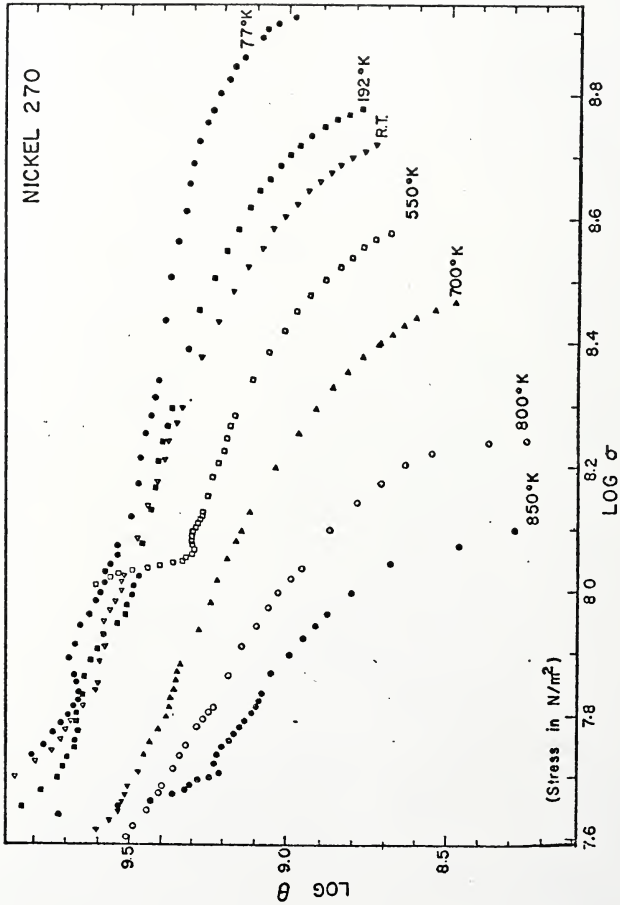


Figure 23. The log σ -log $\dot{\epsilon}$ curves of Nickel 270 ($\dot{\epsilon} = 4.2 \times 10^{-4} \text{ s}^{-1}$).

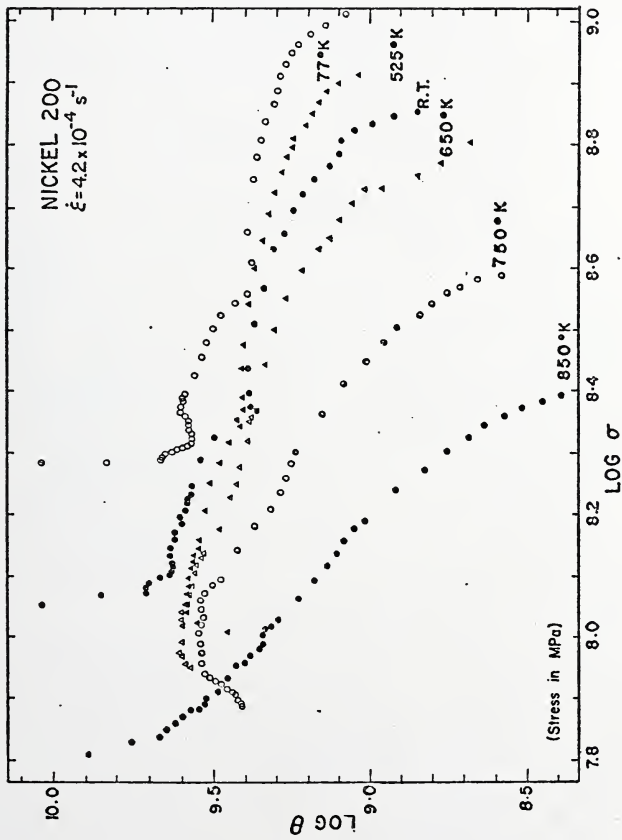


Figure 24. The log t -log σ curves of Nickel 200 ($\dot{\epsilon} = 4.2 \times 10^{-4} \text{ s}^{-1}$).

The work hardening behavior of Nickel 270 and of Nickel 200 are similar to those found earlier in pure face-centered cubic metals. The stages appear in the same manner as Zankl [75], Schwink and Vorbrugg [77], and others [76,78-81] have shown to be the case for pure face-centered cubic metals. It should be noted that hexagonal close packed metals such as zirconium and titanium [131] as well as body-centered cubic metals such as iron and niobium [132] show much higher m values (order of 7 to 40) than the fcc alloys presently being investigated. That is, all $\log \theta$ versus $\log \sigma$ plots for these metals show much steeper slopes. Also, these metals tend to show only one or two stages of deformation behavior indicating that the deformation in these metals is possibly controlled by a different set of deformation phenomena.

Figures 25 and 26 show the m values obtained for Nickel 270 and Nickel 200 by measuring the slopes of $\log \theta$ versus $\log \sigma$ plots at different temperatures. The error of each particular m_{II} value is approximately ± 0.1 as measured by the plausible maximum and minimum slopes that might conceivably characterize a particular work hardening stage. It should also be noted that Stages I and III are difficult to characterize in many cases. The parameter m_{III} is plotted in the figures only to show trends in the third stage as a function of temperature. They are not accurately defined since in Stage III $\log \theta$ - $\log \sigma$ plots are not linear but curved. However, Stage II is generally uniquely defined by a straight line on $\log \theta$ - $\log \sigma$ curves.

Nickel 270 and Nickel 200 possess m_{II} values which are close to 1.5 as shown in Figures 25 and 26. Note that in Nickel 200 m_{II} remains constant over a wide range of temperatures and is strain rate independent.

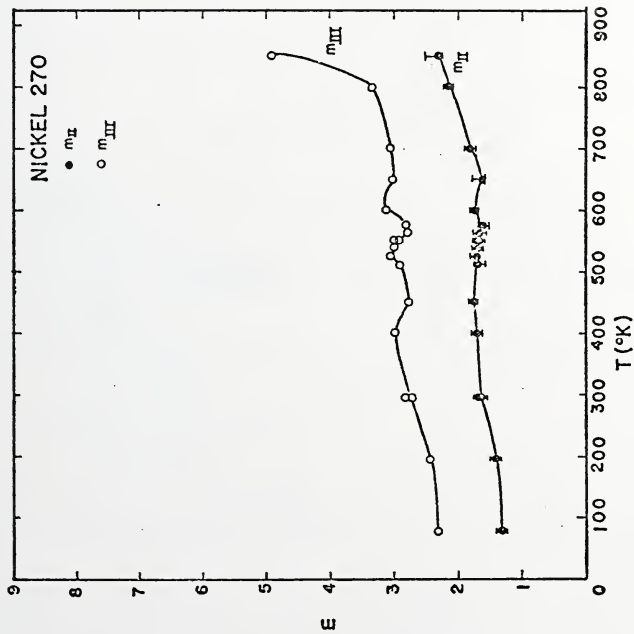


Figure 25. The variation of m_{II} and m_{III} with temperature in Nickel 270 ($\dot{\epsilon} = 4.2 \times 10^{-4} \text{ s}^{-1}$).

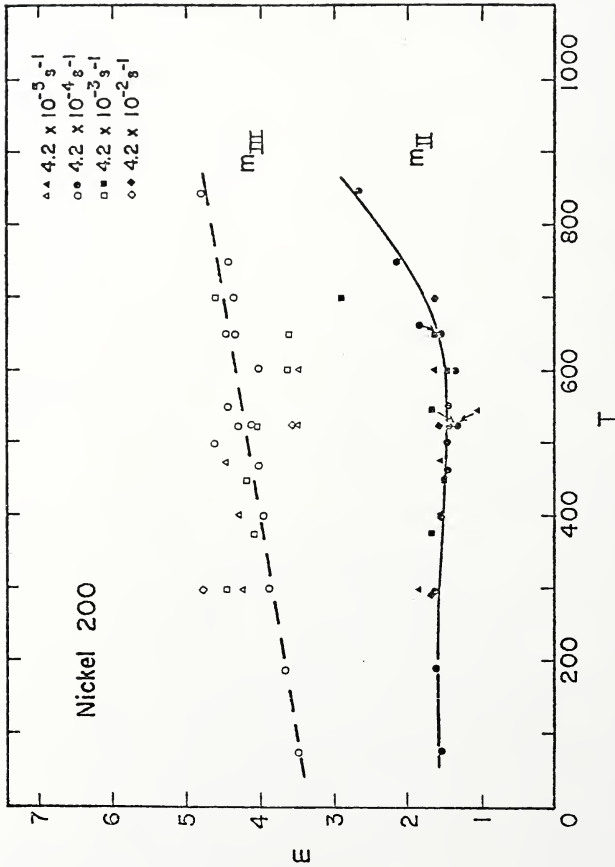


Figure 26. The variation of m_{II} and m_{III} with temperature in Nickel 200 ($\dot{\epsilon} = 4.2 \times 10^{-4} \text{ s}^{-1}$).

It is important to emphasize that the apparent work hardening peak observed in Nickel 200 (Figures 18 and 20) is not a true work hardening peak in the sense that Nickel 200 stress-strain curves show anomalous increases in work hardening over a uniquely defined temperature interval. The peak is associated with an increase in the uniform elongation around the temperature of the ultimate stress peak. Figure 27, a plot of $(\sigma_{5\%} - \sigma_{0.5\%})$ versus temperature, readily shows this behavior. This parameter (where $\sigma_{5\%}$ and $\sigma_{0.5\%}$ are the true stresses at 5 and 0.5% true plastic strain, respectively) confirms that there is little temperature dependence of the work hardening. The constancy of m_{II} in Figure 26 also substantiates this observation. Figures 28 and 29 show very clearly that the onset of Stage III is delayed over exactly the same temperature interval as develops the peak in ultimate stress. These facts imply that there is no prominent work hardening peak in nickel as earlier authors have indicated [67]. There is, however, a significant delay in the onset of Stage III or of dynamic recovery.

In Stage III deformation in both a polycrystalline or single crystal fcc metal or alloy, the stress-strain curve shows a high curvature, i.e., work hardening decreases very rapidly with continued deformation. Thus, Stage III m values tend to be high. Figures 25 and 26 show that m_{III} increases with increasing temperature. This is consistent with the concept that dynamic recovery becomes more important with increasing temperature.

Now consider the extent or length of Stage II which is not illustrated well in the $\log \theta$ - $\log \sigma$ diagrams. In purer metals such as Nickel 270 it is observed that Stage II, which is governed primarily by slip on single slip systems within each grain [75], is lengthened by

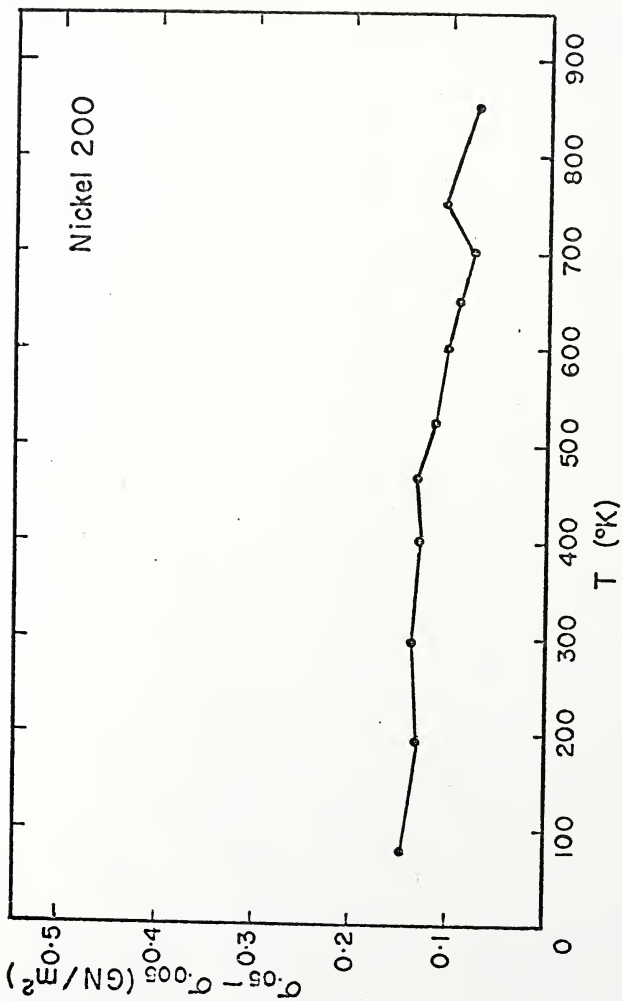


Figure 27. The variation of the work hardening parameter ($\sigma_{5\%} - \sigma_{0.5\%}$) with temperature ($\dot{\epsilon} = 4.2 \times 10^{-4} \text{ s}^{-1}$).

the presence of interstitial carbon as in Nickel 200. Figure 28 compares the approximate strain at which Stage II deformation begins, ϵ_2 , and that at which Stage III begins (and Stage II ends), ϵ_3 , for Nickel 200 and Nickel 270. The principal effect of interstitial carbon in the DSA interval in this respect is to postpone Stage III dynamic recovery processes to a later time in the deformation history. Also the general level of the Nickel 200 curve is higher than that for Nickel 270. It is not clear at this time how the carbon accounts for the general delay in Stage III.

Nickel 200 exhibits an ϵ_3 maximum over the dynamic strain aging interval. This maximum is closely related to the maximum exhibited in the uniform elongation (Figure 21) and accounts for the strengthening observed over this temperature interval. This maximum in ϵ_3 is strain rate dependent as shown in Figure 29. Not only do the peaks shift to higher temperatures with increasing strain rate but the peak heights decrease as well. This is similar to the behavior of the flow stresses described in Figures 19 and 21. The shift in peaks follows an approximate activation energy of 37 kcal/mole, similar to that obtained for the flow stress peaks.

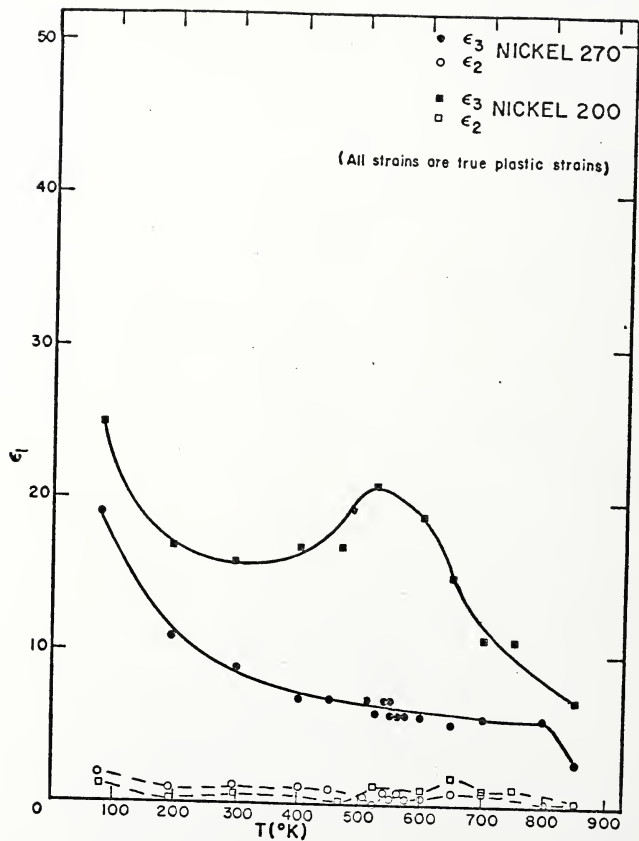


Figure 28. The variation of ϵ_2 and ϵ_3 (the approximate strains at which Stages II and III, respectively, begin) with temperature for Nickel 270 and Nickel 200 deformed at a strain rate of $4.2 \times 10^{-4} \text{ s}^{-1}$.

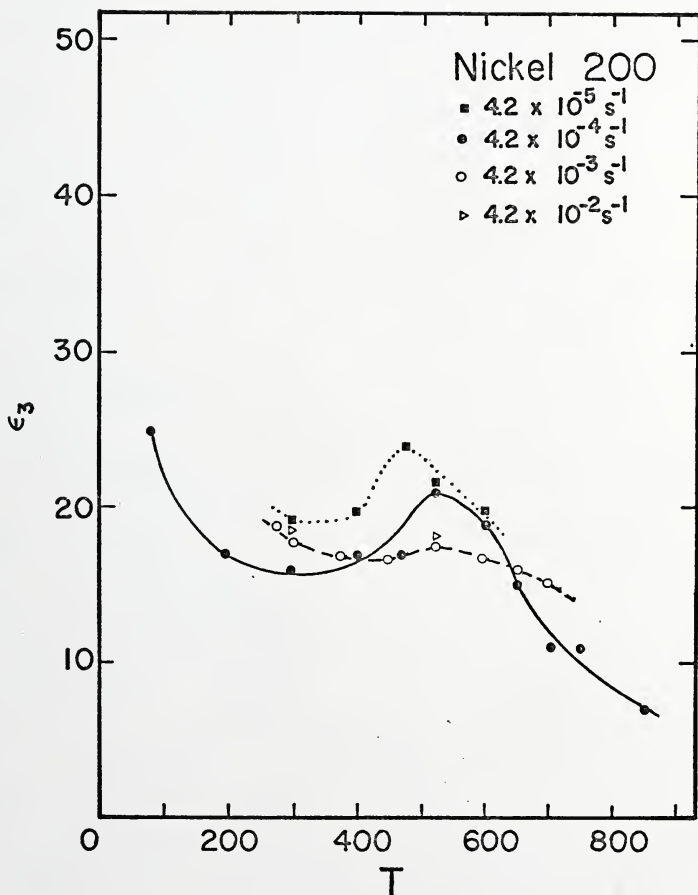


Figure 29. The dependence of ϵ_3 on temperature and strain rate in Nickel 200.

CHAPTER IV
DISCUSSION

4.1 Rationale for Static Strain Aging in Nickel 200

The static strain aging data for Nickel 200 aged between 373 and 473°K after a 5% prestrain indicate:

1. The activation energy for the return of the lower yield stress for times before the maximum in $\Delta\sigma$ is approximately 25 ± 3 kcal/mole.
2. The kinetics of the rise in the lower yield stress can be described by a $\ln t$ time law.

According to the previous discussion three principal causes for strain aging in other metals have been identified: (a) Cottrell pinning, (b) Suzuki locking and (c) Snoek pinning.

It would appear on the outset that aging in Nickel 200 is such that Cottrell pinning must be ruled out as a candidate mechanism. First, the kinetics for aging as described by Cottrell and Bilby [9] are $t^{2/3}$. In Nickel 200 the rise in $\Delta\sigma$ with time is much slower, approximately $t^{1/7}$; this is very different from the Cottrell-Bilby time law. Secondly, the activation energy deduced to govern the early stages of pinning in Nickel 200 is not consistent with the migration energy of carbon, the principal impurity in Nickel 200, as the Cottrell-Bilby model would suggest. The migration energy of carbon in nickel is approximately 35 kcal/mole (see Table 2) and thus significantly different from the observed activation energy. Accordingly, the random migration distance

for carbon at all temperatures investigated during the time required to cause maximum strengthening is only about $8b$ which is a very short diffusion distance compared to distances involved in the formation of a Cottrell atmosphere.

Suzuki pinning is not believed to be responsible for the observed strain aging behavior in Nickel 200 primarily because the stacking fault energy of pure nickel is very high. Hence, the probability of forming stable faults in nickel is very low. It is believed that carbon impurities do not lower the stacking fault energy enough to have a significant effect with regard to this mechanism.

Snoek pinning by itself cannot account for the rise in $\Delta\sigma$ unless anisotropic defects exist in the material in sufficient numbers and have a sufficiently high interaction energy with dislocations. As will be demonstrated the carbon-vacancy pair can satisfy these requirements. However, Snoek pinning should occur in times, very short at the temperatures investigated, compared to the times observed for the rise in $\Delta\sigma$.

The formation of ordered carbon-vacancy pair atmospheres near dislocations can account for the observed static strain aging behavior. The very long times required to reach the maximum in $\Delta\sigma$ can be rationalized in terms of a stress assisted migration of vacancies toward dislocations where enhanced trapping by carbon occurs. The result is an accumulation of ordered carbon-vacancy pairs near the dislocation and the concomitant growth of an ordered carbon-vacancy pair atmosphere. In short, the proposed model utilizes aspects of both the Cottrell-Bilby and the Schoeck-Seeger theories of static strain aging.

In summary the following stages are envisioned: (a) At the end of deformation vacancies diffuse to and become trapped in large measure

by adjacent carbon atoms. (b) The carbon-vacancy pairs thus formed undergo Snoek ordering within the stress fields of the dislocations. (c) Then a slow migration of vacancies toward the dislocation develops an atmosphere of carbon-vacancy pairs near the dislocation. (d) Eventually the vacancy concentration decreases because of losses to sinks. This reduces the pair concentration and causes an eventual loss of strengthening. These stages will now be considered in detail.

4.2 The Mechanism of Static Strain Aging Exhibited in Nickel 200

4.2.1 The Distribution of Vacancies, Carbon Atoms and Dislocations After Plastic Deformation

After the prestrain of 5%, the vacancy concentration in nickel is approximately 10^{-5} atomic fraction as given by Eq. 9. The particular heat of Nickel 200 used in this investigation contains approximately 0.1 w/o or 0.5 a/o carbon. Thus, at 5% strain the carbon to vacancy ratio is approximately 500 to 1. If the carbon and the vacancies are distributed at random throughout the nickel lattice, then the mean carbon atom spacing will be approximately $6b$; the mean vacancy spacing will be approximately $50b$.

After plastic deformation to 5% strain, the dislocation density [133,134] is estimated to be between 3 and $8 \times 10^9 \text{ cm}^{-2}$. Assuming an equidistant array of straight dislocation lines as a first approximation to the dislocation configuration, then their mean spacing is approximately 450 to $730b$.

4.2.2 Vacancy Trapping by Carbon Atoms

In the absence of other defects such as grain boundaries or dislocations, vacancies in a metal are attracted to oversized impurity

atoms by a hydrostatic pressure gradient. The strain energy released when a vacancy is moved from an infinite distance away from an impurity to the impurity is known as the binding energy of the vacancy-impurity pair. This phenomenon is commonly called trapping and it is generally accepted that impurity atoms can trap vacancies in metals. For example, it has been shown that the presence of carbon in austenitic stainless steel forestalls radiation induced swelling in certain critical nuclear reactor parts. This indicates that void formation is hindered by the presence of carbon due to trapping of vacancies [135]. Trapping of carbon by vacancies in irradiated mild steel has been demonstrated as well [136].

4.2.3 The Concentration of Carbon-Vacancy Pairs

After deformation in Nickel 200 and before aging of a specimen, it is reasonable to assume that vacancies become trapped by carbon atoms initially. This probably occurs very rapidly even at 373°K, the lowest aging temperature used, since the vacancies do not have to travel far to become trapped by carbon atoms. Vacancies in nickel are very mobile as evidenced by their approximate 0.8 to 0.9 eV migration energy and assuming that an equilibrium is established between the carbon-vacancy pairs and free vacancies, their concentrations may be calculated on the basis that the binding energy of the carbon-vacancy pair can be estimated to be 0.2 to 0.3 eV per pair from diffusion data (Section 1.4). For the moment, it is assumed that the dislocations in the metal do not affect the concentrations. The concentrations of single (free) vacancies (c_v^f) and bound vacancies in carbon-vacancy pairs (c_{cv}) vary with carbon concentration (c_c), temperature T , and carbon-vacancy binding energy (B)

according to the equations [116]

$$c_{cV} = Z c_c^f c_v^f e^{B/kT} \quad (11)$$

and

$$c_v = c_v^f + c_{cV} \quad (12)$$

where c_v is the vacancy concentration generated during plastic deformation, c_c^f is the free carbon concentration and Z is 6, the nearest neighbor coordination number for a carbon atom in an octahedral site of the fcc lattice.

Substituting Eq. 12 into Eq. 11 gives

$$c_{cV} = Z(c_c - c_{cV})(c_v - c_{cV})e^{B/kT} \quad (13)$$

For $c_c = 5 \times 10^{-3}$ and $c_v = 10^{-5}$ one may write on the basis that $c_c \gg c_v$,

$$c_{cV} = Zc_c(c_v - c_{cV})e^{B/kT} \quad (14)$$

Substituting a value for B equal to 0.3 eV and a temperature of 408°K into Eq. 14 gives the carbon-vacancy pair concentration of 9.93×10^{-6} , very close to the total vacancy concentration of 10^{-5} . The free vacancy concentration from Eq. 12 is then 6.92×10^{-8} atom fraction. Thus, almost all (99.3%) vacancies are bound to carbon atoms based upon the choice of B .

In the absence of carbon atoms the concentration of vacancies at thermal equilibrium is given by

$$c_v = e^{-Q_f/RT} \quad (15)$$

where Q_f is the vacancy formation energy. At 408°K and a Q_f of approximately 39 kcal/mole (1.7 eV) [118] the vacancy concentration is approximately 1.8×10^{-21} atom fraction. This is many orders of magnitude smaller than the free vacancy concentration calculated above and suggests that the deformed metal is not in its lowest energy state with regard to numbers of vacancies. Thus, there exists a distinct tendency for vacancies to migrate to sinks. Because of the high binding to carbon atoms, vacancies spend a large portion of their migration time bound to carbon atoms and, hence, the process of annealing to dislocations and grain boundaries is sluggish and takes a considerable time.

Consider next the influence of a dislocation on the carbon-vacancy pair concentration. It has been demonstrated that the carbon-vacancy pair may be visualized as an elastic dipole which can reorient in the strain field of a dislocation. In Eqs. 11-14, the binding energy, B , is completely general. That is, in the specific case which includes Snoek ordering, B becomes position dependent. Specifically,

$$B = B' + u(r) \quad (16)$$

where B' is the binding energy of a carbon-vacancy pair and $u(r)$ is the position dependent interaction energy of a carbon-vacancy pair with a dislocation. Thus, the effect of $u(r)$, which varies as r^{-1} , is to enhance the binding of vacancies to carbon atoms near the dislocation. This will be explained in detail presently.

4.2.4 Theory of Schoeck Locking by Carbon-Vacancy Pairs

In the case of nickel-carbon alloy, the carbon-vacancy pair acts as a dipole (Section 1.4). Appendix A presents a calculation of the

approximate interaction energy between an assumed carbon-vacancy dipole and a screw dislocation in a fcc lattice. The interaction calculation related to an edge dislocation is more complicated [137]. However, as indicated first by Nabarro [138] and later expanded upon by Cochardt *et al.* [137], the strength of interaction between a dislocation and impurity atoms may be assumed to be very similar whether the dislocation is in the screw or edge orientation.

Let us consider the case of locking of a screw dislocation by an ordered atmosphere of dipoles in the fcc lattice. The reasoning is analogous to that for the calculation made by Schoeck and Seeger [28] for carbon (or nitrogen) in alpha iron. However, the interaction energy for a dipole in a fcc lattice as shown in Figure 35 in Appendix A is somewhat different. The carbon atoms in nickel are assumed to occupy octahedral interstitial sites, e.g., the body-centered position of the fcc unit cell. The six nearest neighbors are face-centered atoms. A dipole is formed when a vacancy is situated on a face-centered position as schematically shown in Figure 30. Thus, the carbon-vacancy dipole may be oriented in one of three possible 100 type directions. These positions are denoted by an orientation number 1, 2 or 3. The dislocation line is assumed to lie along one of four 101 type directions.

It is shown in Appendix A that for the specific case of a screw dislocation, each of the three possible orientations of the carbon-vacancy dipole interacts differently with the dislocation. This gives rise to three possible interaction energies and one of the three orientations is most stable. That is, a carbon-vacancy dipole in, say, the 1-orientation can flip to another orientation (say, 2) and the result is that the interaction energy between that particular dipole

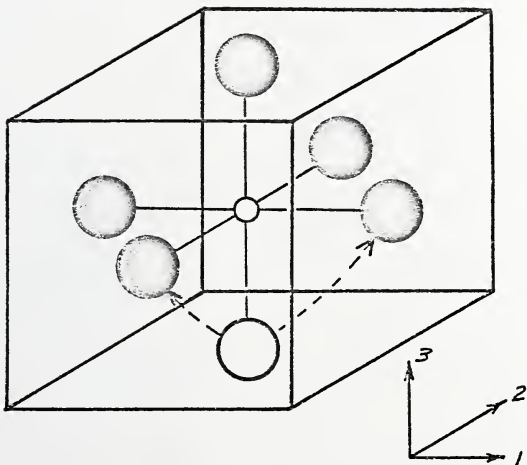


Figure 30. A schematic illustration of the assumed configuration of the carbon-vacancy pair and the three possible independent orientations that it may assume.

and the dislocation is lower after one jump of a vacancy. Thus, the strain energy is lower by $u_1 - u_2$ where u_1 is the interaction energy of a type 1 dipole with the dislocation and u_2 is that associated with the type 2 dipole. This is the energy associated with the stress induced ordering of a dipole in the dislocation strain field. The three possible dipole orientations for an assumed dislocation are shown in Table 8 of Appendix B and possess the following interaction energies:

$$u_1 = -\frac{A}{r} (\sin \theta + \sqrt{2} \cos \theta) = u \quad (17a)$$

$$u_2 = 0 \quad (17b)$$

$$u_3 = -u \quad (17c)$$

where A is an interaction constant assumed approximately equal to 0.2 eV-b (7.97×10^{-21} dyne - cm²).

The concentration of dipoles in each of the three orientations can be calculated easily. Let c_{cv} be the total carbon-vacancy pair concentration expressed as an atom fraction. The concentrations of pairs in the three possible orientations are designated $(c_{cv})_1$, $(c_{cv})_2$ and $(c_{cv})_3$. The total concentration of carbon-vacancy pairs after initial ordering at the beginning of the strain aging process is

$$c_{cv} = (c_{cv})_1 + (c_{cv})_2 + (c_{cv})_3 \quad (18)$$

where

$$(c_{cv})_1 = 2c_c^f c_v^f \exp\left(\frac{B' + u}{kT}\right) \quad (19a)$$

$$(c_{cv})_2 = 2c_c^f c_v^f \exp\left(\frac{B'}{kT}\right) \quad (19b)$$

$$(c_{cv})_3 = 2c_c^f c_v^f \exp\left(\frac{B' - u}{kT}\right) \quad (19c)$$

and c_C^f and c_V^f are the initial free carbon and free vacancy concentrations, calculated from Eqs. 11 and 12. Recall that u depends upon position.

In order to simplify the solution of the equations and to demonstrate the principles involved, assume that $u = A/r$ and is independent of θ .

The more general case where u is given by Eq. 17 will then be treated.

Combining Eqs. 18 and 19, one obtains

$$c_{CV} = 2c_C^f c_V^f e^{B'/kT} (e^{A/rRt} + e^{-A/rRT} + 1) \quad (20)$$

Note that for large r

$$c_{CV} \approx 6c_C^f c_V^f e^{B'/kT} \quad (21)$$

and

$$(c_{CV})_1 = (c_{CV})_2 = (c_{CV})_3 = c_{CV}/3 \quad (22)$$

Another way of writing the concentration of carbon-vacancy pairs

is

$$(c_{CV})_i = c_{CV} \frac{e^{-u_i/kT}}{\sum e^{-u_i/kT}} \quad (i=1,2,3) \quad (23)$$

or

$$n_i = n_0 \frac{e^{-u_i/kT}}{\sum e^{-u_i/kT}} \quad (24)$$

where n_i and u_i are the number per unit volume and the interaction energy, respectively, of dipoles in the i^{th} orientation and n_0 is the initial number of dipoles per unit volume.

Thus, the population of the three possible orientations approaches equality at large distances from the dislocation and Eq. 21 becomes identical to Eq. 11. The principal consequence of the Snoek energy

is to increase the equilibrium concentration of carbon-vacancy pairs in one orientation, near a dislocation, at the expense of the other two. Figure 31 illustrates the results of a calculation using Eqs. 18 and 19 and shows that 1-type orientations are favored near the dislocation. Note also that c_{CV} , the total carbon-vacancy pair concentration (equilibrium), remains almost constant with distance from the dislocation. At distances greater than $200b$ the concentrations of type 1, 2 and 3 dipoles are almost equal, in agreement with Eq. 21.

It should be kept in mind that up to this point no long range redistribution of vacancies has been assumed to have occurred. What is illustrated is the situation shortly after plastic deformation has ceased and vacancies have migrated short distances of the order of 4 or 5b to form carbon-vacancy pairs which then reorient.

The result of the stress induced ordering of dipoles shown in Figure 31 is to lower the strain energy of the dislocation thereby causing pinning. The Schoeck-Seeger [28] model can be utilized to calculate the initial strength of pinning as measured by $\Delta\sigma$ due to the ordering of carbon-vacancy pairs. The number of carbon-vacancy pairs dn_{CV} between r and $r + dr$ (assuming circular symmetry about the dislocation) is given by

$$dn_{CV} = \frac{2\pi bc_{CV}}{\Omega} r dr \quad (25)$$

where Ω is the atomic volume of solvent (nickel atoms). The width of one atom plane is $1b$; $\Omega = a^3/4$ for fcc metals where a is the lattice constant (3.5238 \AA for nickel [115] and $b = a/\sqrt{2}$). The reduction in energy produced by the ordering of carbon-vacancy pairs is

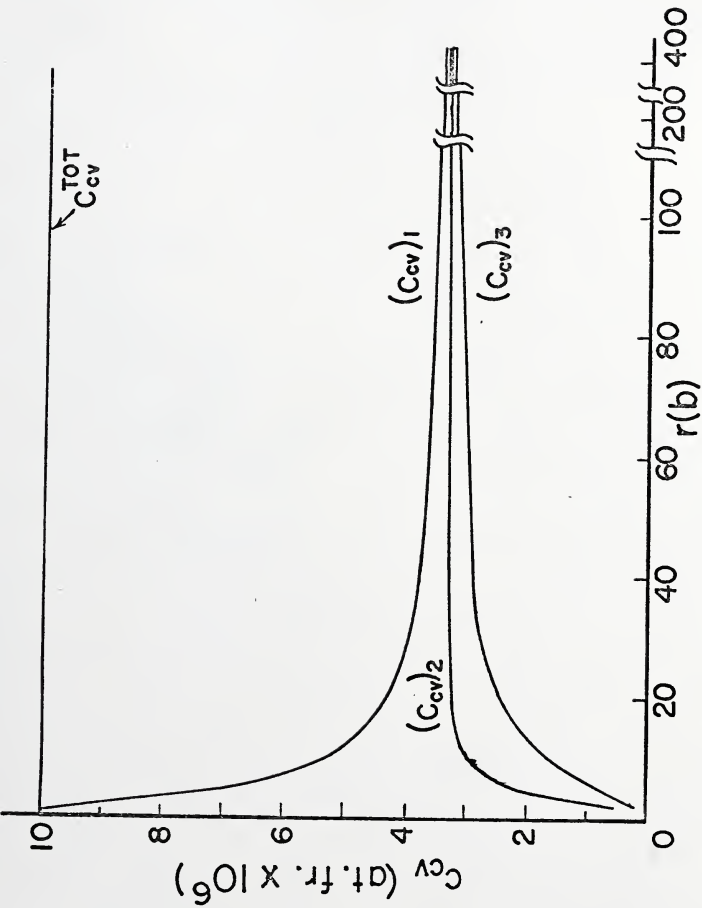


Figure 31. The concentrations of dipoles in each of the three possible orientations ($B' = 0.3$ eV (6900 kcal/mole), $\Lambda = 0.2$ eV (4600 kcal/mole)).

$$dU = u_1 d(n_{cv})_1 + u_2 d(n_{cv})_2 + u_3 d(n_{cv})_3 \quad (26)$$

or substituting Eq. 18 and Eq. 25 into Eq. 26

$$dU = \frac{2\pi b}{\Omega} ((c_{cv})_1 u_1 + (c_{cv})_2 u_2 + (c_{cv})_3 u_3) r dr \quad (27)$$

Assuming that $u_1 = A/r$, $u_2 = 0$ and $u_3 = -A/r$ and substituting these values into Eq. 27 gives

$$dU = \frac{2\pi b A}{\Omega} ((c_{cv})_1 - (c_{cv})_3) dr \quad (28)$$

The total energy change is given by

$$\int_0^{U_0} dU = \frac{2\pi b A}{\Omega} \int_{r_0}^{R_0} ((c_{cv})_1 - (c_{cv})_3) dr \quad (29)$$

where r_0 is an assumed core radius of approximately $1b$ and R_0 is approximately $400b$. It is a very simple matter to numerically evaluate the integral from the graph in Figure 31. Such an integration using $10b$ spacings and the trapezoidal rule gives

$$\int_{1b}^{400b} (c_{cv})_1 dr \approx 3.55 \times 10^{-11} \text{ cm} \quad (30)$$

$$\int_{1b}^{400b} (c_{cv})_3 dr \approx 3.03 \times 10^{-11} \text{ cm} \quad (31)$$

These results when substituted into Eq. 29 give an approximate value for the energy decrease associated with Snoek ordering of existing carbon-vacancy pairs:

$$\begin{aligned} U_0 &\approx (0.52 \times 10^{-11} \text{ cm}) \frac{2\pi\sqrt{2}}{b^2} (0.2 \text{ eV}) \\ &= 1.50 \times 10^4 \text{ eV/cm} \\ &= 2.40 \times 10^{-8} \text{ dyne-cm/cm} \end{aligned} \quad (32)$$

In order to calculate the additional stress needed to remobilize a dislocation from its Snoek atmosphere one may use the following simple relation derived by Schoeck and Seeger [28] which relates the maximum force necessary to free a dislocation from its ordered Snoek atmosphere to U_0 ,

$$F_{\max} = \frac{U_0}{2R} \quad (33)$$

where $R = A/kT$. At 450°K , $A/kT \approx 1.28 \times 10^{-7}$ cm and

$$\Delta\sigma \approx \frac{mU_0}{2bR} \quad (34)$$

where m is an orientation factor which relates shear stresses to tensile stresses and is between 2 and 2.75. Assuming $m = 2.5$, Eq. 34 simplifies to

$$\begin{aligned} \Delta\sigma &\approx 9.4 \times 10^6 \text{ dynes/cm}^2 & (35) \\ &\approx 131 \text{ psi} \\ &\approx 0.90 \text{ MPa} \end{aligned}$$

The above simple calculation is only an estimate of the strength of pinning due to carbon-vacancy pair ordering since the angular dependence of the interaction energies were not taken into account. A more exact expression for U_0 and $\Delta\sigma$ may be calculated in the following analogous fashion.

Due to local ordering of the dipoles the line energy of the dislocation is decreased by an amount U_0 compared with a dislocation surrounded by randomly oriented dipoles. The decrease in energy U_0 is the sum of all interaction energies between individual atoms and

the dislocation and is given by

$$U_o = \int_0^{2\pi} \int_{r_o}^R \Sigma n_i u_i r dr d\theta \quad (36)$$

where R_o is approximately one-half the mean dislocation spacing.

Substituting Eq. 24 into Eq. 36 gives

$$U_o = n_o \int_0^{2\pi} \int_{r_o}^{R_o} \frac{ue^{u/kT} - ue^{-u/kT}}{1 + e^{u/kT} + e^{-u/kT}} r dr d\theta \quad (37)$$

where u is defined by Eq. 17. Noting that $u \ll kT$, one may simplify

Eq. 37:

$$\begin{aligned} U_o &= \frac{2n_o}{3kT} \int_0^{2\pi} \int_{r_o}^{R_o} u^2 r dr d\theta \\ &= \frac{2n_o A^2}{3kT} \int_0^{2\pi} \int_{r_o}^{R_o} (\sin\theta + \sqrt{2} \cos\theta)^2 \frac{dr}{r} d\theta \\ &= \frac{8\pi n_o A^2}{3kT} \ln \frac{R_o}{r_o} \end{aligned} \quad (38)$$

where r_o is approximately the core radius.

This expression is quite similar to that derived by Schoeck and Seeger [28] for bcc metals which is

$$U_o = \frac{\pi n_o A^2}{kT} \ln \frac{3L}{L_o} \quad (39)$$

where $L_o \approx A/kT$. It should be noted that the form of the interaction potential used by Schoeck and Seeger [28] for carbon in alpha iron is different from that used to obtain Eq. 38 and because of this, their analog to Eq. 37 becomes more complicated and not integrable in closed form. Hence, "the integration is carried out...by dividing in different

angular sectors and taking average values of u_i and c_i , the error involved being less than a few percent." The results of Eq. 38 were obtained without any similar assumptions concerning the integration.

Using Eq. 38 to calculate U_0 results in

$$\begin{aligned} U_0 &= 4.90 \times 10^3 \ln \frac{R_0}{r_0} \text{ (eV/cm)} & (40) \\ &= 2.94 \times 10^4 \text{ eV/cm} \\ &= 4.70 \times 10^{-8} \text{ dyne-cm/cm} \end{aligned}$$

Substituting this result into Eqs. 33 and 34 one obtains

$$\begin{aligned} \Delta\sigma &\approx 1.84 \times 10^7 \text{ dynes/cm}^2 & (41) \\ &= 258 \text{ psi} \\ &= 1.78 \text{ MPa} \end{aligned}$$

The inclusion of the angular dependence of the interaction energy approximately doubles the previous result of Eq. 35.

The aging curves in Figures 7 and 8 at the lower temperatures investigated begin at approximately 5 to 6 MPa. These aging curves only commence after approximately 60 seconds. Qualitatively then, the 5 to 6 MPa value is high relative to $\Delta\sigma$ caused by Snoek ordering because the carbon-vacancy dipoles were probably ordered an order of magnitude in time before the experiments began. It is suggested that the value for $\Delta\sigma$ calculated by Eqs. 35 and 41 are in reasonable agreement with the data if one qualitatively extrapolates the $\Delta\sigma$ versus $\log t$ curves to short times consistent, at each temperature, with a vacancy migration distance of approximately $6b$. At 373°K, for example, the jump time of a vacancy is approximately 0.06 seconds. Thus, the formation of pairs and their ordering is complete in approximately 1 second.

The Schoeck-Seeger estimation of approximately 1 to 2 MPa is in fair agreement with this conclusion.

In short, one result of vacancy trapping by carbon atoms after plastic deformation is to create a large number of elastic dipoles which form very quickly because of short range migration of vacancies to adjacent carbon traps. The ordering of the dipoles in the strain field of a dislocation can account for the initial $\Delta\sigma$ obtained on restraining a specimen which has been aged for a very short time at the temperatures investigated. Hence, the curves of $\Delta\sigma$ versus $\log t$ in Figure 7 appear to approach a non-zero value for short times and low aging temperature.

4.2.5 The Mechanism Controlling the Increase in $\Delta\sigma$ with Time

It has been demonstrated [109,118] that the migration energy of a single vacancy in impure nickel during annealing experiments is approximately 1.1 eV (25.3 kcal/mole). In pure nickel, the migration energy has been deduced to be approximately 0.8 to 0.9 eV (18.4 to 20.7 kcal/mole). The difference in energies can be assumed to be due to a binding energy of impurities to vacancies [116]. Thus, the apparent migration energy of vacancies as observed in annealing experiments in nickel is very sensitive to the presence of impurities [117].

The early stages of the static aging experiments give an activation energy consistent with a mechanism involving the migration of vacancies in impure metal. Carbon atoms possess a migration energy of approximately 35 kcal/mole (Table 2) and at the temperatures investigated may be assumed to be immobile for times less than the times to achieve the maxima in $\Delta\sigma$. For example, at 408°K a carbon atom will have jumped only approximately 75 times in 1.2×10^5 seconds [69], the time required

to reach $\Delta\sigma_{\max}$. A random walk distance of only approximately 8 lattice constants will be achieved and this should not result in significant redistribution of the carbon (to dislocations, for example). A vacancy on the other hand with a Q_m approximately equal to 25 kcal/mole will have jumped approximately 10^7 times.

The rise in $\Delta\sigma$, during aging, after the initial Snoek ordering of carbon-vacancy pairs can be rationalized on the basis that stress assisted diffusion of the vacancies toward the dislocation occurs. This aspect can be described by the Cottrell-Bilby model assuming a modulus interaction [139]. Pinning by vacancies alone can result in a small yield point, for example, as obtained in quenched and aged high purity aluminum [140,141]. The maximum yield return is less than 6.9 MPa (1000 psi), however. Nabarro [142] and others [143] have discussed vacancy pinning and indicate that there is considerable doubt that single vacancies can cause significant pinning of dislocations. Thus, it is assumed here that vacancies produced by plastic deformation do not play an important pinning role insofar as direct pinning is concerned. The net effect of vacancy migration toward the dislocation is to form an ordered carbon-vacancy Snoek atmosphere, which because of more pairs being closer to the dislocation causes a significant reduction in the dilatation produced by the dislocation in the metal.

As a first approximation, it is assumed that in the early stages of strain aging (i.e., before the peak in $\Delta\sigma$), very few vacancies reach the core of the dislocation. This assumption is within reason since the effective binding energy of a vacancy to a carbon atom is the sum of the Snoek energy and the binding energy of a vacancy to the

carbon atom. Since the Snoek energy is assumed to vary as r^{-1} , then very close to the dislocation the net effect is for the vacancy to be tightly bound to the carbon atom.

As free vacancies continue to migrate toward the dislocation, it is assumed that a saturated Snoek atmosphere is formed; that is, a fraction, f , of the carbon atoms near the dislocation have single vacancies as nearest neighbors. To relate the increase in $\Delta\sigma$ to time, it is assumed that a "saturated radius" may be defined which grows radially with time. The principal consequence of this assumption is that the carbon-vacancy pair concentration is limited to $f c_c$ radius within R_s where c_c is the atomic fraction of carbon atoms and R_s is the "saturation radius."

The nature of the "saturation radius" may be visualized more clearly in Figure 32. At the beginning of the second stage of aging (after initial Snoek ordering) the concentration profile of the most favored carbon-vacancy pair orientation, as a result of continued vacancy migration, becomes constant for distances closer to the dislocation than r . The value of f must certainly be much less than 1 since it is evident that all carbon atoms cannot be paired to vacancies because of equilibrium considerations. For convenience f is assumed independent of r . As vacancies continue to accumulate, R_s must increase with time. The growth of the saturated Snoek atmosphere will cause the energy of the dislocation and its carbon-vacancy pair atmosphere to decrease with time. Relating the energy decrease to the increase in the yield stress gives the kinetic dependence of $\Delta\sigma$. In addition, the activation energy associated with this process is that for long range vacancy migration in the presence of carbon impurity

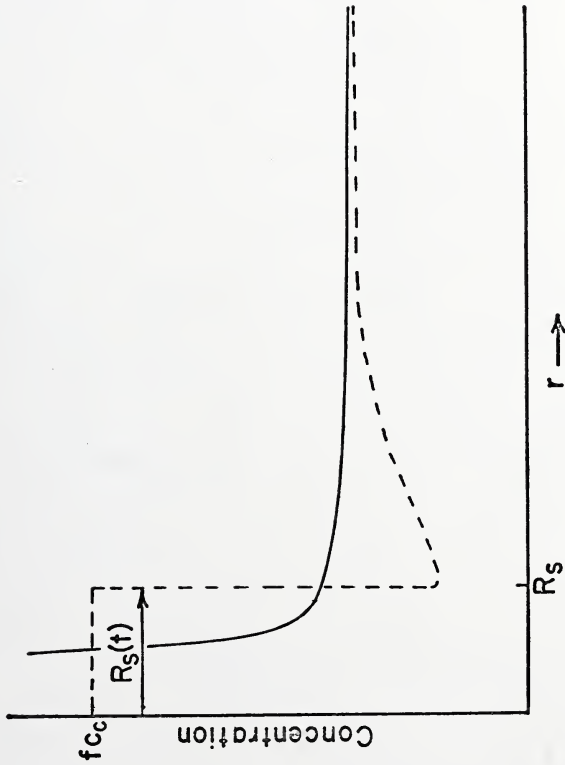


Figure 32. Schematic illustration of the growth of a saturated carbon-vacancy atmosphere. R_s is time dependent and the concentration within R_s is assumed to be a fraction, f , of the carbon concentration.

since the diffusion process, in conjunction with trapping at carbon atoms, controls the supply of carbon-vacancy pairs.

One should recognize the existence of two components of $\Delta\sigma$ which overlap during aging. The first component is attributable to the initial ordering of carbon-vacancy pairs while the second accounts for the increase in $\Delta\sigma$ caused by the growth of the Snoek atmosphere with time. Thus,

$$\Delta\sigma = \Delta\sigma_{\text{initial ordering}} + \Delta\sigma_{\text{atmosphere}} \quad (42)$$

Most of the contribution to $\Delta\sigma$, particularly after time for significant vacancy drift toward the dislocation has elapsed, should be contained in the second term. In view of this, the development of the present model neglects the first term.

Quantitative model of the static strain aging in Nickel 200

From the Cottrell-Bilby model and assuming that the vacancy interaction energy with a dislocation behaves as Ar^{-2} (modulus interaction) [15,138,142], one may deduce the number of vacancies that have arrived at a dislocation in time t as

$$n_v(t) = n_v^0 \pi b \left(\frac{8AD}{kT}\right)^{1/2} t^{1/2} \quad (43)$$

where n_v^0 is the average initial vacancy concentration per unit volume, A is the effective interaction constant of a vacancy, D is the apparent diffusivity of a vacancy in the presence of carbon impurity atoms, and t is the time in seconds. Equation 43 may be rewritten in terms of the atomic fraction of vacancies, c_v , instead of n_v^0 , as

$$n_v(t) = \frac{c_v}{\Omega} \pi b \left(\frac{8AD}{kT}\right)^{1/2} t^{1/2} \quad (44)$$

where Ω is the atomic volume of the solvent.

Assuming that saturation of carbon atoms occurs within a radius r of the dislocation and that the growth of the "saturation radius" is described reasonably well by a two-dimensional growth model, then:

$$\frac{dn_v}{dt} = f n_c (2 \pi r b \frac{dr}{dt}) \quad (45)$$

where dn_v/dt is the accumulation rate of vacancies moving into a cylinder of radius r and depth b between r and $r + dr$ in time dt . The concentration of vacancies in this cylinder is assumed to be $f n_c$ where n_c is the number of carbon atoms per cm^3 and is assumed to be unchanging and independent of position as indicated in the previous section.

Integration of Eq. 45 results in

$$n_v(t) = f \pi R_s^2 b n_c$$

or

$$n_v(t) = f \pi R_s^2 b c_c / \Omega \quad (46)$$

where c_c is the atom fraction of carbon.

Equation 46 can be interpreted as the expression which describes the number of carbon-vacancy pairs accumulated within r at time t since each available vacancy is assumed to be attached to a carbon atom. Equating Eq. 44 to Eq. 46 gives

$$\frac{c_v}{\Omega} \pi b \left(\frac{8AD}{kT}\right)^{1/2} t^{1/2} = \frac{f \pi R_s^2 b c_c}{\Omega} \quad (47)$$

The growth of the ordered Snoek atmosphere is thus approximately given by

$$R_s = \left(\frac{c_v}{f c_c}\right)^{1/2} \left(\frac{8AD}{kT}\right)^{1/4} t^{1/4} \quad (48)$$

Thus, the atmosphere grows approximately as $t^{1/4}$.

Equation 44 is, strictly speaking, the approximate accumulation of vacancies near the dislocation with time. The meaning of Eq. 46, however, is the number of vacancies that have accumulated within R_s ; that is, the vacancies are not arriving at the core of the dislocation as Eq. 44 assumes but are accumulating as R_s grows. Thus, the exact meaning of Eq. 44 is relaxed somewhat to allow for the estimation of the growth of a Snoek atmosphere.

It has been shown (Section 4.2.4) that the decrease in energy associated with Snoek ordering of carbon-vacancy pairs around a dislocation after a time span approximately equal to that required for one reorientation event is approximately

$$U_o = \frac{8\pi n_o A^2}{3kT} \ln \frac{R_o}{r_o} \quad (38)$$

where n_o is the average volume concentration of the ordering species (dipoles) and r_o is approximately the dislocation core radius, lb . R_o is the upper limit of integration on U and is $\rho^{-1/2}/2$, i.e., one-half of the mean dislocation spacing. U_o in this case applies strictly to a quasi-static array of dipoles. That is, no long-range migration of dipoles is assumed to have occurred.

In order to estimate the kinetics of pinning for the present case, it is assumed that only those dipoles (carbon-vacancy pairs) close to the

dislocation are significantly influencing U_0 . That is, only those carbon-vacancy pairs within the "saturation radius" are assumed to contribute to the decrease in energy. This is reasonable since the assumed interaction energy between a dislocation and a carbon-vacancy pair decreases as r^{-1} and at further distances from the dislocation the contribution to pinning of a dislocation by a carbon-vacancy pair reorientation event is small relative to the same event occurring closer to the dislocation. Thus, the upper limit of the integration is approximately R_S rather than one-half the mean dislocation spacing and Eq. 38 becomes

$$U_0 = \frac{8\pi f_c A^2}{3\Omega kT} \ln \frac{R_S}{r_0} \quad (49)$$

where $r_0 \approx b$ and n_0 becomes f_c/Ω .

In order to calculate the increased stress necessary to free a dislocation from its Snoek atmosphere, one needs to know the change in energy associated with moving the dislocation a short distance away from its Snoek atmosphere. That is, one needs to know the behavior of $U(x)$ where x is the displacement of a dislocation from the center of its Snoek atmosphere. $U(0) = U_0$ is the energy decrease caused by stress induced ordering around a dislocation at the center of its Snoek atmosphere. $U(x)$, unfortunately, can only be evaluated numerically. Appendix B illustrates, however, the basic set-up of equations needed to evaluate $U(x)$, the energy of a dislocation displaced a distance $x \ll R_0$ from the center of its Snoek atmosphere, and is based upon the work of Evans and Douthwaite [52]. To calculate the maximum additional force required to free a dislocation from its Snoek atmosphere one needs to know the position x at which the maximum force is experienced.

Then one may compute

$$F_{\max} = -(dU(x)/dx)_{\max} \quad (50)$$

$U(x)$ was not evaluated. However, Schoeck and Seeger [27,28], as noted previously, have estimated the maximum force to be

$$F_{\max} \approx \frac{U_0 kT}{2A} \quad (51)$$

where U_0 is the total interaction energy of the carbon-vacancy dipoles with unit length of a dislocation at the center of the ordered atmosphere ($x=0$) and A is the interaction constant of the carbon-vacancy pair/dislocation.

An estimate of the increased applied tensile stress necessary to free the dislocation from its Snoek atmosphere is approximately given by

$$F_{\max} \approx \frac{b}{m} \Delta\sigma \quad (52)$$

Thus,

$$\Delta\sigma \approx \frac{mkT}{2bA} U_0 \quad (53)$$

where m is an orientation factor between 2 and 2.75. Using the result of Eqs. 49 and 53, one deduces that

$$\Delta\sigma = \frac{4m\pi f_C A^2}{3\eta b} \ln \frac{R_S}{r_0} \quad (54)$$

Thus, the increase in $\Delta\sigma$ is related to the size of the ordered atmosphere. Substituting the time dependent relation for R_S , Eq. 48, into Eq. 54 results in

$$\Delta\sigma = \frac{4\pi\pi f c_c A}{3\Omega b} \ln \left(\frac{c_v}{f c_c} \right)^{1/2} \left(\frac{8AD_o e^{-Q_m/RT}}{kT} \right)^{1/4} \left(\frac{1}{r_o} \right) t^{1/4} \quad (55)$$

It should be noted that this model neglects (a) any migration of carbon atoms, and (b) movement of vacancies within the "saturation radius", R_s , to the dislocation where annihilation might be assumed to occur by elimination of jogs or rapid "pipe" diffusion to other sinks.

Equation 55 may be rewritten as

$$\Delta\sigma = \frac{\pi\pi f c_c A}{3\Omega b} \ln t + \frac{\pi\pi f c_c A}{3\Omega b} \left(-\frac{Q_m}{RT} \right) + \frac{4\pi\pi f c_c A}{3\Omega b} \ln \left(\frac{c_v}{f c_c} \right)^{1/2} \left(\frac{8AD_o}{kT} \right)^{1/4} \left(\frac{1}{r_o} \right) \quad (56)$$

Equation 56 is the increase in flow stress with time caused by the stress enhanced diffusion of vacancies toward the dislocation to form a growing saturated and ordered carbon-vacancy pair atmosphere. Accurately speaking, Eq. 56 is the upper yield point increase which is caused by breakaway of dislocations from their atmospheres. As an approximation, however, the lower yield stress increment, $\Delta\sigma$, should follow the time dependent behavior of the upper yield point much in the same way as in bcc metals which obey Cottrell-Bilby kinetics [2].

The time dependence of $\Delta\sigma$ is reflected only in the first term of Eq. 56, i.e., $\ln t$. Furthermore, the first term also predicts that the slopes of $\Delta\sigma$ versus $\ln t$ curves should be independent of temperature. This feature is reasonably well exhibited in both the $\Delta\sigma$ versus $\log t$ and $\Delta\sigma/\Delta\sigma_{\max}$ versus $\log t$ plots of Figures 7 and 8. The temperature dependence of static strain aging from this model lies in the second and third terms of Eq. 56. The predominant temperature dependence is reflected in the second term. Thus, the model predicts (for times less

than those to achieve maximum hardening) straight $\Delta\sigma$ - $\ln t$ aging curves which are parallel and are simply displaced in time depending upon the size of Q_m and T .

Quantitative predictions of the model

As an example, the 428°K aging curve of Figure 7 was chosen to demonstrate the surprising accuracy of the $\Delta\sigma$ predicted by Eq. 56. The values assumed for the various parameters to obtain a reasonable fit to the data are listed below:

$$m = 2.5$$

$$\Omega = a^3/4 = b^3 \sqrt{2}$$

$$b = 2.49 \times 10^{-8} \text{ cm}$$

$$c_c = 5 \times 10^{-3}$$

$$A = 0.2 \text{ eV} - b = 4.98 \times 10^{-9} \text{ eV-cm}$$

$$D_0 = 1 \text{ cm}^2/\text{s}$$

$$Q_m = 25,200 \text{ cal/mole}$$

$$C_v = 1.2 \times 10^{-9}$$

$$r_0 = b$$

$$f = 0.065$$

These values when substituted into Eq. 56 give

$$\Delta\sigma(\text{MPa}) = 2.414 \ln t - 3.042 \times 10^4 T^{-1} - 2.414 \ln T + 88.679 \quad (57a)$$

or

$$\Delta\sigma(\text{psi}) = 350 \ln t - 4.412 \times 10^6 T^{-1} - 350 \ln T + 1.286 \times 10^4 \quad (57b)$$

Table 7 lists the values for the slopes and intercepts (at $t=1$ second) of the $\Delta\sigma$ versus $\ln t$ curves calculated from Eq. 56. These values may be compared to those of Table 5 obtained from the experimental data of Figure 7. In addition, Figure 33 illustrates the comparison between the model and the experimental data. The agreement is reasonable. Note that the principal unknown which could not be estimated was f the maximum fraction of carbon atoms which can be occupied by vacancies. The value assumed for f is 0.065 and would imply that the solubility limit of carbon-vacancy pairs near a dislocation, that is, the saturation limit, is considerably less than the total number of carbon atoms. This is a reasonable result in view of the comments made by Cocharadt et al. [137] relating to the saturation concentration of carbon in iron near a dislocation. They estimate a maximum carbon concentration of 0.07 atom fraction near edge dislocations and about twice as much near screw dislocations. In addition a variation in f could account for the difference between the upper and lower yield points since the model presented relates to the upper yield point.

The value for the average free vacancy concentration, c_v^f , of 10^{-9} atom fraction is in fair agreement with the 7×10^{-8} value obtained in Section 4.2 which assumed a binding energy of approximately 0.3 eV between carbon atoms and vacancies. Thus, the model as derived can rationalize the aging behavior for times less than the time to achieve a maximum in $\Delta\sigma$.

4.2.6 Regarding the Behavior of Ni 200 After the Peak in $\Delta\sigma$

The quantitative model presented in Section 4.2.5 rationalized that the yield point increase with time is a result of long range

TABLE 7

The Slopes and Intercepts (at $t=1s$) of $\Delta\sigma$
Versus $\ln t$ Curves Calculated from Eq. 56

<u>Temperature</u>	<u>Slope (MPa/$\ln s$)</u>	<u>Intercept</u>
373	2.414	-7.17
408	2.414	-0.39
428	2.414	2.98
448	2.414	6.04
473	2.414	9.50

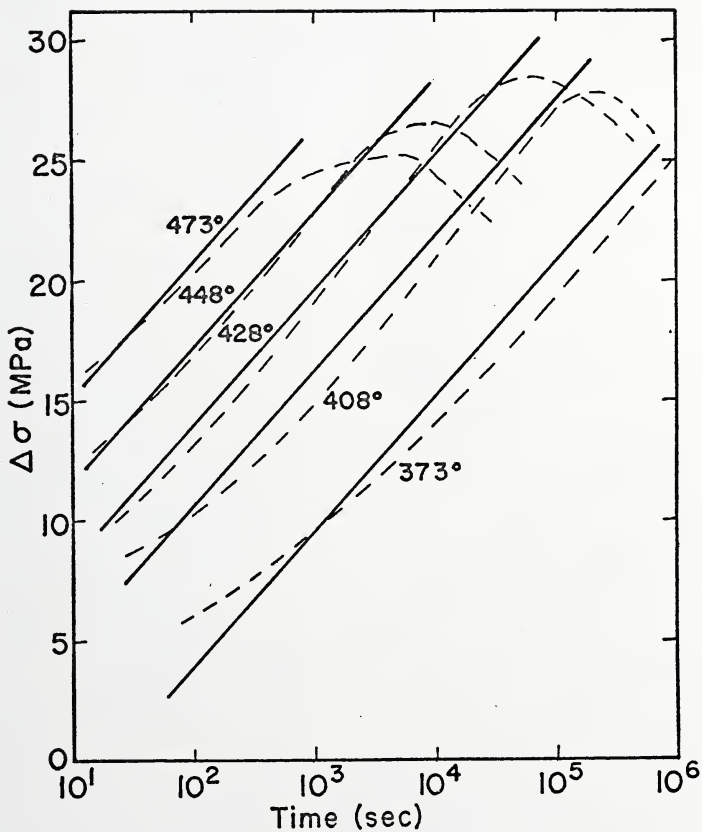


Figure 33. The aging curves obtained from the model for strain aging in Nickel 200 (Eq. 56); the dashed lines are the experimental data (Figure 7).

migration of free vacancies toward the dislocation principally because of the dislocation-vacancy interaction. When the vacancies approach the dislocation, however, they are shown to be more tightly bound to carbon atoms and as a result more carbon-vacancy pairs are formed and via Snoek ordering in the dislocation strain field, the dislocation/carbon-vacancy pair total strain energy is decreased. Hence, additional energy in the form of an increased applied stress is necessary to remobilize the dislocation. This energy was found to be time dependent and, as a first approximation, the vacancies were assumed to saturate a fraction of the carbon atoms near the dislocation. The result is that an ordered Snoek atmosphere grows as a power law in time. The energy, however, was shown to vary as the logarithm of time. The assumption that the flux of vacancies into the core of the dislocation is small at early times is reasonable on the basis that the binding of vacancies to carbon atoms is stronger near the dislocation and, hence, the carbon very near the dislocation essentially slows the flux of vacancies into the dislocation. Also, the flux of vacancies into the saturated atmosphere is probably very large at the beginning of aging, and dominates during the early stages of aging.

Regarding the time required to achieve the maximum in $\Delta\sigma$, it is probable that one of two things occurs. The strengthening is assumed to be a result of the carbon-vacancy pair concentration near the dislocation. A decrease in the number of carbon-vacancy pairs in this region would cause a decrease in $\Delta\sigma$ and may be the result of depletion of vacancies far away from the dislocation. This would slow the flux to the Snoek atmosphere and, hence, R_s would cease to increase the size. In addition, it is probable that with increasing time vacancies attached to carbon

atoms close to the core of the dislocations are migrating to the core in significant numbers relative to the flux into the atmosphere at R_S . Thus, vacancies probably are migrating at this time to the core at a greater rate than can be supplied by the matrix. The net result is that a loss of carbon-vacancy pairs occurs and thereby decreases the energy U_0 of Eq. 38 by decreasing the number of dipoles and, hence, $\Delta\sigma$ decreases.

The rate controlling process responsible for the decrease in $\Delta\sigma$ should be the separation of vacancies from ordered carbon-vacancy pairs and their subsequent migration to the core of a dislocation. The energy associated with this event is $B' + u(b) + E_m$ where B' is the binding energy of a vacancy to a carbon atom, $u(b)$ is the Snoek energy at approximately $r=b$ and E_m is the migration energy of a free vacancy. Thus, the apparent activation energy for this process is higher by an amount $u(b)$ than the energy controlling the rise in $\Delta\sigma$ during the time to reach $\Delta\sigma_{\max}$ (which is $B' + E_m$). Typical values for B' , $u(b)$ and E_m are 0.3, 0.2, and 0.8 eV, respectively. The conclusion is that the activation energy associated with aging at early times is different from that during "overaging" by approximately $u(b)$, the Snoek ordering energy near the dislocation.

Although the data are not as complete for the "overaged" state as during the aging stage, an activation energy was calculated on the basis of the method of cuts at $\Delta\sigma=23\text{MPa}$ and a least squares value of 29.0 kcal/mole (1.26 eV) with a correlation coefficient of 0.973 was obtained. The early aging curves gave an activation energy of approximately 25 to 26 kcal/mole. Thus, the difference in energies is

approximately 3 to 4 kcal/mole (0.13 to 0.17 eV). This is in good agreement with the Snoek energy calculated in Appendix A.

It is very important to point out that the carbon atoms during overaging may be partially responsible for the increased activation energy just calculated. This is because the carbon has had some time to start redistributing by stress assisted drift as predicted by the Cottrell-Bilby model. As previously noted, a carbon atom will have jumped only approximately 75 times during the time for $\Delta\sigma$ to reach $\Delta\sigma_{\max}$. For Cottrell pinning one would expect a considerable number of jumps [12] (of the order of 1000) per interstitial atom for completion of the pinning process since diffusion over fairly large distances is involved. Thus, during overaging some migration of carbon toward dislocations may have occurred. Evidently it is not significant in the time span of the aging times that were investigated because $\Delta\sigma$ never increased again.

It is curious to note, however, that the 473°K curves of Figures 7 and 8 show that $\Delta\sigma$ has slowed its decrease beginning at $t = 2 \times 10^5$ seconds. This may be an indication that carbon may be beginning to cause Cottrell type pinning. In addition, the Lüders extensions shown in Figure 10 for 473, 448 and 428°K may be foreshadowing another possible peak in $\Delta\sigma$ due to, perhaps, the carbon. Generally, in bcc metals the Lüders extension maxima tend to lead in time the $\Delta\sigma$ maxima [2] and this may be a case here for the existence of a second peak.

The secondary hardening curves $\Delta\sigma_H$ versus $\log t$ of Figure 11 also suggest a similar interpretation. Secondary hardening in bcc metals has been associated with the ease of remobilizing dislocations. When the

reloading stress-strain curve no longer extrapolates back to the prestrain stress as in Figure 5 it is generally interpreted as an indication that dislocation multiplication has occurred. This increases ρ above that obtained during normal strain hardening and, hence, the stress level is higher after the passage of the Lüders band down the gage section when normal work hardening resumes, i.e., the metal suffers permanent hardening. This could be the case for Nickel 200 as well. For example, the trend for the 448 and 473°K curves of Figure 11 is for a maximum in $\Delta\sigma_H$ to occur and afterward a significant decrease occurs. This is indicative of dislocation multiplication as hypothesized in previous bcc metals investigations. $\Delta\sigma_H$ probably decreases because of the loss of vacancies (and, therefore, carbon-vacancy pairs) to the cores of dislocations and, hence, remobilization is again favored. Note that for the 473°K $\Delta\sigma_H$ curve a possible minimum in $\Delta\sigma_H$ is achieved and this may be an indication that carbon atoms have begun to migrate in significant numbers to the dislocations and may indicate the beginning of Cottrell pinning by carbon atmospheres.

As suggested previously the austenitic stainless steels are quite similar to nickel in their mechanical behavior. Also, the carbon diffusivities are very similar. Marek and Hochman [66] conducted a very brief survey of static strain aging in as-received Type 316 stainless steel. Their aging temperatures were higher (see their Figure 1) by approximately 150 to 200°K than the temperatures used in this investigation. The interesting point, however, is that they observed peaks in the 0.2% yield stress (of as-received, i.e., prestrained material) during aging with an apparent activation energy of 31 kcal/mole which is close to the diffusivity of carbon in Type 316 stainless. Curiously,

their 0.2% offset curve at 350°C (623°K) shows an initial decrease in yield stress for short aging times. Thus, there is a strong possibility that another peak may have occurred at an earlier time at 350°C (623°K) which they missed because of their higher aging temperatures and long aging times. This may be an aging peak caused by carbon-vacancy pinning such as that observed in Nickel 200. Rose and Glover [37] have attributed room temperature aging under load experiments of similar material to the rotation of carbon-vacancy pairs. Thus, there exists reasonable evidence obtained in some austenitic stainless steels which suggests that aging peaks similar to those observed in Nickel 200 might be observed in these steels if they were aged over an appropriate temperature range.

For extremely long aging times in Nickel 200 it is probable that precipitation of graphite can occur since this alloy is supersaturated. This factor was not observed.

4.3 Summary

The static strain aging model developed in this chapter may be summarized briefly by listing the steps which are believed to occur during static strain aging in Nickel 200:

- (a) Formation of carbon-vacancy pairs and initial ordering which causes an initial $\Delta\sigma$ very quickly (Stage I).
- (b) Migration of free vacancies in the strain field of the dislocation toward the dislocation and the formation of new carbon-vacancy pairs near the dislocation.
- (c) Formation of a saturated Snoek atmosphere around the dislocation which can be described by a size parameter called the "saturated radius."

- (d) Growth of the "saturated radius" and the consequent rise in $\Delta\sigma$ (Stage II).
- (e) Depletion of vacancies in the remainder of the lattice thus decreasing the flux of vacancies into the ordered radius and slowing the rise in $\Delta\sigma$ (Stage III).
- (f) Concomitant migration of vacancies in significant numbers to dislocation cores which causes a decrease in number of carbon-vacancy pairs and, hence, a decrease in $\Delta\sigma$ (Stage IV).
- (g) Probable long range migration of carbon atoms to dislocations; Cottrell-Bilby model may be applicable. There is the possibility that another peak in $\Delta\sigma$ may occur at much later times than in the present case (Stage V).
- (h) Probable precipitation of supersaturated carbon as graphite and final overaging (Stage VI).

A supplementary schematic illustration of the probable behavior of $\Delta\sigma$ with time during aging of Nickel 200 is shown in Figure 34.

4.4 Comments on the Relationship Between Static Strain Aging and Dynamic Strain Aging in Nickel 200

The results of static strain aging experiments on Nickel 200 indicate the very strong possibility that carbon-vacancy pairs interact in a strong way with dislocations and can cause significant pinning. Discontinuous yielding is now considered to arise, in bcc metals particularly, when a low density of free or mobile dislocations develops at a stress sufficient to move dislocations large distances. Dynamic strain aging occurs in a temperature interval where interstitials are mobile enough to cause dynamic pinning so that homogeneous plastic deformation is no longer possible. As a result, a specimen yields

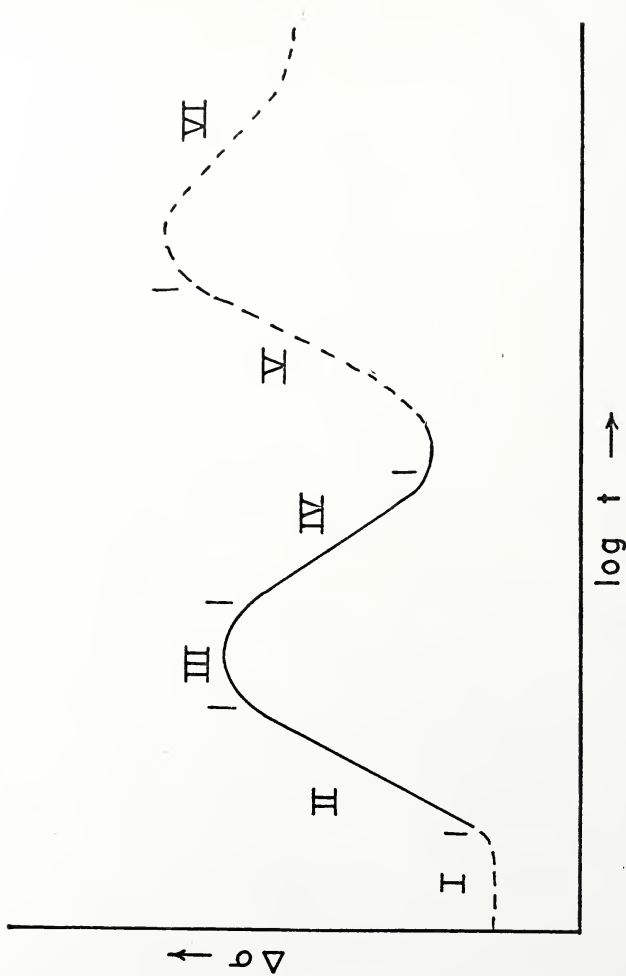


Figure 34. This diagram illustrates the aging stages of Nickel 200. The solid line represents the experimental scope of the present investigation.

locally and produces load drops. Each serration represents a local yield return event. Also, as listed in Table 1, other dynamic effects occur and may be attributed to this critical interstitial mobility.

Internal friction phenomena should be related directly to effects occurring during the deformation of a metal containing interstitials. For example, the use of the torsion pendulum has established that in static strain aging experiments on bcc metals (see, for example, the work of Szkopiak [8] on Nb-O alloys), the Snoek peak (a measure of solute concentration) decreases and the cold work peak (attributable to atmosphere pinning of dislocations) increases. Thus, evidence related to the segregation of impurities to dislocations is available for the bcc metals.

Another important feature of internal friction measurements is that these types of experiments give direct information relating to the mobilities of impurities (e.g., jump times). The mobility of the impurities as deduced by internal friction must be related to dynamic strain aging. Gibala [144] has suggested that during a typical tensile test (10^{-4} s^{-1}) if $\tau \geq 0.1$ second, then a specimen should experience inhomogeneous plastic deformation.

This has been shown to be a quite accurate estimation [130]. For example, in alpha Fe at room temperature, the jump time for a carbon atom is about one second and, indeed, serrated flow is observed.

Although one does not expect an internal friction peak due to single interstitials in fcc metals, one may still estimate an approximate temperature where serrations should begin to be observed; that is, the temperature where $\tau \approx 0.1$ second. For the case of hydrogen [145] in

nickel $D \approx 0.0070 \exp\left(\frac{-9434}{RT}\right)$. Assuming $\tau = a^2/12D$ then one expects to observe serrations beginning at approximately 148°K. Serrations are observed in hydrogenated nickel between approximately 130 and 230°K [57,63]. Thus, for hydrogen in nickel, reasonable agreement is obtained for the onset temperature.

Consider the approximation related to carbon atoms in nickel. The onset temperature assuming [69] $\tau = 3.57 \times 10^{-16} \exp(34800/RT)$, is 523°K. Figure 21 shows very clearly for a rate of $4 \times 10^{-4} \text{ s}^{-1}$, that serrated flow occurs between approximately room temperature and 575°K. The conclusion is that carbon atoms alone are not responsible for serrated flow between these temperatures. That is, if carbon were solely responsible for DSA in Nickel 200, then one would expect on the basis of Gibala's estimation [144] that serrated flow should begin at much higher temperatures than are observed.

Evans and Douthwaite [52] have previously concluded that Snoek ordering of carbon atoms at room temperature in alpha iron could be responsible for serrated flow in agreement with the $\tau \approx 0.1$ second estimation. Thus, it is very possible that dynamic Snoek ordering of carbon-vacancy pairs is occurring during DSA in Nickel 200.

In addition to the observations that the onset of serrated flow can be described using a 15 to 20 kcal/mole activation energy [51,68], the present aging investigation of Nickel 200 indicates an activation energy for the return of the yield point at 5% strain of approximately 25 kcal/mole. This activation energy is not consistent with an explanation based solely upon diffusion of carbon atoms to dislocations and the ensuing pinning process. Nakada and Keh [51] suggested that the low

value of the activation energy for the onset of serrations is different from that normally associated with carbon diffusion (Table 2) because of dislocation pipe diffusion. However, this is not a very tenable explanation [130,146]. Blakemore [147] and Blakemore and Hall [148] have suggested that the Portevin-Le Chatelier Effect could be due to carbide precipitation. However, no indications of carbide or graphite were observed either in their investigation or the present investigation (see Section 3.1).

The very wide range of temperature (300 to 575°K at 10^{-4} s^{-1}) over which serrated flow is observed in Nickel 200 suggests that interactions between carbon atoms and vacancies may occur over a wide span of temperatures. The Portevin-Le Chatelier Effect has been observed in Type 330 stainless steel [53,54] between approximately 550 and 950°K and serrations were rationalized to occur over such a wide range of temperature because of overlapping mechanisms caused by interactions between point defects. The behavior from 550 to about 750°K was attributed to the carbon-vacancy interaction and above 750°K chromium was rationalized to have caused dynamic pinning of dislocations. When no apparent defect interactions occur as in alpha iron, the serrations are observed over a narrower range of temperatures, 340 to 475°K [149,150].

It is possible that in Nickel 200 at the lower end of the DSA temperature interval, predominantly the flipping of carbon-vacancy pairs may be responsible for serrated flow since this, the flipping process, should occur fairly rapid. As the temperature is raised, it is possible that the migration of vacancies is fast enough to increase the carbon-vacancy pair concentration near moving dislocations and may cause stronger pinning as evidenced by Type B serrations. No real

distinction between these two processes occurring at the lower and upper ends of the serration spectrum can be made but this could account for the wide spread in temperature over which the Portevin-Le Chatelier Effect is observed compared to the relatively narrow temperature range of serrations observed in, for example, iron containing carbon.

Additional evidence for the carbon-vacancy pair mechanism relative to serrated flow in Nickel 200 indicates that both carbon and vacancies must be present for aging to occur. Materials in which interstitials alone are responsible for hardening, such as low carbon steels [149] and Ni-H [57,63] have serrations starting at the onset of plastic flow. Nakada and Keh [51] observed that a finite strain was required before serrations initiated in Ni-C alloys. Initial smooth regions of plastic flow have only been found in fcc alloys in which substitutional solute atoms cause serrations. This is generally believed to result from the diffusion rate of substitutional atoms in these materials being too slow to enable them to cause serrations during tensile testing. As straining proceeds, the vacancy concentration increases and the solute atoms can move just fast enough to initiate jerky flow. Hence, the smooth region of plastic flow is a measure of the concentration of vacancies needed to increase the diffusion rate at a given temperature to a level where the solute is mobile enough to cause serrations [151]. The observation by Nakada and Keh [51] of a small but finite incubation strain supports the existence of the carbon-vacancy pair in Ni-C alloys and in Nickel 200.

CONCLUSIONS AND OBSERVATIONS

1. The carbon-vacancy pair is a defect which can be rationalized to cause strain aging in Nickel 200.
2. The rise in $\Delta\sigma$ during static strain aging is very slow in Nickel 200 and may be described in terms of a $\ln t$ time law. An approximation for comparison to aging phenomena in other metals and alloys is a $t^{1/7}$ time dependence.
3. The activation energy controlling the rise in $\Delta\sigma$ is about 25 kcal/mole (1.1 eV/atom) and apparently represents the migration energy of a vacancy in the presence of carbon impurity.
4. Pinning in Nickel 200 can be rationalized as being due to the stress induced ordering of carbon-vacancy dipoles in the strain fields of dislocations.
5. Six stages are believed to occur during static strain aging of Nickel 200:
 - a. the formation of carbon-vacancy pairs and their initial ordering (Stage I);
 - b. the migration of vacancies in the strain energy gradient of a dislocation, the formation of new carbon-vacancy pairs near dislocations and the growth of an ordered carbon-vacancy dipole atmosphere (Stage II);
 - c. depletion of free vacancies in the remainder of the lattice due to movement towards dislocations and to sinks in general which

decreases the flux to the ordered atmosphere and therefore slows the rise in $\Delta\sigma$ (Stage III);

d. eventual loss of vacancies from carbon-vacancy pairs due to migration to dislocation sinks which causes $\Delta\sigma$ to decrease at long times (Stage IV);

e. the migration of carbon atoms in the strain fields of dislocations and the growth of a carbon Cottrell atmosphere (Stage V);

f. possible precipitation of graphite and overaging (Stage VI).

6. Nickel 200 exhibits dynamic strain aging between approximately 300 and 600°K depending upon strain rate.
7. Dynamic Snoek ordering of carbon-vacancy pairs can account for serrated flow in Nickel 200. The carbon-vacancy pair possesses the necessary mobility to cause DSA over a wide range of temperatures unlike single carbon atoms in alpha iron, for example.
8. Nickel 270 does not exhibit significant strain aging.
9. Enhanced strengthening as measured by the ultimate tensile strength is not caused by anomalous work hardening but to a prolonging of Stage II activity, i.e., single slip, which gives rise to a ductility maximum at 525°K.
10. Nickel 200 does not exhibit abnormal rate dependent work hardening as defined by $\log \theta$ versus $\log \sigma$ plots.
11. Nickel 200 exhibits a 0.2% yield stress plateau between approximately 300 and 475°K.
12. Discontinuous yielding in Nickel 200 is in agreement with the results of Nakada and Keh [51] who tested purer Ni-C alloys and obtained onset and termination activation energies of 15 ± 2 and 26 ± 4 , respectively.

13. Nickel 200 exhibits a well-defined reduction in area minimum in the DSA interval which has an apparent activation energy of approximately 25 kcal/mole.

APPENDICES

APPENDIX A

COMPUTATION OF THE INTERACTION ENERGY BETWEEN A CARBON-VACANCY PAIR DEFECT AND SCREW DISLOCATIONS IN FCC METALS

The technique used for obtaining the interaction energy is based on the work of Barnett and Nix [152]. Briefly, this method assumes that a tetragonal defect can be created by permitting the material within a small spherical volume, Ω , to undergo a pure shear transformation strain.

$$\epsilon_{ij}^T = \epsilon \begin{pmatrix} 2 & 0 & 0 \\ 0 & -1 & 0 \\ 0 & 0 & -1 \end{pmatrix} \quad (58)$$

This equation is written for a coordinate system aligned with the principal distortion axes of the defect. The total interaction energy between the tetragonal defect and an internal stress p'_{ij} is

$$E_{int} = - \int_V p'_{ij} \epsilon_{ij}^T dv \quad (59)$$

($i, j = 1, 2, 3$ with summation over repeated indices implied). Since there is no hydrostatic component of the stress tensor for any of the screw dislocations ($p'_{ii} = 0$), one may split the transformation strain, ϵ_{ij} , into two parts

$$E_{int} = \epsilon \begin{pmatrix} -1 & 0 & 0 \\ 0 & -1 & 0 \\ 0 & 0 & -1 \end{pmatrix} + 3\epsilon \begin{pmatrix} 1 & 0 & 0 \\ 0 & 0 & 0 \\ 0 & 0 & 0 \end{pmatrix} \quad (60)$$

then

$$E_{int} = -\int_V p'_{ij} \epsilon_{ij}^T dv = -3\Omega \epsilon p'_{11} \quad (61)$$

where p'_{11} is the 11 component of the dislocation stress field aligned with the principal axes of the tetragonal defect (carbon-vacancy pair). This is quite convenient because the interaction energy is easily obtained by calculating only one component of the dislocation strain field.

Let x'_1 , x'_2 , and x'_3 be the defect coordinate axes and x_1 , x_2 , and x_3 be the coordinate axes for a right handed screw dislocation. The x'_1 axis corresponds to the largest principal distortion of the defect. The dislocation lies along x_3 and glides in the x_1 - x_3 plane. Let $p_{\alpha\beta}$ ($\alpha, \beta = 1, 2, 3$) represent the dislocation stress field expressed in the dislocation coordinate system. The stress component needed for the computation of the interaction energy is obtained by transforming p'_{11} to $p_{\alpha\beta}$ using

$$p'_{11} = l_{1\alpha} l_{1\beta} p_{\alpha\beta} \quad (62)$$

where $l_{1\alpha}$ and $l_{1\beta}$ are the direction cosines between the x'_1 and the x_α and x_β axes, respectively. The only non-zero components of $p_{\alpha\beta}$ are p_{13} and p_{23} so that

$$E_{int}(x_1, x_2) = -(3\Omega\epsilon) 2\{l_{11}l_{13}p_{13}(x_1, x_2) + l_{12}l_{13}p_{23}(x_1, x_2)\} \quad (63)$$

Next consider the specific case of an fcc metal with a $\langle 100 \rangle$ tetragonal defect. Barnett and Nix [152] in their discussion utilized a $\langle 111 \rangle$ tetragonal defect which possesses four possible orientations. For the case of $\langle 100 \rangle$ defects (carbon-vacancy pairs) only three orientations are

possible and the interactions are different. The dislocation coordinates are taken to be: $x_1 = 1/\sqrt{6} [1\bar{2}1]$, $x_2 = 1/\sqrt{3} [111]$, $x_3 = 1/\sqrt{2} [\bar{1}01]$.

The three possible orientations of the carbon-vacancy pair are:

$x'_1 = 1/\sqrt{2} [001]$, $1/\sqrt{2} [010]$, $1/\sqrt{2} [100]$. The interaction energies for each of these orientations are given in Table 8.

The components of the stress field of a screw dislocation in the fcc structure are given by Hirth and Lothe [153] for the general case of anisotropy. For isotropy

$$P_{13} = - \frac{C_{44}b}{2\pi} \frac{x_2}{x_1^2 + x_2^2} \quad (64)$$

$$P_{23} = \frac{C_{44}b}{2\pi} \frac{x_1}{x_1^2 + x_2^2} \quad (65)$$

Thus, the interaction energy for a [001] defect is

$$E_{int} = - \frac{3}{\sqrt{3}} \Omega \epsilon \frac{C_{44}b}{4\pi r} (\sin \theta + \sqrt{2} \cos \theta) \quad (66)$$

where $\Omega = a^3/4$ (the atomic volume of a solvent atom). The value for ΔV the dilatation, due to carbon in nickel can be deduced from the lattice parameter measurements of Ni-C alloys determined by Zwell et al. [115]. Their result is

$$a(\text{\AA}) = 3.5238 + 0.74c_c \quad (67)$$

where a is the lattice parameter in Angstroms and c_c is the carbon concentration in atomic fraction. The dilatation caused by carbon can be estimated from [154]

TABLE 8

Interaction Energies for Tetragonal Defects in the FCC Structure

Perfect Orientation	Dislocation Coordinates*			Direction Cosines			Interaction Energy
	x_1	x_2	x_3	b_{11}	b_{12}	b_{13}	
$\frac{1}{\sqrt{2}} [001]$	$\frac{1}{\sqrt{6}} [\bar{1}\bar{2}\bar{1}]$	$\frac{1}{\sqrt{3}} [111]$	$\frac{1}{\sqrt{2}} [\bar{1}01]$	$\frac{1}{2\sqrt{3}}$	$\frac{1}{\sqrt{6}}$	$\frac{1}{2}$	$-\frac{3}{\sqrt{3}} \Omega \epsilon \left(\frac{P_{13}}{2} + \frac{P_{23}}{\sqrt{2}} \right)$
$\frac{1}{\sqrt{2}} [010]$	$\frac{1}{\sqrt{6}} [1\bar{2}\bar{1}]$	$\frac{1}{\sqrt{3}} [111]$	$\frac{1}{\sqrt{2}} [\bar{1}01]$	$-\frac{1}{\sqrt{3}}$	$\frac{1}{\sqrt{6}}$	0	0
$\frac{1}{\sqrt{2}} [100]$	$\frac{1}{\sqrt{6}} [1\bar{2}\bar{1}]$	$\frac{1}{\sqrt{3}} [111]$	$\frac{1}{\sqrt{2}} [\bar{1}01]$	$\frac{1}{2\sqrt{3}}$	$\frac{1}{\sqrt{6}}$	$-\frac{1}{2}$	$+\frac{3}{\sqrt{3}} \Omega \epsilon \left(\frac{P_{13}}{2} + \frac{P_{23}}{\sqrt{2}} \right)$

* Screw dislocation lies along $[\bar{1}01]$

$$\Delta V = \frac{3}{a} \frac{da}{dc} \Omega \quad (68)$$

Substitution of the appropriate values into Eq. 68 gives

$$\frac{\Delta V}{V} = 0.63 \quad (69)$$

Thus, as an average $\epsilon = 0.21$. This value can be rationalized from the hard ball model as well by assuming that the carbon atom in the lattice is about 1.54\AA in diameter (its size in the diamond lattice [155]) and can be squeezed into the body-centered position of the fcc unit cell. This approximation gives a misfit of 0.15, less than the lattice parameter estimate. The vacancy on a 100 site should relax the strain somewhat. However, exactly how much it should relax the carbon dilatation is unknown. For the purposes of this discussion a value of $\epsilon = 0.1$ has been assumed for the carbon-vacancy pair. Thus, for the [001] defect

$$E_{\text{int}} = - \frac{4.682 \times 10^{-21}}{r} (\sin \theta + \sqrt{2} \cos \theta) \text{ erg-cm} \quad (70)$$

In addition, it is assumed that $\theta = 0$ in order to estimate the size of the interaction constant. On this basis

$$E_{\text{int}} \approx - \frac{6.62 \times 10^{-21} \text{ erg-cm}}{r} = - \frac{0.17\text{eV-b}}{r} \quad (71)$$

At $r = b = 2.49 \times 10^{-8}$ cm, $E_{\text{int}} = 2.66 \times 10^{-13}$ ergs = 0.17eV. Thus, the interaction energy is estimated to be about 0.2 eV.

From Table 8 it is evident that the [001] defect possesses the lowest interaction energy. Hence, it is possible that reorientation of the other defects into [001] directions can lower the total

interaction energy between the dislocation and defects. This type of ordering could probably occur in the strain field of an edge dislocation as well. However, as for the case of bcc metals [137] the form of the interaction energies of the three classes of defects with an edge dislocation is probably more complicated than for the screw dislocation. The magnitude of the interactions are probably similar as pointed out by Cochardt et al. [137].

Note that for the case of a 001 dipole interacting with a screw dislocation in an fcc metal

$$u_1 = -\frac{A}{r} (\sin \theta + \sqrt{2} \cos \theta) = u \quad (72a)$$

$$u_2 = 0 \quad (72b)$$

$$u_3 = -u \quad (72c)$$

where the subscripts indicate the three possible dipole orientations. Figure 35 illustrates the behavior of the interaction energies of Eq. 72 on angular position of the dipoles around the screw dislocation.

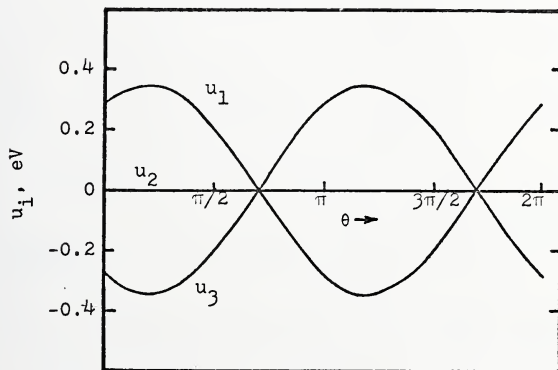


Figure 35. The interaction potential u_i of a carbon-vacancy dipole with a screw dislocation for $r = b$ and $A/b = 0.2$ eV.

APPENDIX B

DETERMINATION OF $U(x)$, THE ENERGY OF A SCREW DISLOCATION DISPLACED A DISTANCE x FROM THE CENTER OF ITS SNOEK ATMOSPHERE

The purpose of this appendix is to briefly present the method of Evans and Douthwaite [152] used to calculate $U(x)$, the strain energy increase which a dislocation experiences when moved a small distance x from the center of its equilibrium Snoek atmosphere.

The maximum force on a dislocation moving away from its static, equilibrium Snoek atmosphere is found by calculating the interaction energy of the dislocation as a function of its displacement, x , from the center of the atmosphere. The logic used is based upon the Schoeck and Seeger [28] calculation of U_0 , the total interaction energy of dipoles with a screw dislocation and the assumption made by Evans and Douthwaite that as a consequence of displacing a dislocation to x , repopulation of the three possible dipole orientations does not occur appreciably. However, the energy, $U(x)$, does change. Figure 1 of Evans and Douthwaite [152] demonstrates the geometry of the situation.

When the dislocation is displaced a distance x ($x \ll L$) from the center of the equilibrium atmosphere, the coordinates of any point (r, θ) relative to the dislocation at $x = 0$ become (r', θ') relative to the dislocation at x and the interaction energy is given approximately by

$$U(x) = \int_0^{2\pi} \int_0^L \sum_i n_i u_i' r' dr' d\theta' \quad (i = 1, 2, 3) \quad (73)$$

where n_i is the number of dipoles per unit volume in the i^{th} possible orientation at a position r and is given by the probability function in the text (Eq. 24). In Eq. 73 the u_i' have the same form as the u_i given by Eq. 72 and the new coordinates are related to the old coordinates by

$$r^2 = r'^2 + x^2 + 2r' x \cos \theta' \quad , \quad \sin \theta = r' \sin \theta' / r \quad (74)$$

Simplifying Eq. 73 gives

$$U(x) = \int_0^{2\pi} \int_0^L (n_1 u_1' + n_2 u_2' + n_3 u_3') r' dr' d\theta' \quad (75)$$

Thus, in new coordinates (i.e., after the dislocation moves to x), r is replaced by r' . Using Eq. 24 for the n_i and substituting into Eq. 36 gives

$$U(x) = n_0 \int_0^{2\pi} \int_0^L \frac{u' e^{u/kT} - u' e^{-u/kT}}{1 + e^{u/kT} + e^{-u/kT}} r' dr' d\theta' \quad (76)$$

A reasonable assumption is that $u \ll kT$. As a result, the exponentials may be expanded and the integral becomes

$$U(x) = \frac{2}{3} n_0 \frac{A^2}{kT} \int_0^{2\pi} \int_0^L (\sin \theta' + \sqrt{2} \cos \theta') (\sin \theta + \sqrt{2} \cos \theta) \frac{dr'}{r} d\theta' \quad (77)$$

Utilizing transformation equations relating r to r' and θ to θ' , Eq. 74, the author has concluded that Eq. 77 is not integratable in closed form. Thus, a numerical approach is in order. Due to time considerations, Eq. 77 was not evaluated numerically. Using the results of a tabulation of $U(x)$, however, one may deduce $F_x = -dU(x)/dx$ and the equivalent maximum applied shear stress required to free the dislocation from its

Snoek atmosphere, $\Delta\tau_{\max} = - (dU(x)/dx)_{\max}/b$. Using a suitable orientation factor one may calculate the tensile equivalent of the shear stress. Best estimates [28] indicate that this maximum stress occurs when

$$\Delta\tau \approx U_0/2R \quad (78)$$

where U_0 is the total energy decrease caused by stress induced ordering of dipoles and $R = A/kT$.

BIBLIOGRAPHY

1. R. E. Reed-Hill: Reviews on High-Temperature Materials, 1974, vol. 2(3), pp. 217-42.
2. J. D. Baird: Met. Rev., 1971, vol. 5, Review No. 149, pp. 1-18.
3. E. S. Davenport and E. C. Bain: Trans. Amer. Met. Soc., 1935, vol. 23, p. 1047.
4. M. Gensamer and J. R. Low: Trans. AIME, 1944, vol. 224, p. 207.
5. J. W. Edington, T. C. Lindley and R. E. Smallman: Acta Met., 1964, vol. 12, pp. 1025-31.
6. Z. C. Szkopiak: Acta Met., 1968, vol. 16, pp. 381-91.
7. C. S. Hartley: Acta Met., 1966, vol. 14, pp. 1237-46.
8. G. W. Brock: Trans. AIME, 1961, vol. 221, pp. 1055-62.
9. A. H. Cottrell and B. A. Bilby: Proc. Phys. Soc. London, 1949, vol. A62, pp. 49-62.
10. B. B. Hundy: Metallurgia, 1956, vol. 53, p. 203.
11. W. R. Thomas and G. M. Leak: J. Iron and Steel Inst., 1960, vol. 180, p. 155.
12. S. H. Carpenter: Ph.D. Dissertation, University of Utah, 1964, pp. 56-59.
13. S. Harper: Phys. Rev., 1951, vol. 83, pp. 709-12.
14. F. S. Ham: J. Appl. Phys., 1959, vol. 30, pp. 915-26.
15. R. Bullough: Dislocations, A course of lectures given at the Post Graduate Education Center, Harwell from February to May, 1964, Lecture 7.
16. A. H. Cottrell: Dislocations and Plastic Flow in Crystals, Clarendon Press, 1953, pp. 134-50.

17. E. O. Hall: Yield Point Phenomena in Metals and Alloys, Plenum Press, 1970, pp. 173-75.
18. C. S. Hartley: Ph.D. Dissertation, Ohio State University, 1965.
19. C. L. Formby: Ph.D. Dissertation, University of Liverpool, 1964.
20. H. Suzuki: Dislocations and Mechanical Properties of Crystals, John Wiley and Sons, 1957, pp. 361-92.
21. E. O. Hall, Yield Point Phenomena in Metals and Alloys, Plenum Press, 1970, p. 55.
22. I. L. Dillamore and R. E. Smallman: Phil. Mag., 1965, vol. 12, pp. 191-93.
23. T. Jøssang and J. P. Hirth: Phil. Mag., 1966, vol. 13, pp. 657-70.
24. J. P. Hirth and J. Lothe: Theory of Dislocations, 1968, McGraw-Hill, p. 298.
25. A. A. Hendrickson and M. E. Fine: Trans. AIME, 1961, vol. 221, pp. 103-09.
26. D. E. Sonon and G. V. Smith: Trans. AIME, 1968, vol. 242, pp. 1527-33.
27. G. Schoeck: Phys. Rev., 1956, vol. 102, pp. 1458-59.
28. G. Schoeck and A. Seeger: Acta Met., 1959, vol. 7, pp. 469-77.
29. J. L. Snoek: Physica, 1941, vol. 8, p. 711.
30. B. S. Berry and A. S. Nowick: Physical Acoustics, Principles and Methods, W. P. Mason, ed., vol. IIA, Academic Press, New York, 1966, pp. 1-42.
31. H. G. van Bueren: Imperfections in Crystals, North Holland, Amsterdam, 1961, pp. 40-44, 156-59, 386-89.
32. A. S. Nowick and B. S. Berry: Anelastic Relaxation in Crystalline Solids, Academic Press, 1972, pp. 226-46.
33. R. W. Powers and M. V. Doyle: J. Appl. Phys., 1959, vol. 30, pp. 514-24.
34. D. V. Wilson, B. Russell with an Appendix by J. D. Eshelby: Acta Met., 1959, vol. 7, pp. 628-31.

35. O. P. Quist and S. H. Carpenter: Acta Met., 1975, vol. 23, pp. 321-28.
36. W. S. Owen and M. J. Roberts: Dislocation Dynamics, A. R. Rosenfield et al., eds., Battelle Institute Colloquium, McGraw-Hill, 1967, pp. 357-79.
37. K. S. B. Rose and S. G. Glover: Acta Met., 1966, vol. 14, pp. 1505-16.
38. Y. Nakada and A. S. Keh: Acta Met., 1967, vol. 15, pp. 879-83.
39. H. W. Paxton: J. Appl. Phys., 1953, vol. 24, pp. 104-05.
40. T. Mura and J. O. Brittain: Acta Met., 1960, vol. 8, pp. 767-72.
41. J. O. Brittain and S. E. Bronisz: Trans. AIME, 1960, vol. 218, pp. 289-94.
42. E. A. Almond and D. Hull: Phil. Mag., 1966, vol. 14, pp. 515-29.
43. W. R. Cribb: Unpublished research.
44. J. T. Evans and R. M. Douthwaite: Acta Met., 1973, vol. 21, pp. 49-54.
45. D. V. Wilson and B. Russell: Acta Met., 1960, vol. 8, pp. 36-45.
46. D. V. Wilson and B. Russell: Acta Met., 1960, vol. 8, pp. 468-79.
47. J. Heslop and N. J. Petch: Phil. Mag., 1956, vol. 1, pp. 866-73.
48. N. J. Petch: J. Iron and Steel Inst., 1953, vol. 174, p. 25.
49. A. Cracknell and N. J. Petch: Acta Met., 1955, vol. 3, pp. 186-89.
50. A. R. Rosenfield and W. S. Owen: Trans. Met. Soc. AIME, 1963, vol. 227, pp. 603-08.
51. Y. Nakada and A. S. Keh: Acta Met., 1970, vol. 18, pp. 437-43.
52. J. T. Evans and R. M. Douthwaite: Acta Met., 1973, vol. 21, pp. 49-54.
53. J. Glen: J. Iron and Steel Inst., 1957, vol. 186, p. 21.
54. C. F. Jenkins and G. V. Smith: Trans. AIME, 1969, vol. 245, pp. 2149-56.

55. E. Macherauch, K. Kolb and H. Christian: Z. Naturforschg., 1961, vol. 16A, pp. 1113-14.
56. E. Macherauch and O. Vöhringer: Acta Met., 1963, vol. 11, pp. 157-58.
57. T. Boniszewski and G. C. Smith: Acta Met., 1963, vol. 11, pp. 165-78.
58. V. F. Sukhovarov: Phys. Met. Metall., 1962, vol. 13, pp. 109-13.
59. V. F. Sukhovarov, N. A. Aleksandrov and L. A. Kudryavtseva: Phys. Met. Metall., 1962, vol. 14(6), pp. 82-5.
60. B. A. Wilcox and G. C. Smith: Acta Met., 1964, vol. 12, pp. 371-76.
61. A. H. Windle and G. C. Smith: Met. Sci. J., 1968, vol. 2, pp. 187-91.
62. A. H. Windle and G. C. Smith: Met. Sci. J., 1970, vol. 4, pp. 136-44.
63. B. A. Wilcox and G. C. Smith: Acta Met., 1965, vol. 13, pp. 331-43.
64. J. S. Blakemore: Met. Trans., 1970, vol. 1, pp. 151-56.
65. J. S. Blakemore: Met. Trans., 1970, vol. 1, pp. 145-49.
66. M. Marek and R. F. Hochman: Scripta Met., 1969, vol. 3, pp. 693-98.
67. V. F. Sukhovarov and R. P. Kharlova: Phys. Met. Metall., 1960, vol. 10, pp. 143-46.
68. L. Y. Popov and V. F. Sukhovarov: Phys. Met. Metall., 1964, vol. 17(3), pp. 100-05.
69. S. Diamond and C. Wert: Trans. Met. Soc. AIME, 1967, vol. 239, pp. 705-09.
70. A. B. Shovensin, A. H. Minkevitch and G. B. Scherbinski: Izvestiya Vysshikh Vchelon Zavedenii Chernaya Met., 1965, pp. 95-8.
71. P. L. Gruzin, In. A. Polickarpov and G. B. Federov: Phys. Met. Metall., 1957, vol. 4, pp. 94-102.
72. Diffusion Data, 1967, vol. 1, p. 28.

73. M. Wuttig and H. K. Birnbaum: Appl. Phys. Letters, 1965, vol. 7, pp. 320-22.
74. S. Kinoshita, P. J. Wray and G. T. Horne: Trans. AIME, 1965, vol. 233, pp. 1902-04.
75. G. Zankl: Z. Naturforschg., 1963, vol. 18A, pp. 795-809.
76. E. Macherauch: Z. Metallkde., 1964, vol. 55, pp. 60-82.
77. C. Schwink and W. Vorbrugg: Z. Naturforschg., 1967, vol. 22A, pp. 626-42.
78. C. Schwink and D. Knoppik: Phys. Stat. Sol., 1965, vol. 8, pp. 729-38.
79. D. Krause and E. Göttler: Phys. Stat. Sol., 1965, vol. 9, pp. 485-98.
80. U. Essman, M. Rapp and M. Wilkens: Acta Met., 1968, vol. 16, pp. 1275-87.
81. O. Vöhringer and E. Macherauch: Z. Metallkde., 1967, vol. 58, pp. 21-8.
82. S. Mader: Z. Physik, 1957, vol. 149, pp. 73-102.
83. R. E. Reed-Hill, W. R. Cribb and S. N. Monteiro: Met. Trans., 1973, vol. 4, pp. 2665-67.
84. J. F. Bell: The Physics of Large Deformation of Crystalline Solids, Springer-Verlag, New York, 1968.
85. W. B. Morrison: Met. Trans., 1971, vol. 2, pp. 331-32.
86. Y. Bergström and B. Aaronsson: Met. Trans., 1970, vol. 1, pp. 1029-30.
87. C. Crussard and B. Jaoul: Rev. Met., 1950, vol. 47, pp. 589-600.
88. C. Crussard: Rev. Met., 1953, vol. 10, pp. 696-709.
89. B. Jaoul: J. Mech. Phys. Solids, 1957, vol. 5, pp. 95-114.
90. V. S. Arunachalam, S. Pattanaik, S. N. Monteiro and R. E. Reed-Hill: Met. Trans., 1972, vol. 3, pp. 1009-11.
91. S. N. Monteiro and R. E. Reed-Hill: Met. Trans., 1973, vol. 4, pp. 1011-15.

92. H. W. Swift: J. Mech. Phys. Solids, 1952, vol. 1, pp. 1-18.
93. M. Ahlers: Met. Trans., 1970, vol. 1, pp. 2415-27.
94. B. E. P. Beeston, I. L. Dillamore and R. E. Smallman: Met. Sci. J., 1968, vol. 2, pp. 12-14.
95. A. M. Garde and R. E. Reed-Hill: "Zirconium in Nuclear Applications," ASTM STP 551, American Society for Testing and Materials, 1974, pp. 75-91.
96. D. Vöhringer: Mat. Sci. and Engr., 1968, vol. 3, pp. 299-302.
97. D. N. Beshers: J. Metals, 1968, vol. 20, pp. 19-23.
98. C. A. Wert: Physical Acoustics, Principles and Methods, W. P. Mason, ed., vol. IIIA, Academic Press, New York, 1966, pp. 44-75.
99. E. Adler and C. Radeloff: J. Appl. Phys., 1969, vol. 40, pp. 1526-33.
100. T. L. Wu and C. M. Wang: Scientia Sinica, 1958, vol. 7, pp. 1029-53.
101. A. S. Nowick and B. S. Berry: Anelastic Relaxation in Crystalline Solids, 1972, Academic Press, p. 321.
102. T. Kê and C. Tsien: Scientia Sinica, 1956, vol. 5, pp. 625-43.
103. T. Kê, C. Tsien and K. Misek: Scientia Sinica, 1955, vol. 4, pp. 519-26.
104. C. Tsien: Scientia Sinica, 1961, vol. 10, pp. 930-37.
105. T. Kê and C. Wang: Scientia Sinica, 1955, vol. 4, pp. 501-18.
106. F. Seitz: Adv. Phys., 1953, vol. 1, pp. 43-90.
107. M. G. Ulitschny and R. Gibala: Met. Trans., 1973, vol. 4, pp. 497-506.
108. H. Kressel and N. Brown: J. Appl. Phys., 1967, vol. 38, pp. 1618-25.
109. A. van den Beukel: Vacancies and Interstitials in Metals, A. Seeger, D. Schumacher, W. Schilling and J. Diehl, eds, North-Holland, Amsterdam, 1969, pp. 427-81.

110. A. Seeger and H. Mehrer: Vacancies and Interstitials in Metals, A. Seeger, D. Schumacher, W. Schilling and J. Diehl, eds., North-Holland, Amsterdam, 1969, pp. 1-58.
111. B. L. Shriver and M. Wuttig: Acta Met., 1972, vol. 20, pp. 1-4.
112. M. Wuttig and H. K. Birnbaum: J. Phys. Chem. Solids, 1966, vol. 27, pp. 225-34.
113. J. Friedel: Dislocations, Pergamon Press, 1964, pp. 400-04.
114. Metals Handbook, vol. 1, ASM, Metals Park, Ohio, p. 44.
115. L. Zwell, E. J. Fasiska, Y. Nakada and A. S. Keh: Trans. Met. Soc. AIME, 1968, vol. 242, pp. 765-66.
116. A. C. Damask and G. J. Dienes: Point Defects in Metals, Gordon and Breach, New York, 1963, pp. 21-25.
117. P. Simson and R. Sizmann: Z. Naturforschg., 1962, vol. 17A, pp. 596-603.
118. A. Sosin and J. A. Brinkman: Acta Met., 1959, vol. 7, pp. 478-94.
119. M. Hansen: Constitution of Binary Alloys, McGraw-Hill Book Co., New York, 1958, pp. 374-76.
120. K. E. Volk: Nickel und Nickellegierungen, Springer-Verlag, 1970, p. 9.
121. H. J. Goldschmidt: Interstitial Alloys, Plenum Press, New York, 1967, pp. 98, 116, 125, 132, 186.
122. R. E. Reed-Hill and A. S. Gülec: Met. Trans., 1975, vol. 6A, pp. 461-66.
123. P. Haasen and A. Kelly: Acta Met., 1957, vol. 5, pp. 192-99.
124. S. Siegel and S. L. Quimby: Phys. Rev., 1936, vol. 49, pp. 663-70.
125. W. Köster, Z. Metallkde., 1943, vol. 39, pp. 1-9.
126. Metals Handbook, vol. 1, ASM, Metals Park, Ohio, p. 1217.
127. A. M. Garde: Ph.D. Dissertation, University of Florida, 1974.
128. A. T. Santhanam and R. E. Reed-Hill: Scripta Met., 1970, vol. 4, pp. 529-32.

129. A. T. Santhanam: Ph.D. Dissertation, 1971, pp. 30-34.
130. R. E. Reed-Hill: Private communication.
131. A. M. Garde and R. E. Reed-Hill: "Zirconium in Nuclear Applications," ASTM STP 551, American Society for Testing and Materials, 1974, pp. 75-91.
132. J. R. Donoso: Unpublished research, University of Florida.
133. T. B. Gibbons and M. H. Brown: Scripta Met., 1975, vol. 9, pp. 15-16.
134. P. Ambrosi, E. Göttler, and C. Schwink: Scripta Met., 1974, vol. 8, pp. 1093-98.
135. D. Kuhlmann-Wilsdorf: Scripta Met., 1973, vol. 7, pp. 1059-64.
136. A. C. Damask and G. J. Dienes: Point Defects in Metals, Gordon and Breach, New York, 1963, pp. 292-94.
137. A. W. Cocharadt, G. Schoeck and H. Wiedersich: Acta Met., 1955, vol. 3, pp. 532-33.
138. F. R. N. Nabarro: Report on Strength of Solids, 1948, Physical Society of London, p. 38.
139. F. R. N. Nabarro: Theory of Crystal Dislocations, Oxford University Press, 1967, p. 431.
140. H. K. Birnbaum and F. R. Tuler: J. Appl. Phys., 1961, vol. 32, pp. 1403-04.
141. H. K. Birnbaum: J. Appl. Phys., 1962, vol. 33, pp. 750-51.
142. F. R. N. Nabarro: Theory of Crystal Dislocations, Oxford University Press, 1967, pp. 409-18.
143. R. W. Baluffi, J. S. Koehler and R. O. Simmons: Recovery and Recrystallization of Metals, Gordon and Breach, 1968, pp. 1-62.
144. K. V. Ravi and R. Gibala: Met. Trans., 1971, vol. 2, pp. 1219-25.
145. L. Katz, M. Guinan and R. J. Borg: Phys. Rev. B, 1971, vol. 4, p. 330.
146. C. S. Hartley: Private communication.
147. J. S. Blakemore: Met. Trans., 1970, vol. 1, pp. 1281-85.

148. J. S. Blakemore and E. O. Hall: Trans. Met. Soc. AIME, 1968, vol. 242, pp. 333-35.
149. D. J. Dingley and D. McLean: Acta Met., 1967, vol. 15, pp. 885-901.
150. J. D. Baird: The Inhomogeneity of Plastic Deformation, 1973, pp. 191-222.
151. A. Cottrell: Phil. Mag., 1953, vol. 44, pp. 829-32.
152. D. M. Barnett and W. D. Nix: Acta Met., 1973, vol. 21, pp. 1157-68.
153. J. P. Hirth and J. Lothe: Theory of Dislocations, McGraw-Hill, 1968, p. 398.
154. F. R. N. Nabarro: Theory of Crystal Dislocations, Oxford University Press, 1967, p. 403.
155. C. S. Barrett and T. B. Massalski: Structure of Metals, McGraw-Hill Book Co., New York, 1966, pp. 235-37.

BIOGRAPHICAL SKETCH

Walter Raymond Cribb was born on August 29, 1949, in Columbia, South Carolina. His father was a member of the U.S. Army and as a result, he travelled quite extensively with his family throughout his entire elementary and high school years to numerous places within the United States and also overseas to Panama and West Germany.

The author began his undergraduate work at the University of Florida in September, 1967. He entered the Department of Engineering Science and Mechanics and received the degree Bachelor of Science in Engineering Science (with honors) in December, 1972. January, 1973, the author began his work toward the Ph.D. degree in the Materials Science and Engineering department at the University of Florida. He received a Master of Engineering degree from this department in June, 1974. He is a member of the American Institute of Metallurgical Engineers as well as Tau Beta Pi, Sigma Tau and Alpha Sigma Mu honor societies.

He is a First Lieutenant in the United States Air Force Reserves. He is married to the former Katherine Ann Morlock who is presently expecting a child.

I certify that I have read this study and that in my opinion it conforms to acceptable standards of scholarly presentation and is fully adequate, in scope and quality, as a dissertation for the degree of Doctor of Philosophy.



R.E. Reed-Hill, Chairman
Professor of Materials Science
and Engineering

I certify that I have read this study and that in my opinion it conforms to acceptable standards of scholarly presentation and is fully adequate, in scope and quality, as a dissertation for the degree of Doctor of Philosophy.



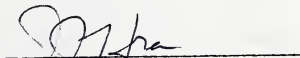
M.A. Eisenberg
Professor of Engineering Science
and Mechanics

I certify that I have read this study and that in my opinion it conforms to acceptable standards of scholarly presentation and is fully adequate, in scope and quality, as a dissertation for the degree of Doctor of Philosophy.



C.S. Hartley
Professor of Materials Science
and Engineering

I certify that I have read this study and that in my opinion it conforms to acceptable standards of scholarly presentation and is fully adequate, in scope and quality, as a dissertation for the degree of Doctor of Philosophy.



J.J. Hren
Professor of Materials Science
and Engineering

This dissertation was submitted to the Graduate Faculty of the College of Engineering and to the Graduate Council, and was accepted as partial fulfillment of the requirements for the degree of Doctor of Philosophy.

August, 1975

Wayne H. Chen

Dean, College of Engineering

Dean, Graduate School

#599 See man 38 (208)

204 75 300.5